UNIVERSITY OF OKLAHOMA

GRADUATE COLLEGE

Opposite Side Jet Charge Tagging and Measurement of CP Asymmetry Parameter $\sin(2\beta)$ at DØ

A Dissertation

SUBMITTED TO THE GRADUATE FACULTY

In partial fulfillment of the requirements

for the degree of

Doctor of Philosophy

by

Xiaojian Zhang

Norman, Oklahoma

2004

Opposite Side Jet Charge Tagging and Measurement of CP Asymmetry Parameter $\sin(2\beta)$ at DØ

A Dissertation APPROVED for THE

DEPARTMENT OF PHYSICS AND ASTRONOMY

BY

Phillip Gutierrez, CHAIR

Ron Kantowski

Mike Strauss

Bruce Mason

James Hawthorne

To my wife Yudong and our children

Rachael and Erica

and

To my parents, Mingchun and Hailiang

Acknowledgments.

My experience in the OU high energy physics group has been extremely fulfilling and fruitful. I greatly appreciate the support of the many people who have made this dissertation possible.

First, I would like to give thanks to my wife, Yudong. After graduating from OU biochemistry department with her M.S. degree, she moved with me to Chicago. While working in the Genetic Department at the University of Chicago, she has supported my efforts to complete a difficult thesis; work which often left little time for her and our two little daughters. The completion of 7 years of hard work would not be possible without her support.

I would also like to thank my adviser, Prof. Phillip Gutierrez, whose guidance, support, and friendship has make this experience a pleasure. He has shown consistent interest in my work, both thesis and service. His input and criticism have many times steered me back onto a productive course. I love the dictum by an ancient Chinese poet: "better slow and steady, not flighty and tricky; better plain and honest, not flowery and showy". Prof. Phillip Gutierrez has shown me the merits. The final quality of my dissertation is the result of his work.

I have enjoyed working with the members of the B-physics group at DØ , and thank the many individuals who have provided insight in reviewing my analysis, especially, Rick Van Kooten, Vivek Jain and Brendan Casey. I should also give my thanks to Prof. Mike Strauss and Prof. Brad Abbott, I have had many good discussions with them on the high energy physics topics and data analysis. Their input and criticism have kept me working hard and being fruitful. I also thank those who have worked on the DØ detector and the Fermilab Tevatron collider; without the hard work of these people this analysis would not be possible.

I owe special thanks to my host family, Michael and Jounee Mckee family. They have shared their love and friendship with me and my family since we came into the Unite States for the education endeavor. I feel lucky that my family has met with such a good host family. I would also like to take this opportunity to give thanks to my many friends in Norman, especially Jim and Jerry White. Finally, I wish to thank my parents and parents in law for their consistent interest and support in my work. I consider myself very fortunate to have such wonderful parents.

Contents

List of Figures

List of Tables

Chapter 1

Introduction

This dissertation describes the first CP asymmetry parameter $\sin(2\beta)$ measurement by the DØ collaboration running at the Fermilab proton-antiproton collider (Tevatron). The analysis uses the opposite side jet charge tagging algorithm (JETQ), which was developed for this study, to determine the production flavor of the reconstructed neutral B-mesons. The tagging algorithm is tested using Monte Carlo samples that include all three major $b\bar{b}$ production mechanisms (Flavor Creation, Flavor Excitation, and Gluon Splitting).

It is shown that the JETQ tagging result is a function of $\Delta\phi$, the azimuthal cone about the reconstructed B-meson, and p_T, the transverse momentum of the B-meson. We have compared the JETQ tagging results using a data sample of fully reconstructed $B^{\pm} \to J/\psi K^{\pm}$ with our MC results. Good agreement has been found.

The JETQ tagging algorithm is then used to measure the CP asymmetry

parameter $\sin(2\beta)$ from $B_d \rightarrow J/\psi K_s$ using both the time dependent and time integrated asymmetry. The time integrated measurement yields $\sin(2\beta) = 0.82 \pm 1.80$, and the time dependent asymmetry gives $\sin(2\beta) = 1.80 \pm 1.15$. Both results are consistent with the world average value for $\sin(2\beta)$. The integrated luminosity of the data sample used in this analysis is 225 pb^{-1}.

Chapter 2

Theoretical Survey

High energy physics studies the fundamental properties of elementary particles. Any theory of elementary particles must be consistent with both *the special theory of relativity* and *quantum mechanics*. Dirac's equation successfully united the two theories and laid the foundation for *Quantum Field Theory* (QFT), which is used to describe high energy physics.

2.1 The Standard Model

All known particle physics phenomena are well described within the Standard Model (SM) of elementary particles and their fundamental interactions. In this section, we give a brief overview of the Standard Model [1] [2]. We discuss in section 2.1.1 the fundamental particles and in section 2.1.2 the fundamental interactions. In section 2.1.3, some important elements of the Standard Model

are discussed, such as Quantum Electrodynamics, Quantum Chromodynamics, etc.

2.1.1 Fundamental particles

The Standard Model asserts that the material in the universe is made up of elementary fermions, which are the sources of the fields through which they interact. The particles associated with the interaction fields are gauge bosons.

The elementary fermions are subdivided into two types of elementary particles: leptons and quarks. These particles are grouped into three generations, with each generation consisting of two leptons and two quarks. Therefore there are altogether six leptons and six quarks. The leptons are the electron, tau, muon, and their associated neutrinos. The quarks are down, up, strange, charm, bottom and top. The name of a quark is also known as its flavor. There is a very important difference between quarks and leptons: each quark carries one of the three colors (Red, Green, Blue) - the charge of the strong interaction, leptons don't. Table 2.1 and 2.2 (from PDG group, 2002) summarize the basic properties of leptons and quarks.

The gauge bosons are composed of eight gluons and the photon γ, $W^{\pm}$ and Z. As for the theoretical aspects, the SM is a quantum field theory that is based on the gauge symmetry $SU(3)_c \times SU(2)_L \times U(1)_Y$. This gauge group includes the

Lepton	Charge	Mass(MeV/c^2)
Electron(e)	-1	0.511
Electron Neutrino(ν_e)	0	$\leq\ 3 \times 10^{-6}$
Muon(μ)	-1	105.7
Muon Neutrino(ν_μ)	0	$\leq$0.19
Tau(τ)	-1	1777
Tau Neutrino(ν_τ)	0	$\leq$18.2

Table 2.1: Properties of fundamental leptons

Quark	Charge	Mass(MeV/c^2)
Up(u)	2/3	$1.5 \sim 4.5$
Down (d)	-1/3	$3.0 \sim 9$
Charm(c)	2/3	$1000. \sim 1400$
Strange (s)	-1/3	$60 \sim 170$
Top (t)	2/3	$174.3 \pm 5.1\,\mathrm{GeV}$
Bottom (b)	-1/3	$4000 \sim 4500$

Table 2.2: Properties of fundamental quarks

symmetry group of the strong interactions ($SU(3)_c$) and the symmetry group of the electroweak interactions ($SU(2)_L \times U(1)_Y$). The gluons are the gauge bosons of $SU(3)_c$. the γ, $W^\pm$ and Z are the gauge bosons of $SU(2)_L \times U(1)_Y$. Table 2.3 (from PDG group, 2002) summarizes the basic properties of the gauge bosons.

Boson	Charge	Mass(GeV/c^2)
gluon	0	massless
γ	0	massless
$W^{\pm}$	± 1	80.419
Z	0	91.19

Table 2.3: Properties of the gauge bosons

2.1.2 Fundamental interactions

There are four types of interactions in the SM: gravitational, electromagnetic, weak and strong.

The gravitational interaction describes the force between particles that results from their mass. Isaac Newton was one of the pioneers studying the interaction and proposed the Law of Universal Gravitation over 300 years ago. In the SM, the gravitational interaction is assumed to be mediated by gravitons, although they have not been found in any experiment. The most promising approach to developing a quantum theory of gravity may be *String Theory*, which asserts that elementary particles are not point like but rather are small lines or loops of energy, "strings".

The electromagnetic interaction describes the force between charged particles through the exchange of one or more photons. Quantum Electrodynamics (QED) has been very successful at explaining the electromagnetic interaction. This theory not only includes classical electrodynamics in the limit of large distances,

but also explains purely quantum phenomena such as the structure of atoms and molecules, pair production ($\gamma \rightarrow e^+e^-$), etc. The prediction of the anomalous magnetic moment of the electron is probably the most accurate prediction. It has been experimentally confirmed to 11 decimal digits!

The weak interaction describes the force between elementary particles mediated by $W^{\pm}$ or Z bosons. There are a number of conservation laws that are broken by weak processes, e.g. parity violation. The weak interactions have been united with the electromagnetic interactions in the Weinberg-Salam Model.

The strong interaction describes the force between quarks mediated by gluons. The strong interaction binds protons and neutrons together in the nuclei of atoms. Leptons don't involve the strong interaction. Quarks are described as having "red," "green," or "blue" color and anti-color for anti-quarks. Because of the color property of quarks, the theory which describes the strong interaction is named *Quantum Chromodynamics* (QCD). No free quarks have ever been observed due to its strong interaction field. Quarks are bound together in hadrons. There two types of hadrons: mesons (quark and anti-quark pairs) and baryons (triplets of quarks). Consequently, it is hypothesized that only colorless particle can be observed in nature, for example, a meson may consist of red and anti-red quarks, and a baryon may consist of a red, a green, and a blue quark (the result is a colorless baryon). Glueball is a fascinating prediction of this hypothesis. It consists of bound gluons, forming a lump of pure energy.

2.1.3 Some Important Elements of the Standard Model

The Standard Model is a Quantum Field Theory with the requirement of local gauge invariance. There is a symmetry S when the physical system under study has an invariance under the transformation given by S or, equivalently, when the Hamiltonian of this system H is invariant, i.e.,

$$SHS^{+} = H \tag{2.1}$$

2.1.3.1 **Symmetries**

Symmetries can be classified differently based on different ways. Classified by the kind of parameters, symmetries can be divided. There are two basic types of symmetries:

1. Discrete symmetries: The parameters for this symmetry take discrete values only. For examples, Parity P: flip the coordinate in a physical system; Charge Conjugation C: flip the charge of all particles in a physical system; Time Reversal T: flip the time. The CPT Theorem asserts that all interactions must be invariant under the total transformation given by the combination of C, P, T, irrespectively of their order. The electromagnetic and strong interactions are invariant in P, C, T separately as well as any of their combinations. The weak interaction can violate C, P and CP.

2. Continuous symmetries: The parameters take continuous values. An example of this type are the rotations ($R(\theta)$), where the rotation angle θ can take any values.

The following two asymmetries play very important roles in the Standard Model. They are both continuous symmetries:

1. Global symmetries: the continuous parameters of the transformation **do not depend** on the space-time coordinates. For example, a global rotation by a given phase $\Psi \rightarrow e^{i\alpha}\Psi$

2. Local (Gauge) symmetries: the continuous parameters of the transformation **do depend** on the space-time coordinates, e.g. when the global phase changes to a local one, giving $\Psi \rightarrow e^{i\alpha(x)}\Psi$

There are two theorems/principles that apply to the two symmetries and give important physical implications. Noether's Theorem asserts that for a physical system having a global symmetry, there must be a current and the associated charge that are conserved. The Gauge Principle requires new vector boson fields (interaction fields) to be introduced to keep the local gauge invariance. This will discussed more in the following sections.

2.1.3.2 **The Gauge Theory of Electromagnetic Interactions: QED**

Quantum Electrodynamics is the most successful Gauge Theory and has been tested up to an extremely high level of precision. To construct the QED

Lagrangian, one starts with a free Dirac field Ψ with spin $\frac{1}{2}$, mass m and electric charge Qe. The field is described by the Dirac equation

$$(i\gamma^{\mu}\partial_{\mu} - m)\Psi(x) = 0 \tag{2.2}$$

The Dirac Lagrangian density is thus given as follows

$$L = i\bar{\Psi}(x)\gamma^{\mu}\partial_{\mu}\Psi(x) - m\bar{\Psi}(x)\Psi(x) \tag{2.3}$$

The Lagrangian in Eq. 2.3 is invariant under a global gauge transformation which act on the field as follows

$$\Psi \rightarrow e^{iQ\theta}\Psi;\ \bar{\Psi} \rightarrow \bar{\Psi}e^{-iQ\theta} \tag{2.4}$$

By Noether's Theorem, this global $U(1)$ invariance of L implies the conservation of the electromagnetic current, J_{μ}, and the electromagnetic charge, eQ. However, the Lagrangian L is not invariant under a local gauge transformation, but yielding an additional term from the derivative term as follows

$$L \rightarrow L - Q(\partial_{\mu}\theta)\bar{\Psi}\gamma^{\mu}\Psi \tag{2.5}$$

To insist on local gauge invariance, we can introduce a gauge field A_{μ}, which transforms under a local gauge transformation according to the rule (It is inferred by the Maxwell Equations, since under this gauge transformation, the Maxwell equations are invariant)

$$A_{\mu} \rightarrow A_{\mu} - \frac{1}{e}\partial_{\mu}\theta(x) \tag{2.6}$$

The introduction of the new boson field (photon field) A_μ leads to the complete QED Lagrangian, invariant under a local gauge transformation

$$L = i\bar{\Psi}\gamma^\mu\partial_\mu\Psi - m\bar{\Psi}\Psi - (eQ\bar{\Psi}\gamma^\mu\partial_\mu\Psi)A_\mu - \frac{1}{16\pi}F^{\mu\nu}F_{\mu\nu} \tag{2.7}$$

where $-\frac{1}{16\pi}F^{\mu\nu}F_{\mu\nu}$ corresponds the kinetic energy term of the introduced gauge field. The mass of the gauge field has to be zero, because the mass term will spoil the local gauge symmetry under the transformation in Eq. 2.6. The interaction term $(eQ\bar{\Psi}\gamma^\mu\partial_\mu\Psi)A_\mu$ describes the electromagnetic current interacting with the photon fields.

After introducing a covariant derivative

$$D_\mu \equiv \partial_\mu + ieQA_\mu \tag{2.8}$$

the Lagrangian can be written in a more concise form

$$L = i\bar{\Psi}\gamma^\mu D_\mu\Psi - m\bar{\Psi}\Psi - \frac{1}{16\pi}F^{\mu\nu}F_{\mu\nu} \tag{2.9}$$

Finally, the gauge group for electromagnetic interactions is $U(1)_{em}$ with one generator, Q and one parameter θ.

2.1.3.3 **The Gauge Theory of Strong Interactions: QCD**

Quantum Chromodynamics describes the strong interactions. It is based on the local gauge symmetry of the color state transformations which leave the Hamiltonian of the strong interaction invariant. The free Lagrangian of QCD is

$$L = i\bar{q}\gamma^\mu\partial_\mu q - m\bar{q}q \tag{2.10}$$

where

$$q = \begin{pmatrix} q_r \\ q_b \\ q_g \end{pmatrix} \tag{2.11}$$

$$\bar{q} = (\bar{q}_r, \bar{q}_b, \bar{q}_g) \tag{2.12}$$

The q_r, q_b, q_g correspond the three color states of quarks. For the same reason as mentioned in the QED case, this free Lagrangian is not invariant under the local gauge transformation as follows

$$q(x) \rightarrow Uq(x) \equiv e^{i_\alpha(x)T_a} q(x) \tag{2.13}$$

where U is an arbitrary 3×3 unitary matrix. T_a are a set of linearly independent traceless matrices with a = 1, ..., 8, and α_a are the group parameters. A summation over the repeated suffix a is imposed.

To keep it invariant under the local gauge transformation, new boson fields must be introduced. Actually, eight gauge fields (G^a_μ are introduced, each transforming as

$$G^a_\mu \rightarrow G^a_\mu - \frac{1}{g}\partial_\mu \alpha_a - f_{abc}\alpha_b G^c_\mu \tag{2.14}$$

f_{abc} are real constants, called the structure constants of the group. The Lagrangian density of QCD finally becomes

$$L = i\bar{q}\gamma^\mu \partial_\mu q - m\bar{q}q - g(\bar{q}\gamma^\mu T_a q)G^a_\mu - \frac{1}{4}G^a_{\mu\nu}G^{\mu\nu}{}_a \tag{2.15}$$

$G^{\mu\nu}$ is the gluon field strength defined as

$$G^a_\mu = \partial_\mu G^a_\nu - \partial_\nu G^a_\mu - g f_{abc} G^b_\mu G^c_\nu \tag{2.16}$$

$\frac{1}{4} G^a_{\mu\nu} G^{\mu\nu}{}_a$ is the kinematic energy of the gluon field. The interaction term $g(\bar{q}\gamma^\mu T_a q) G^a_\mu$ describes the quark flux current interacting with the gluon fields. Again, one can define the covariant derivative as follows

$$D_\mu = \partial_\mu + igT_a G^a_\mu \tag{2.17}$$

to write the Lagrangian in a more concise form

$$L = i\bar{q}\gamma^\mu D_\mu q - m\bar{q}q - \frac{1}{4} G^a_{\mu\nu} G^{\mu\nu}{}_a \tag{2.18}$$

2.1.3.4 **The unification of the electromagnetic and weak interactions: The Electroweak Theory**

To combine the weak and electromagnetic interactions, we must replace the interaction term in QED Lagrangian with the following two basic interactions

$$-ig\mathbf{J}_\mu \cdot \mathbf{W}_\mu + -i\frac{g'}{2} j^Y_\mu B^\mu \tag{2.19}$$

$\mathbf{W}^\mu$ and B^μ are the fields in the electroweak interactions. The observed fields are the mixed of $\mathbf{W}^\mu$ and B^μ through

$$W^\pm_\mu = \frac{1}{2}(W^1_\mu \pm W^2_\mu) \quad (massive) \tag{2.20}$$

$$Z_\mu = -B_\mu \cos\theta_w + W^3_\mu \sin\theta_w \quad (massive) \tag{2.21}$$

$$A_\mu = B_\mu \cos\theta_w + W_\mu^3 \sin\theta_w \quad (massless) \tag{2.22}$$

where θ_w is the Weinberg angle. The $W^\pm$ and Z gauge bosons were discovered at CERN in 1983. Their massive properties cause the weak interaction to be short ranged. Massive bosons will spoil local gauge invariance. To describe the short ranged weak interactions by a gauge theory without spoiling gauge invariance, the Higgs Mechanism was proposed. The Higgs Mechanism applies spontaneous symmetry breaking (SSB) to a gauge theory. Finally, the Lagrangian density of the Electroweak Model can be written in symbolic form as

$$L = L(f,G) + L(f,H) + L(G,H) + L(G) - V(H) \tag{2.23}$$

where f stands for fermions, G for gauge bosons, and H for the Higgs doublet (Discussed in the next section).

The CabibboKobayashiMaskawa (CKM) Matrix

In the Standard Model, the quark mass eigenstates are not equal to the weak eigenstate. The CKM matrix rotates the quark mass eigenstates into the weak eigenstates as follows

$$\begin{pmatrix} d' \\ s' \\ b' \end{pmatrix} = \begin{pmatrix} V_{ud} & V_{us} & V_{ub} \\ V_{cd} & V_{cs} & V_{cb} \\ V_{td} & V_{ts} & V_{tb} \end{pmatrix} \begin{pmatrix} d \\ s \\ b \end{pmatrix} \tag{2.24}$$

The CKM matrix is a 3×3 unitary matrix. Its individual elements are the probabilities that a quark will turn into a different kind of quark in a weak interaction.

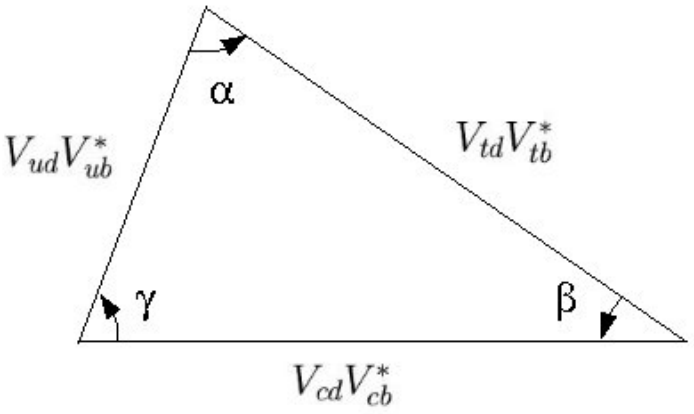

Figure 2.1: The unitary triangle.

The elements are not predicted by theory, but measured in experiments. The unitarity property gives a number of constraint equations such as

$$|V_{ud}|^2 + |V_{us}|^2 + |V_{ub}|^2 = 1 \tag{2.25}$$

$$V_{ud}V_{ub}^* + V_{cd}V_{cb}^* + V_{td}V_{tb}^* = 0 \tag{2.26}$$

Equation 2.26 describes a triangle in the complex plane, called the unitary triangle shown in Fig. 2.1. The lengths of the sides are $|V_{ud}V_{ub}^*|$, etc. The angles are given by

$$\alpha = arg[-\frac{V_{td}V_{tb}^*}{V_{ud}V_{ub}^*}] \quad \beta = arg[-\frac{V_{cd}V_{cb}^*}{V_{td}V_{tb}^*}] \quad \gamma = arg[-\frac{V_{ud}V_{ub}^*}{V_{cd}V_{cb}^*}] \tag{2.27}$$

where $\alpha + \beta + \gamma = \pi$.

For a real 3×3 unitary matrix, there are nine parameters with six constraint equations from $UU^\dagger = \mathbf{1}$. Therefore, there are only three independent parameters to be determined, corresponding to the three Euler angles of the rotation matrix.

For a complex 3×3 unitary matrix, there are eighteen parameters and nine constraint equations. It is much easier to see this by writing the matrix elements in form of $e^{i\theta_{kl}} A_{kl}$. Using this form, one can immediately see that the diagonal elements in the expansions of equation $UU^\dagger = \mathbf{1}$ only constrain the real part, therefore giving three constraints. The off-diagonal elements are symmetric, except a flipped sign in each imaginary part, giving three constraints in the real part and three constraints in the imaginary part. Therefore the number of the total constraints is nine, and the number of the independent parameters is nine.

Again, three of the nine parameters are the Euler angles of rotation. There are five unobservable parameters, since the phase of each quark can be changed freely (as long as the difference between phases remains constant) without causing any observable effect. The last independent parameter is the measurable phase parameter. With the four measurable parameters, the CKM matrix can be written in the following form

$$V = \begin{pmatrix} c_{12}c_{13} & s_{12}c_{13} & s_{13}e^{-i\delta_{13}} \\ -s_{12}c_{23} - c_{12}s_{23}s_{13}e^{i\delta_{13}} & c_{12}c_{23} - s_{12}s_{23}s_{13}e^{i\delta_{13}} & s_{23}c_{13} \\ s_{12}s_{23} - c_{12}c_{23}s_{13}e^{i\delta_{13}} & -c_{12}s_{23} - s_{12}s_{23}s_{13}e^{i\delta_{13}} & c_{23}c_{13} \end{pmatrix} \tag{2.28}$$

with $c_{ij} = \cos\theta_{ij}$ and $s_{ij} = \sin\theta_{ij}$ for the "generation" labels i,j = 1, 2, 3. The area of the unitary triangle is $|J|/2$, where J is given by

$$J = c_{12}c_{23}c_{13}^2 s_{12}s_{23}s_{13}\sin\delta_{13} \tag{2.29}$$

2.2 Heavy Quark Production

The term "heavy quark" refers to a parton with mass large compared to the QCD scale Λ. Hadron colliders are by far the largest source of heavy quarks available today. Heavy quark production at hadron colliders provide a quantitative means of testing perturbative QCD at the next-to-leading order (NLO) in the limit of large masses relative to Λ_{QCD}.

At hadron colliders the production of heavy quarks is described by QCD. The creation of heavy quarks at $p\bar{p}$ collider is hypothesized to occur via the interaction of the partons in the beam particles. These partons are the valence quarks of the hadron and the gluons and sea quarks. Sea quarks exist in a proton due to the frequent gluon splitting process. Compared with the valence quark, they carry much smaller fraction of the total momentum of the proton. For the b-quark productions, the distribution most commonly studied in the hadron collider experiments is the b-quark transverse momentum distribution in a fixed pseudorapidity region:

$$\sigma(p_T > p_T^{min}) = \int_{|\eta|<|\eta_{max}|} d\eta \int_{p_T>p_T^{min}} dp_T \frac{d\sigma^2}{d\eta dp_T} \tag{2.30}$$

In hadron collisions, heavy quark production at leading order (LO) occurs through both $q\bar{q}$ annihilation ($q\bar{q} \to Q\bar{Q}$), and $\hat{s}$ and $\hat{t}$-channel gluon-gluon fusion ($g\bar{g} \to Q\bar{Q}$). The two processes dominate in different regions of phase space, with $q\bar{q}$ annihilation being the major process near the $Q\bar{Q}$ threshold and large p_T, and

gluon processes dominate at low p_T. At the Tevatron, $b\bar{b}$ production is dominated by gluon processes, while 90% of the $t\bar{t}$ production is due to $q\bar{q}$ annihilation.

NLO calculations of heavy quark production have been available for a long time [6] [7]. These processes include $q\bar{q} \to Q\bar{Q}g$, $gq \to Q\bar{Q}q$, $g\bar{q} \to Q\bar{Q}\bar{q}$, $gg \to Q\bar{Q}g$. In addition to the NLO processes of $q\bar{q}$ annihilation and gluon-gluon fusion, two other subprocesses come into the total b production, namely, flavor excitation and gluon splitting. The detail of the subprocesses will be discussed in chapter 6.

The comparisons of NLO QCD with the Tevatron data have been made by both the DØ and CDF experiments. Figure 2.2 shows results from the DØ experiment compared to theory. Figure 2.3 shows results from the CDF experiment compared to theory. There is good agreement between the shape of the distribution observed in data and that predicted by theory. However, the data are higher by a factor of approximately 2 with respect to the NLO QCD prediction when the default parameters ($\mu = \mu_0$) are used.

The contributions to the total heavy quark production from the higher orders were found to be important mainly in two regions: near threshold, corresponding to the low p_T domain, and very large p_T. It has been shown in [8] that the total b-quark cross section at the Tevatron is increased no more than 30% by the threshold effects. The effects are explained by initial state gluon radiation and Coulomb enhancement from the virtual gluon exchange between the heavy

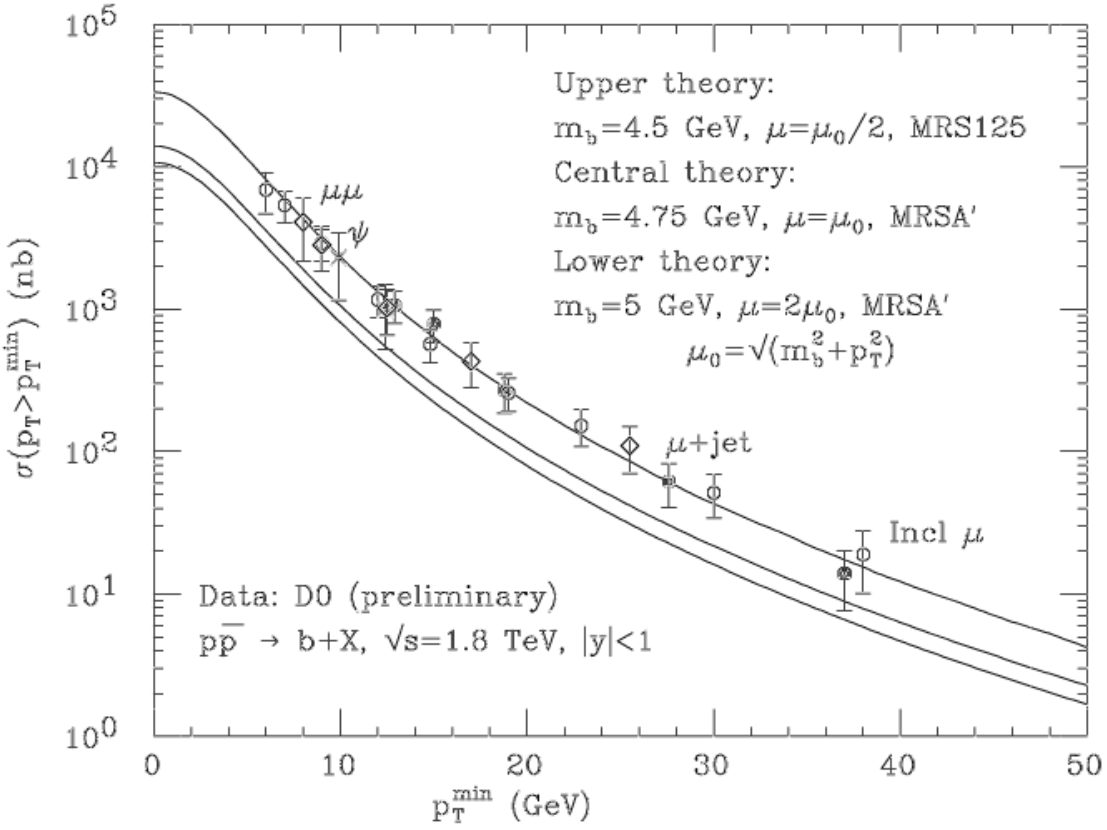

Figure 2.2: Compare CDF data on the integrated b-quark p_T distribution with the results of NLO QCD.

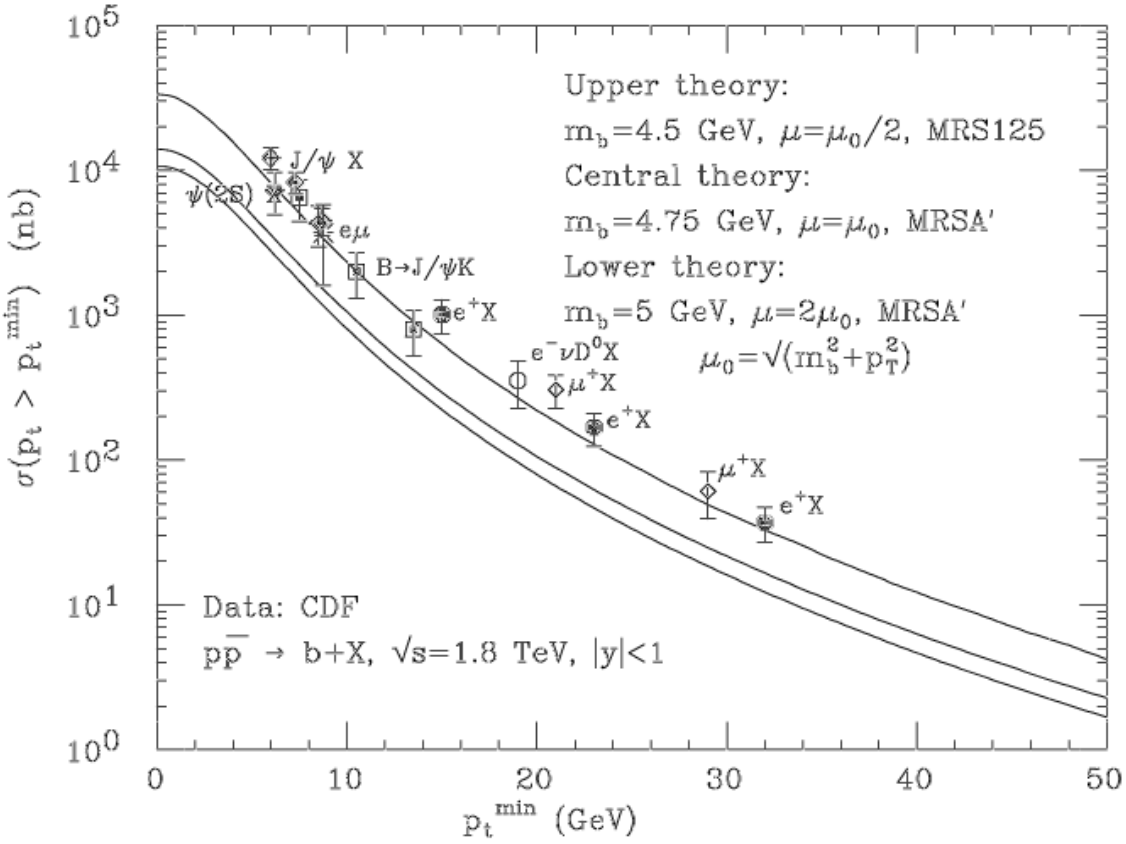

Figure 2.3: Compare DØ data on the integrated b-quark p_T distribution with the results of NLO QCD.

quarks. The enhancement is due to the exchange of a spin 1 gluon in the $\hat{t}$ channel. At large momentum, the b-quark behaves more and more like a massless particle, radiating an increasingly large amount of its energy in the form of hard, collinear gluons. This physical phenomenon is associated with the presence of logrithms of the form $\log(p_T/m)$, which appears at all orders in perturbation thery. It has been shown in [9] that some logarithmically enhanced higher-order terms are negative and small up to transverse momenta of order of $20\,\mathrm{GeV}/C$.

2.3 B mixing and CP violation

$B^0 - \bar{B}^0$ mixing refers to transitions between the two flavor eigenstates $|B^0\rangle$ and $|\bar{B}^0\rangle$. CP violation in B mesons is caused by the non-vanishing phase in the CKM matrix. CP violation in the B-system has a close relation to B mixing. In section 2.3, we discuss B mixing. B CP violation and its relation to B mixing is discussed in section 2.3. For more information, refer to Ref. [12] and [13].

2.3.1 B mixing

In strong interactions, the neutral B mesons are produced in two well defined flavor eigenstates: $|B^0\rangle$ (containing a $\bar{b}$) or $|\bar{B}^0\rangle$ (containing a b). Their evolution in time is ruled by the Hamiltonian equation

$$ih\frac{\partial}{\partial t}\begin{pmatrix}|B^0\rangle\\|\bar{B}^0\rangle\end{pmatrix} = (\mathbf{M} - \frac{i}{2}\mathbf{\Gamma})\begin{pmatrix}|B^0\rangle\\|\bar{B}^0\rangle\end{pmatrix} \tag{2.31}$$

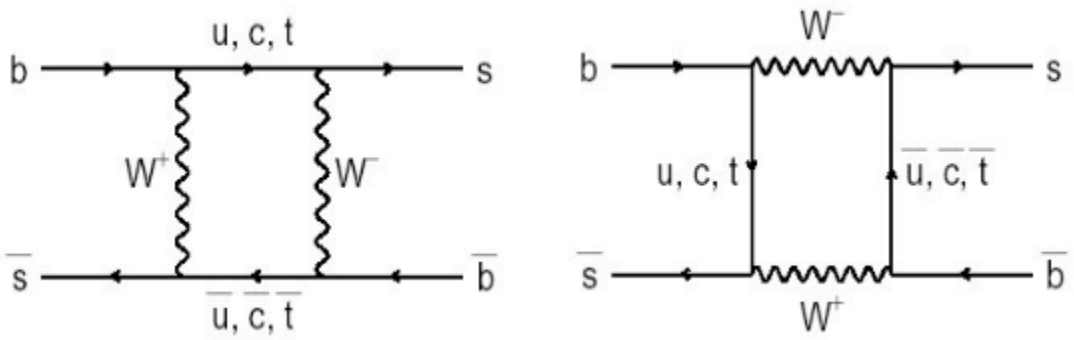

Figure 2.4: Standard Model box diagrams including $B^0 - \bar{B}^0$ mixing.

where $\mathbf{M}$ and $\mathbf{\Gamma}$ are the mass and decay matrices respectively. These matrices are Hermitian, and CPT invariance requires $M_{11} = M_{22} \equiv M$ and $\Gamma_{11} = \Gamma_{22} \equiv \Gamma$.

In the Standard Model $B^0 - \bar{B}^0$ mixing is caused by the fourth order flavor changing weak interaction described by the box diagrams in Fig. 2.4. In such transitions, the bottom quantum number is changed by 2 ($|\Delta B| = 2$). $|\Delta B| = 2$ transitions induce non-zero off-diagonal elements in 2.31. The two mass eigenstates are labeled as $|B_\pm\rangle$ (Not B^+ and B^- meson!) which can be expressed in the basis of the flavor eigenstates

$$|B_\pm\rangle = p|B^0\rangle \pm q|\bar{B}^0\rangle \tag{2.32}$$

with corresponding eigenvalues

$$\lambda_\pm = (M - \frac{i}{2}\Gamma) \pm \frac{q}{p}(M_{12} - \frac{i}{2}\Gamma_{12}) \tag{2.33}$$

where

$$\frac{q}{p} = \sqrt{\frac{M_{12}^* - \frac{i}{2}\Gamma_{12}^*}{M_{12} - \frac{i}{2}\Gamma_{12}}} \tag{2.34}$$

The convention where $Re(q/p) > 0$ and $CP|B^0\rangle = |\bar{B}^0\rangle$ has been used. From Eq. 2.32, it is easy to obtain the evolution of a pure $|B^0\rangle$ or $|\bar{B}^0\rangle$ state at $t = 0$

$$|B^0(t)\rangle = g_+(t)|B^0\rangle + \frac{q}{p}g_-(t)|\bar{B}^0\rangle \tag{2.35}$$

$$|\bar{B}^0(t)\rangle = g_+(t)|\bar{B}^0\rangle + \frac{p}{q}g_-(t)|B^0\rangle \tag{2.36}$$

where $g_\pm(t) = \frac{1}{2}(e^{-i\lambda_+ t} \pm e^{-i\lambda_- t})$. Equations 2.35 and 2.36 says that, for a $|B^0\rangle$ state produced at $t = 0$, there is a finite probability of finding it in a $|\bar{B}^0\rangle$ state at time t, and vice versa. This phenomenon is known as the *mixing* of B meson. The time-dependent probabilities of unmixed and mixed are proportional to the squared amplitude of the corresponding coefficients

$$|g_\pm(t)|^2 = \frac{e^{-\Gamma t}}{2}[\cosh(\frac{\Delta\Gamma t}{2}) \pm \cos(\Delta m t)] \tag{2.37}$$

where

$$\Delta m = |M_+ - M_-|, \quad \Delta\Gamma = |\Gamma_+ - \Gamma_-|, \tag{2.38}$$

For the B_d^0 mesons, $|M_{12}/\Gamma_{12}|$ is about 1000. Therefore, in the time period of observing the mixing of B_d^0, it is safe to assume $\Delta\Gamma \approx 0$, making $g_\pm(t)$ take on the simple form

$$|g_\pm(t)|^2 = \frac{e^{-\Gamma t}}{2}[1 \pm \cos(\Delta m t)] \tag{2.39}$$

2.3.2 **CP violation in B mesons**

CP violation was first observed in the neutral kaon system [14]. The neutral kaon system has a short lived particle called K_s and a long lived particle called

K_L. K_s has CP eigenvalue of 1, thus decaying to 2 pions. K_L has CP eigenvalue of -1, decaying to 3 pions. In 1964 the experiment of Jim Cronin and Val Fitch showed that a small fraction of the time (about one case in every 500, a fraction called epsilon) the K_L decays to 2 pions, a clear signature of CP violation.

CP-violating effects in decays of B mesons were predicted later in [15]. According to the Standard Model, CP violation occurs in the weak interaction, more specifically it is in the quark flavor-changing process due to the weak interaction. The Standard Model predicts that CP violation is caused by a non-vanishing phase in the quark mixing matrix, i.e. CKM matrix. It was found that all CP violating quantities are proportional to J.

There are three different types of CP violations: *indirect CP violation, direct CP violation, CP violation of interference*. To study them, we define the transition amplitude for $|B^0\rangle \to f$ and $|\bar{B}^0\rangle \to f$ and their ratio below

$$\begin{aligned} A(f) &= \langle f|H|B^0\rangle \\ \bar{A}(f) &= \langle f|H|\bar{B}^0\rangle \\ \rho(\bar{f}) &= \frac{\bar{A}(f)}{A(f)} \end{aligned} \tag{2.40}$$

where f is a final state that is possible for both $|B^0\rangle$ and $|\bar{B}^0\rangle$. Using Eq. 2.35

and 2.36, the time dependent transition rates are calculated to be

$$\Gamma(|B^0(t)\rangle \to f) \propto$$
$$e^{-\Gamma t}|A(f)|^2[(1+\cos(\Delta mt)) + \ (1-\cos(\Delta mt))|\frac{q}{p}|^2|\bar{\rho}(f)|^2$$
$$+ \ Re[4e^{\Gamma t}g_-(t)g_+^*(t)(\frac{q}{p})\bar{\rho}(f)]] \tag{2.41}$$

$$\Gamma(|\bar{B}^0(t)\rangle \to f) \propto$$
$$e^{-\Gamma t}|\bar{A}(f)|^2[(1+\cos(\Delta mt)) + (1-\cos(\Delta mt))|\frac{p}{q}|^2|\rho(f)|^2$$
$$+ \ Re[4e^{\Gamma t}g_-(t)g_+^*(t)(\frac{p}{q})\rho(f)]] \tag{2.42}$$

The indirect CP violation is caused by the apparently different mixing rates between $|B^0\rangle$ and $|\bar{B}^0\rangle$ when $|q/p| \neq 1$(see Eq. 2.35 and 2.36). It is related to a non-vanishing relative phase between the mass and the width parts of the mixing matrix that causes $|q/p| \neq 1$. If the relative phase is 0, there will be no B^0 mixing, and no indirect CP violation.

The direct CP violation is caused by a difference in phase between the two decay amplitudes in equation 2.40. This phase difference leads to $|\rho(f)| \neq 1$.

For the transitions of $B^0 \to f$ and $\bar{B}^0 \to f$, there is interference between decays with and without mixing whenever $Arg((q/p)\bar{\rho}(f)) \neq 0$, causing the CP violation of interferences. We can understand how this interference cause differences between the interference terms in Eq. 2.41 and 2.42 by noting that

$Arg((q/p)\bar{\rho}(f)) \neq 0$ means $((q/p)\bar{\rho}(f))$ is a real number. Therefore the interference term is identical if $|\rho(f)| = 1$ and $|q/p| = 1$.

Chapter 3

The DØ Detector

This chapter contains a brief description of the DØ detector. The details of the detector can be found in Ref. [17] [18].

3.1 Introduction

3.1.1 The Fermilab Tevatron

The DØ detector is located at the Fermilab $p\bar{p}$ Tevatron collider. The Tevatron is presently the world's highest-energy hadron collider, with a center-of-mass energy of 1960 GeV. Figure 3.1 shows the schematic of the accelerator complex.

A brief description is provided in Fig. 3.2 for the generation of 1960 GeV proton and antiproton colliding beams at the Tevatron collider. The beams originate in the preaccelerator (Preacc). There, H^- ions are formed and accelerated to 750 KeV by an electrostatic Cockroft-Walton accelerator. The ions are bunched

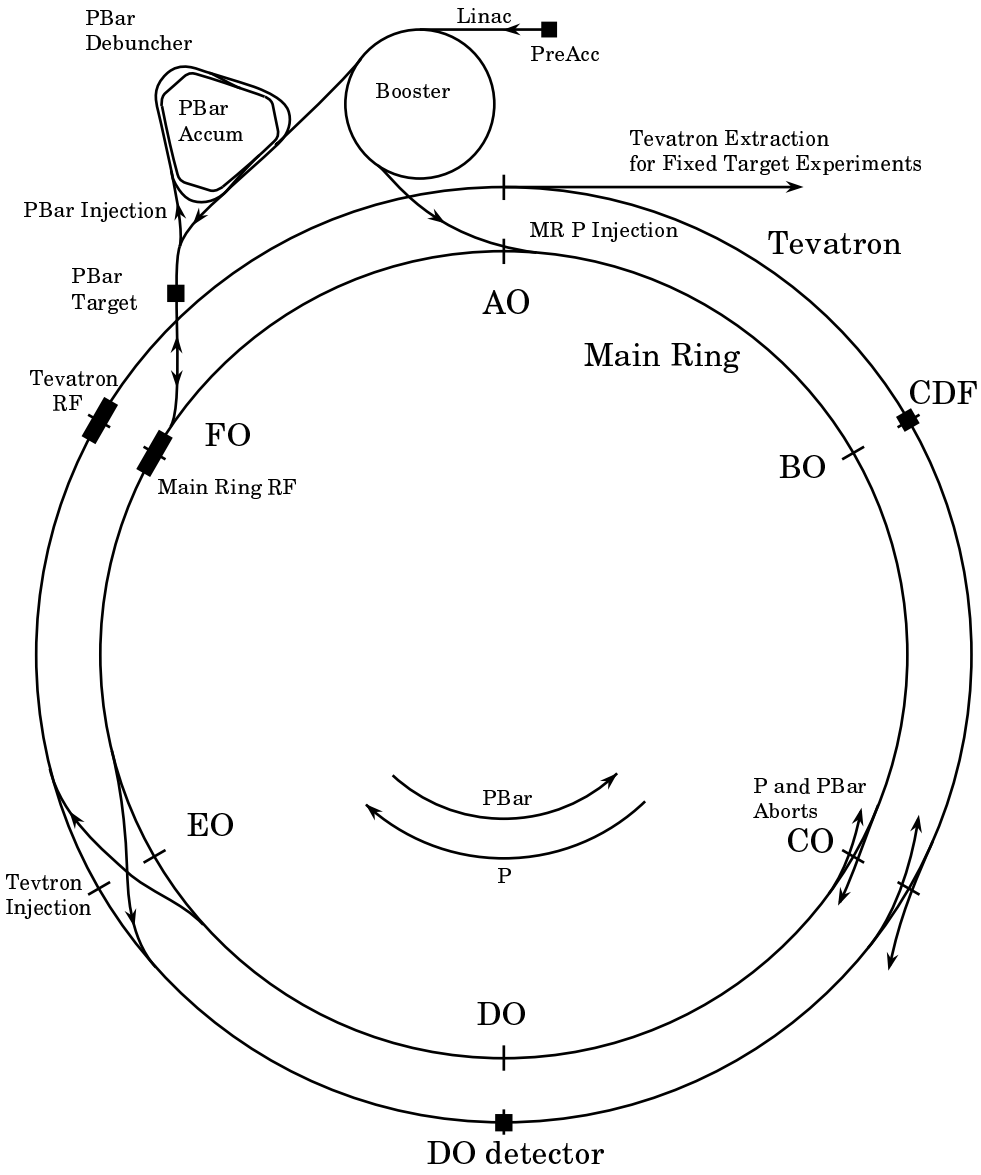

Figure 3.1: Schematic of the Fermilab accelerator complex.

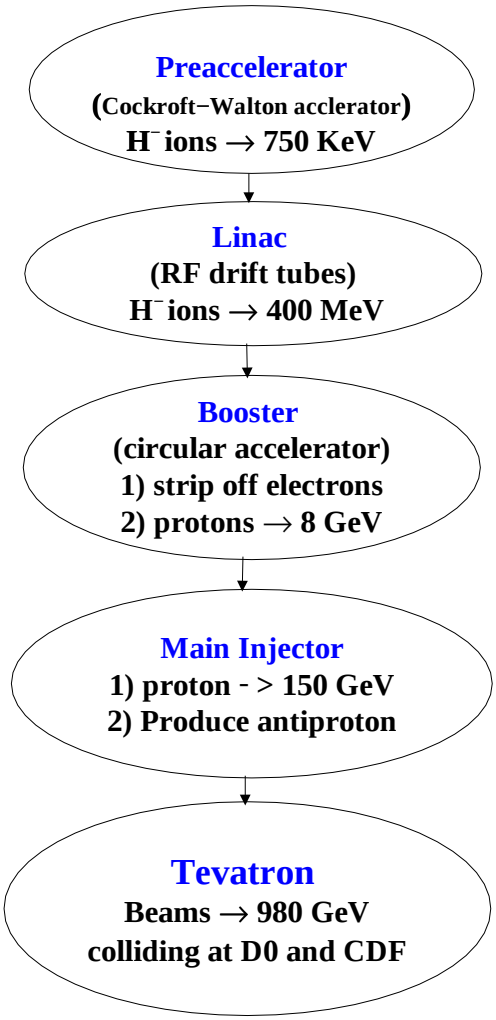

Figure 3.2: The generation of the $p\bar{p}$ colliding beams at the Fermilab collider

and transported to the start of the Linac. The Linac takes the Preacc beam and accelerates it to 400 MeV using Radio Frequency (RF) drift tubes arranged in a straight line. After emerging from the Linac, the ions enter the Booster. Located 6 m below ground, the Booster is an approximately circular accelerator with a 75 m radius that contains magnets and 18 RF cavities. In the Booster, the ions are stripped of their electrons by passing through a carbon foil, leaving bare protons. The protons are then accelerated to 8 GeV and injected into the Main Injector (MI). The Main Injector is a circular accelerator that is a little more than half the circumference of the Tevatron. It contains various magnets and 18 RF cavities. It serves two functions: 1) accelerate protons to 150 GeV; 2) accelerate protons to 120 GeV as a preparation for the production of antiproton.

The antiproton is produced by the Antiproton Source. The Antiproton Source consist of three components: Target, Debuncher and Accumulator. The 120 GeV protons extracted from the Main Injector are directed onto a target of nickel. The result is a spray of particles, some of which are antiprotons (It takes one hundred thousand to one million protons to make a single antiproton.). The emerging particles pass through a solid Li cylinder along its axis. The Li cylinder carries large pulses of current (500,000 A) anti-aligned with the particle moving direction. The result is that all negatively charged particles are focused, and all positively charged particles are de-focused. The Debuncher is a storage ring. It accepts 8 GeV antiprotons and rotates the antiproton bunches until they have

small momentum uncertainty and become denser beam. The antiprotons are transferred into the Accumulator before the next cycle of antiproton production from the Main Injector, which occurs at 2.4 second intervals.

The final phase in the life cycle of protons and antiprotons is injection into the Tevatron. The Tevatron is a circular synchrotron made from superconducting magnets [19], having a circumference of about 6400 m. The protons traveling at almost the speed of light require 21 μs to complete one revolution. The Tevatron is filled with 36 bunches of protons and 36 bunches of antiprotons from the Main Injector, traveling in opposite directions. The Tevatron finally accelerates both beams to 980 GeV before they are guided to head-on collisions at the center of the DØ and CDF detectors.

3.1.2 Luminosity and Cross Section

In colliding-beam machines, interaction rates are measured in terms of the instantaneous luminosity, L, which is given by:

$$L = \frac{N_p N_{\bar{p}} B f_0}{4\pi A}, \tag{3.1}$$

in the case of $p\bar{p}$ collisions. Here N_p is the total number of protons per bunch, $N_{\bar{p}}$ is the total number of antiprotons per bunch, B is the number of bunches of each type, f_0 is the frequency of bunch revolution (47.7 kHz), and A is the effective area of the bunches ($\sim 3 \times 10^{-5}\ cm^2$). The interaction rate, R, is related to the

instantaneous luminosity, L, by:

$$R = \sigma L, \tag{3.2}$$

where σ is the cross section of the particular interaction, and is a measure of the probability of its occurrence. Cross sections are often expressed in *barns*, where $1\,\text{barn} = 10^{-24}\,\text{cm}^2$. The number of events (N) of a specific type expected after running an experiment for a period of time is found by integrating the luminosity with respect to time:

$$N = \sigma \int L dt. \tag{3.3}$$

The quantity $\int L dt$ is called *integrated luminosity*.

3.1.3 The DØ Run II upgrade

The DØ detector was first proposed in 1983 and completed in early 1992. It weighs 5500 tons and measures 13 m (height) x 11 m (width) x 17 m (length). It was constructed to study high p_T and high mass phenomena in high energy physics. The total integrated luminosity for Run I was measured to be 130 pb^{-1}. Based on these data, DØ has published more than 120 papers and obtained many exciting results, including the discovery of the top quark. A full description of Run I DØ detector can be found in Ref. [20].

The DØ Run II project was proposed in 1990, before the detector began its first run of data taking. The DØ Run II project will increase the luminosity to

$2\times10^{32}\ cm^{-2}s^{-1}$, which is 20 times higher than that in the DØ Run I project. The physics motivations behind it are studies of low cross-section, high-p_T processes, such as top and W/Z particles, and search for new phenomena. To gain the high luminosity, more proton and antiproton bunches are filled in each revolution, The bunch crossing time is thus shortened from 3.5 μs in Run I to 396 ns. The much shorter bunch crossing time requires a much faster responses from each subsystem of the DØ detector. Figure 3.3 shows an overview of the DØ Run II detector. The major upgrades [18] of the DØ Run II project are listed below:

1. A new tracking system, including a silicon tracking detector and a central fiber tracking detector.

2. The addition of a 2-Tesla magnetic field to measure the momentum of charged particle tracks.

3. A forward tracking system based on silicon strip detectors, thereby increasing the pseudorapidity to 3 for reconstructed tracks.

4. A new three-level trigger system replaces the old trigger system to handle the higher data acquisition rate.

The following sections discuss the subsystems of the DØ detector, including the central tracking system, the superconducting solenoid, the calorimeter detector, the preshower detector, the muon system, the trigger and data acquisition

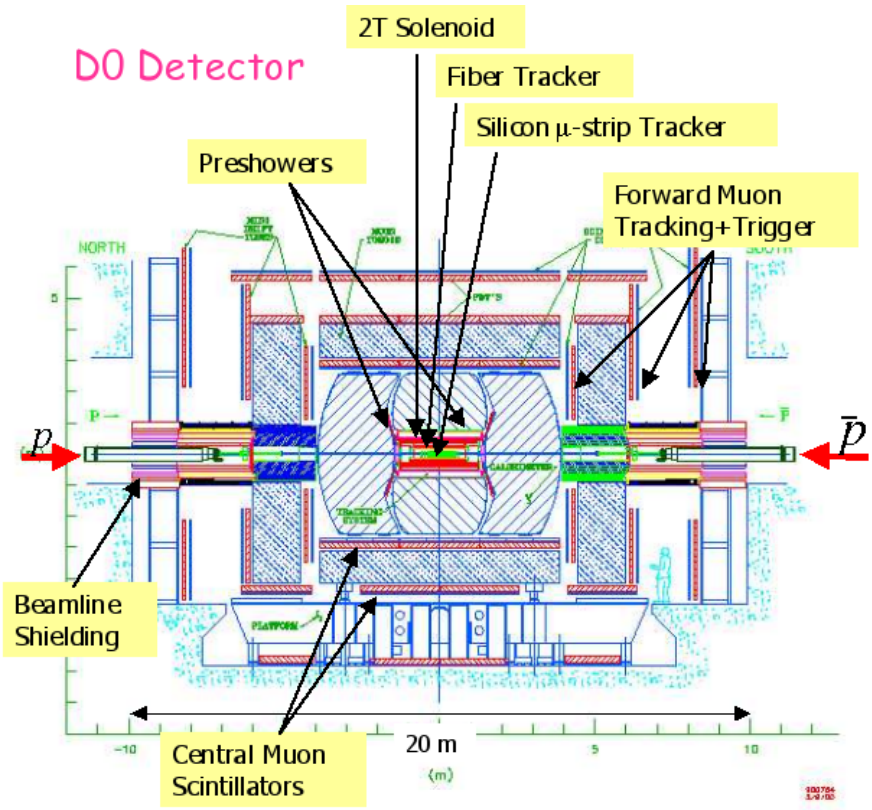

Figure 3.3: The r-z view of the DØ Run II detector

system.

3.2 The Tracking System

The DØ tracking system consists of a Silicon Microstrip Tracker (SMT) [48] and a central fiber tracking detector (CFT) [25]. We first describe the DØ coordinate system, then give a detailed description of the two tracking detectors.

3.2.1 DØ Coordinate System

DØ uses a right-handed coordinate system with the positive z-axis pointing along the direction of the proton beam, and the positive y-axis vertically upward. The azimuthal angle (ϕ) is defined such that $\phi = 0$ is aligned along the x-axis, and $\phi = \pi/2$ is aligned along the y-axis. The polar angle (θ) is defined such that $\theta = 0$ is aligned along the z-axis. The radial distance is measured perpendicular to the z-axis.

A reconstructed track is defined by 5 parameters that can be used to extract all of the kinematic variables. These parameters are the Distance of Closest Approach (DCA) to the primary vertex, the z position of the DCA, ϕ_0 at the DCA, $\tan(\lambda)$ and q/p_T, where $\tan(\lambda)$ is defined as p_z/p_T, p_z is the momentum in z direction (longitudinal momentum) $p_z = p\cos\theta$, p_T is the momentum transverse to the beam axis $p_T = p\sin\theta$, q is the charge.

Instead of the polar angle θ, one generally uses the rapidity y of a particle defined as

$$y = \frac{1}{2}\log(\frac{E + p_z}{E - p_z}) \tag{3.4}$$

where E is the energy. The advantage of using the rapidity is that a Lorentz boost in the z direction to a frame with velocity β just adds a constant ($\tanh^{-1}\beta$) to the rapidity, making rapidity differences invariant. Hence the shape of the rapidity distribution dN/dy is invariant. If the energy of a particle is much larger than its mass, the pseudorapidity η becomes a very good approximation to y

$$\eta = -log(tan\frac{\theta}{2}) \tag{3.5}$$

3.2.2 The Silicon Microstrip Tracker (SMT)

The SMT detector is the first detector that most of the collision-produced particles encounter. The detector can reconstruct charged particle tracks in both central ($|\eta| < 1.7$) and forward ($1.7 < |\eta| < 3.$) region. The reconstruction of the forward tracks provides a more detailed picture of the decay products in an event and therefore improves the potential abilities in many analysis. For example, based on our Monte Carlo studies of the opposite side jet charge tagging algorithm, the inclusion of forward tracks increases the tagging dilution by at least 30% for the neutral B sample. (The tagging dilution is given by $2 * P - 1$, where

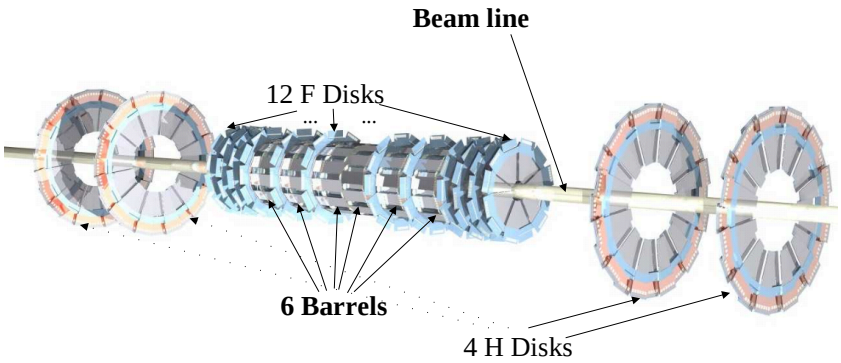

Figure 3.4: DØ Run II Silicon Microstrip Tracker detector.

P is the probability of tagging an event correctly. The tagging dilution will be discussed in detail in the next charpter.)

The SMT detector is shown in Fig. 3.4. It consists of six 12 cm long barrels with interspersed disks for forward track reconstruction. Each barrel (see Fig. 3.5) consists of 4 radial layers of detector ladder assemblies. Barrel layers one and three consist of double-sided silicon microscrip detectors (except that the two outer barrels are constructed by single sided silicon detectors) with axial strips on the p-side and 90° stereo strips on the n-side, where p- and n-side refer to positively and negatively doped strips of silicon respectively. Layers two and four are all constructed by double sided silicon detectors with a 2° stereo angle. The

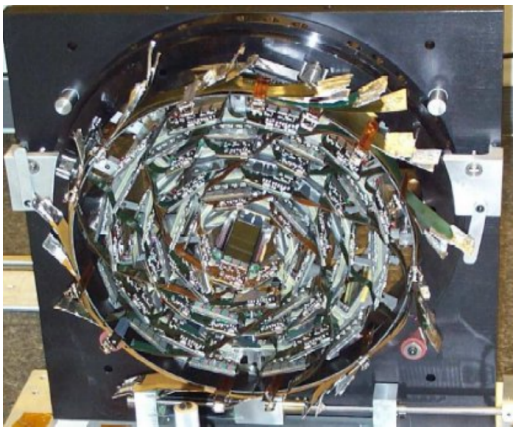

Figure 3.5: A picture of DØ SMT barrel.

disks consists of twelve "F-disks" and four "H-disks". Each disk has 12 wedge shaped double sided silicon detectors with a 30° stereo angle.

In the central region, the SMT tracks are matched to the CFT tracks (discussed in next section) to make global tracks. The global track reconstruction will be discussed in detail in the next chapter.

Located in the innermost layer, the SMT is affected by radiation damage the most. Radiation damage causes increase in leakage current and demands application of higher bias voltage. A radiation monitoring system has been designed, built and installed to monitor the radiation environment inside SMT. The SMT technology has been shown to be sufficiently radiation hard [23].

	F	H	L1	L2	L3	L4	TOTAL
# detector sides	2	1	1	2	1	2	
# assemblies (both sides)	12	4	7	7	7	7	44
R (min) (cm)	2.57	9.5	2.77	4.61	6.83	9.16	
R (max) (cm)	9.96	26	3.58	5.49	7.52	9.99	
$\|z\|$ (min) or $<dz>$ (cm)	6.4	110	$<12>$	$<12>$	$<12>$	$<12>$	
$\|z\|$ (max) (cm)	54.8	120	42	42	42	42	
# ladders/assembly	12	24	12	12	24	24	
Detector length (cm)	7.5	14.86	6	6	6	6	
Min. detector width (cm)	1.673	2.42	2.115	3.395	2.115	3.395	
Max. detector width (cm)	5.692	6.40	2.12	3.40	2.12	3.40	
Detector area (cm^2)	27.62	65.53	12.72	20.4	12.72	20.4	
Strip pitch (μm)	50	50	50	50	50	50	
# IC's/side	8	10	3	5	3	5	
# detectors/readout unit	1	2	2	2	2	2	
# detectors/assembly	12	48	24	24	48	48	
# detectors (total)	144	192	168	168	366	366	1344
Silicon mass (g)	278	440	149	240	299	479	1885
Sides×area (cm^2)	7954	7528	2137	6854	4274	13709	41222
# sets IC's/assembly	24	24	12	24	24	48	
# sets IC's	288	96	84	168	168	336	
# IC's	2304	960	252	840	504	1680	6540
# kchannels	294.9	122.9	32	108	65	215	837

Table 3.1: The numbers of detectors and geometric parameters of the SMT detector.

The number of individual silicon detectors and geometric parameters are summarized in table 3.1.

3.2.3 The Central Fiber Tracking Detector (CFT)

The Central Fiber Detector is shown in Fig. 3.7. It has a total of 76,800 scintillating fibers. Sixteen fiber doublet layers (See Fig. 3.6) are mounted on eight concentric cylinders with radii from 20.0 cm to 51.6 cm. There are 8 axial

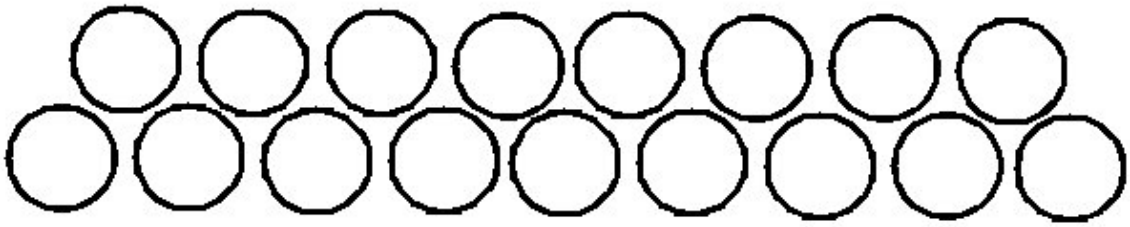

Figure 3.6: The cross section of a segment of a single CFT layer.

layers and 8 stereo layer. The axial layers (labeled as x) provide the ϕ information of a track, and the stereo layers (u/v, one layer tilts 2° from the z axis clockwise, the other tilts 2° counter clockwise) provides the η information. The order of the layers is $xu - xv - xu - xv - xu - xv - xu - xv$. Table 3.2 summarizes the parameters of each layer of the detector.

The CFT detector surrounds the SMT detector and covers the central pseudorapidity region up to 1.7. It serves two man functions: 1) combined with SMT barrel detector, helps reconstruct the global tracks. 2) Provides fast trigger with the level 1 (L1) track, i.e. L1CTT [26].

The detector is divided into 80 sectors in ϕ for the preparation of the level 1(L1) trigger tracks. The first sector starts from $\phi = 0$ to $\phi = 4.5°$. Each sector has 896 fibers. Each fiber is 835 microns in diameter. This gives the tracker sufficient granularity to trigger and reconstruct tracks in the complex event environments in Run II. The doublet layer position resolution is on the order of 100 μm, corresponding to a ϕ resolution of 2×10^{-4} radian.

Layer	Radius cm	# of Fibers per sector	# of Fibers per layer	# of Fiber Ribbons	Fiber pitch in microns	Active length (m)
A	19.99	16	1280	10.0	979.3	1.66
AU	20.15	16	1280	10.0	987.2	1.66
B	24.90	20	1600	12.5	975.8	1.66
BV	25.60	20	1600	12.5	982.1	1.66
C	29.80	24	1920	15.0	973.4	2.52
CU	29.97	24	1920	15.0	978.6	2.52
D	34.71	28	2240	17.5	971.7	2.52
DV	34.87	28	2240	17.5	976.2	2.52
E	39.62	32	2560	20.0	970.4	2.52
EU	39.78	32	2560	20.0	974.4	2.52
F	44.53	36	2880	22.5	969.5	2.52
FV	44.69	36	2880	22.5	972.9	2.52
G	49.43	40	3200	25.0	968.7	2.52
GU	49.59	40	3200	25.0	971.8	2.52
H	51.43	44	3520	27.5	916.1	2.52
HV	51.59	44	3520	27.5	919.0	2.52

Table 3.2: Parameters of the Central Fiber Tracker. There are 16 layers of fibers altogether. Layers 1 through 8 are labeled as A through H. U and V correspond to the stereo layers, while the others are the axial layers.

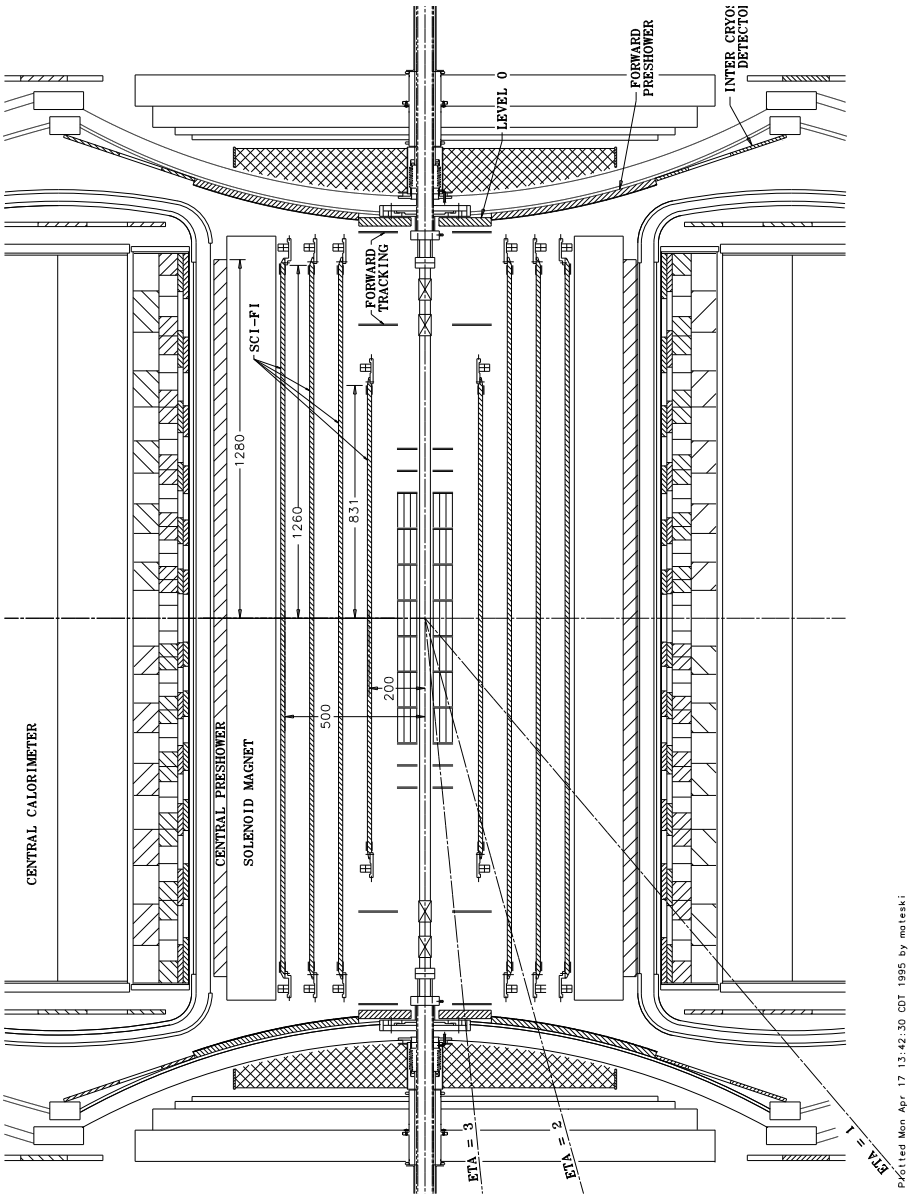

Figure 3.7: The side view of the central tracking system.

Each scintillating fiber is mirrored on one end and connected at the other end, through an optical connector, to a clear fiber wave guide that pipes the scintillation light to a Visible Light Photon Counter (VLPC) [27]. The VLPC consists of small silicon chips that convert the photons to electrical signal with a gain at about 20,000 to 60,000. The high gain enables the VLPC to measure a single photon. To keep low level of noises, the VLPC chips operate at 9 degrees Kelvin.

3.3 The Superconducting Solenoid

The momenta of charged particles are determined from their curvatures in the 2-Tesla magnetic field provided by a 2.7 m long solenoid magnet. The superconducting solenoid (SC) has two layers of coils with mean radius of 60 cm. It stores magnetic energy of 5 MJ (for reference the CDF coil is 30 MJ). Inside the tracking volume, the solenoid is uniform to within 0.5%. This is the first thin solenoid for use in a particle physics detector that operates at 2T.

An electrical energization, control and protection system controls the run of the solenoid. The system allows switching the polarity of the magnetic field to minimize potential asymmetry in the detector configurations.

3.4 The Calorimeter Detector

The calorimeter measures the energy of particles that enter it. The calorimeter is mostly used in the jet (a cluster of particles) related analysis by measuring the jet energy. It is not used in this analysis. We elaborate on it just for a complete description of the DØ detectors. In this section, we first describe the energy measurement in calorimeter, then describe the DØ calorimeter and its energy resolution.

3.4.1 Energy Measurement

As a particle passes through the calorimeter, it produces electromagnetic (EM) and/or hadronic showers in the absorber plate. The EM showers are primarily produced by the emission of photons due to the deceleration of highly energetic electrons passing the Coulomb field around the nucleus of the absorber plate (Bremsstrahlung process), or the creation of e^+e^- pairs from photons (pair production process)[34]. The energy loss of an EM particle passing through a specified amount of material is determined by the material's **radiation length** (X_0),

$$E(x) = E_0 e^{-X/X_0} \tag{3.6}$$

Generally, material with higher atomic numbers has smaller radiation length, for example Uranium's radiation length is 3.2 mm.

The hadronic shower is dominated by a succession of inelastic hadronic interactions[35]. At high energy, these are characterized by multi-particle production and particle emission originating from nuclear decay of excited nuclei. Due to the relatively frequent generation of π^0's (most of them decay to two photons), there is also an electromagnetic component presents in hadronic showers. The hadron's mean free path between interactions in the medium is called **the nuclear interaction length** λ_0. Uranium's interaction length is about 10 cm. Consequently, hadronic showers are generally larger, both longitudinally and transversely, than the electromagnetic showers.

3.4.2 The DØ Calorimeter Detector

DØ has a liquid argon sampling calorimeter[30][31][32][33]. It consists of a stack of interleaved absorber plates and signal boards (called modules), each pair of the absorber plate and the signal board forms a unit cell, see Fig. 3.8. Each cell consists of a liquid argon cap between an absorber plate and a G10 board. The G10 board has a high-resistivity coating to which a potential is applied with respect to the absorber plate to create the drift field. When a particle enters the calorimeter, it showers inside the absorber plate and the particles from the shower ionize the argon atoms. In the electric field the ionized electrons drift toward the G10 coating, producing a current. The current induces charges on

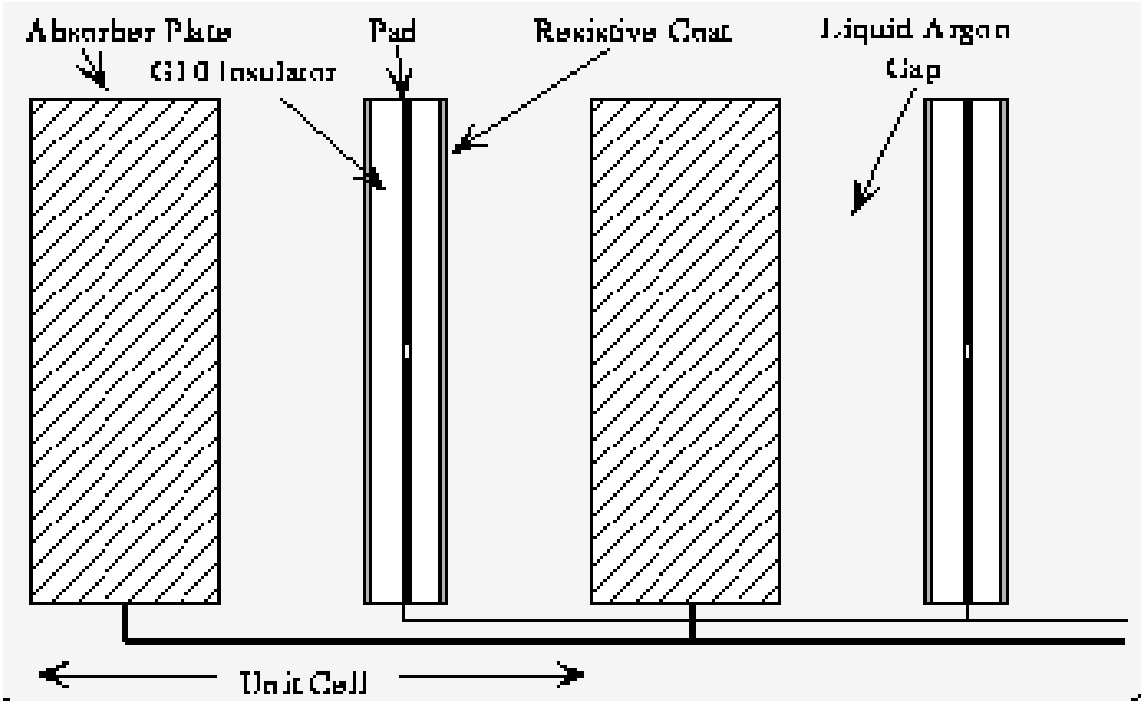

Figure 3.8: Schematic view of a calorimeter cell.

a copper pad etched on the G10 board under the resistive coat. The readout currents are preamplified and produce voltages. Several unit cells are stacked on top of each other to create a layer in the calorimeter. All the cells in the layer are readout together.

Reading out all calorimeter electronic channels (about 60,000 channels) will cause long readout time and big size events. To keep the readout time and event size at reasonable level, the calorimeter electronics are generally read out in the zero suppression mode, which ignores those channels with zero energy deposit. This does not cause any loss of information. However, due to the radiation background (from the depleted uranium absorber in the calorimeter detector),

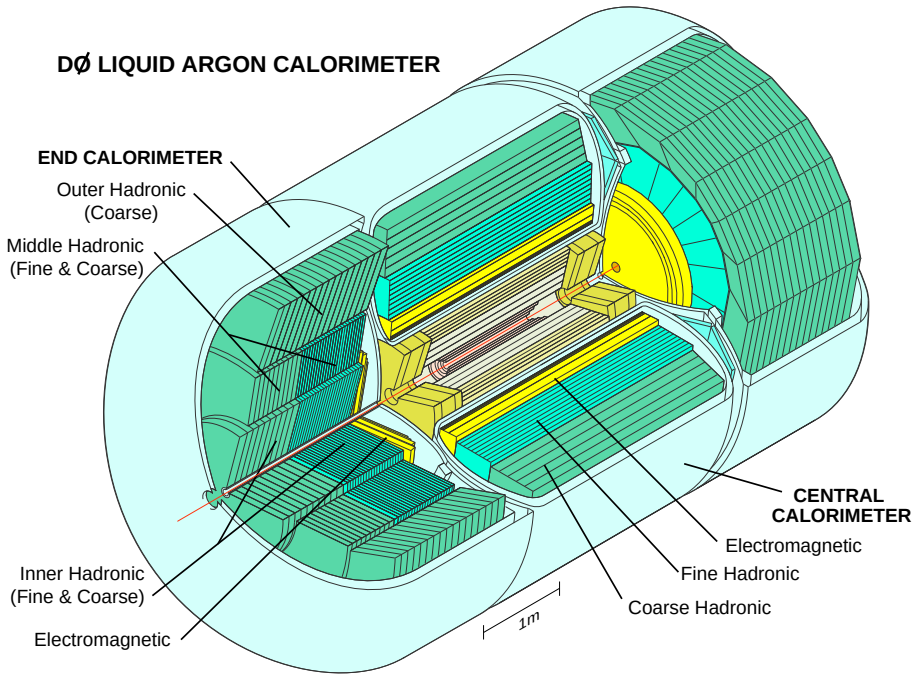

Figure 3.9: The DØ calorimeter detector full view, with Cut-away.

non-zero energy is measured in channels even when there is no beam colliding. Therefore a zero suppression cut is applied to all channel readout. The cut is determined by the width of the pedestal for each channel which is measured in special detector runs.

The calorimeter detector consists of three units (see Fig. 3.9), the Central Calorimeter (CC) covering the region of $|\eta| < 1.2$, the two End-cap Calorimeters (EC) providing complete pseudorapidity coverage up to 4, and the Intercryostat Detector (ICD) covering the overlapping region between CC and EC.

The central calorimeter (CC) consists of three cylindrical concentric shells parallel to the beam line from 75 cm to 222 cm in radial direction. The three

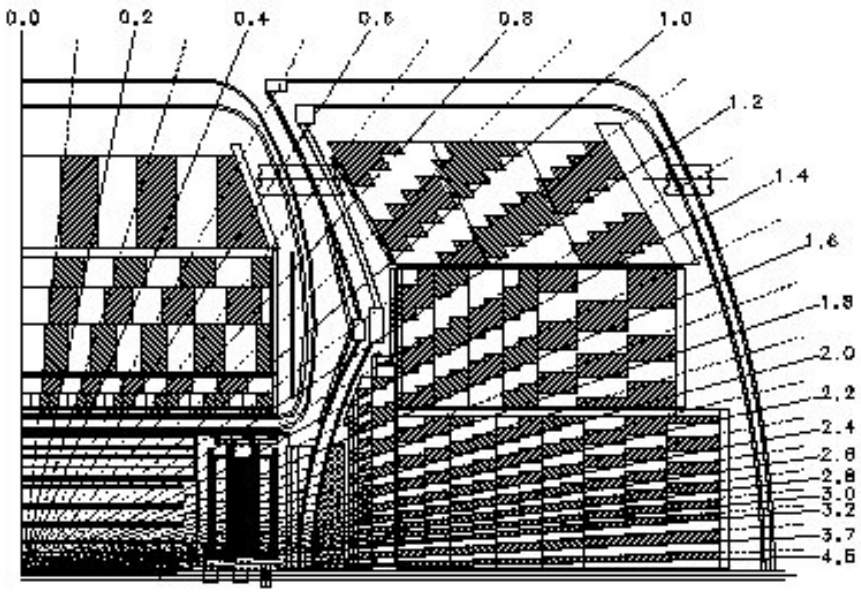

Figure 3.10: The side view of a quarter of the calorimeter detector.

sections are the electromagnetic (EM), the fine hadronic (FH) and the coarse hadronic (CH) ring. The EM modules are arranged in four radial readout layers, corresponding to 2.0, 2.0, 6.8, 9.8 radiation length (X_0). The FH modules are arranged in three radial readout layers, corresponding to 1.3, 1.0, 0.9 nuclear interaction length (λ_0). The CH modules are arranged in one radial readout layer, corresponding to 3.2 λ_0. Table 3.3 lists the major design specifications.

The readout layers of the CC are arranged into pseudoprojective towers of size 0.1×0.1 in $\Delta\eta \times \Delta\phi$ (see Fig. 3.10). Each tower consists set of cells having the same pseudorapidity. To optimize the ability to distinguish between EM and hadronic showers, the third layer of the EM section, which corresponds to the EM shower maximum, is segmented more finely into 0.05×0.05 in $\Delta\eta \times \Delta\phi$.

Module type	EM	FH	CH
Rapidity coverage	±1.2	±1.0	±0.6
Number of modules	32	16	16
Absorber [a]	DU	DU-Nb	Cu
Absorber thickness (mm)	3	6	46.5
Argon gap (mm)	2.3	2.3	2.3
Number of signal boards	21	50	9
Number of readout layers	4	3	1
Cells per readout layer	2,2,7,10	20,16,14	9
Total radiation lengths (X_0) [b]	20.5	96.0	32.9
Total nuclear absorption lengths (λ) [b]	0.76	3.2	3.2
Sampling fraction (%)	11.79	6.79	1.45
Total readout cells	10,368	3000	1224

[a] Depleted uranium (DU), depleted uranium with 1.7% niobium (DU-Nb), or copper (Cu).

[b] At $\eta = 0$.

Table 3.3: The central calorimeter Parameters.

Module type	EM	IFH	ICH	MFH	MCH	OH
Rapidity range	1.3–3.7	1.6–4.5	2.0–4.5	1.0–1.7	1.3–1.9	0.7–1.4
No. of modules	1	1	1	16	16	16
Absorber [a]	DU	DU-Nb	SS	DU-Nb	SS	SS
Thickness (mm)	4	6	6	6	46.5	46.5
LAr gap (mm)	2.3	2.1	2.1	2.2	2.2	2.2
Signal boards	18	64	12	60	14	24
R.O. layers	4	4	1	4	1	3
Cells/r.o. layer	2,2,6,8	16	14	15	12	8
Total rad. len.	20.5	121.8	32.8	115.5	37.9	65.1
Total abs. len.	0.95	4.9	3.6	4.0	4.1	7.0
Samp. frac. (%)	11.9	5.7	1.5	6.7	1.6	1.6
Tot. r.o. cells	7488	4288	928	1472	384 + 64 + 896 [b]	

[a] Depleted uranium (DU), depleted uranium with 1.7% niobium (DU-Nb), or stainless steel (SS).

[b] MCH and OH cells are summed together at $|\eta| = 1.4$

Table 3.4: The End-cap calorimeter Parameters.

The two End-cap calorimeters (EC) are located on both sides of the central calorimeter. They are similar to the CC, but with somewhat different layers, segmentations and materials. The End-cap calorimeter are divided into four sections: the forward electromagnetic (EM), the inner hadronic (IH), the middle hadronic (MH), and the outer hadronic ring (OH). Table 3.4 lists the major design specifications for the EC.

In the crossover region between the central calorimeter and the End-cap calorimeter, there are several rapidity regions where the structure and support

mechanical system are placed (e.g cryostat walls), creating a gap between CC and EC in the z direction. In the gap, there is substantial amount of absorption material, but no energy sampling module. To partially compensate for the energy loss in these support material two different types of detectors were adopted: the Inter-cryosts Detector (ICD), consisting of two arrays of 384 scintillation counter tiles, is mounted on the front surface of each EC cryostat to sample the energy. An additional layer of LAr sampling was positioned inside the CC and EC cryostat walls. These Massless Gaps (MG) have no significant absorber material but do sample the shower as it develops between the CC and the EC.

3.4.3 Energy Resolution

Only the energy deposited by particles in the liquid argon from the ionization process is detected. It is a small fraction of a particle's energy. The full energy can be obtained by using a number of calibration processes. The calorimeter's response to single electron and pion has been tested by using test beams before Run I experiment. For the energies between 10 to 150 GeV, the calorimeter's response is found to be linear to within 0.5%. The energy resolution was measured to be

$$\textbf{For electron}: \quad \frac{\sigma_E}{E} = \sqrt{0.3\%^2 + \frac{15\%^2}{E}} \tag{3.7}$$

$$\textbf{For pion}: \quad \frac{\sigma_E}{E} = \sqrt{4.0\%^2 + \frac{45\%^2}{E}} \tag{3.8}$$

In Run II experiments, because of the newly added detectors between the beam pipe and the calorimeter detector, the resolutions are expected to become worse. But a fully functioning preshower detector is expected to compensate and even make the resolution better. To re-calibrate, $Z \rightarrow ee$ and $J/\psi \rightarrow ee$ processes have been used, with the work still in progress.

3.5 The Preshower Detectors

The primary purpose of the preshower detectors is to provide discrimination between electrons/photons and those of the dominant backgrounds (principally hadronic jets) by exploiting the differences between their energy loss mechanisms in showers. It helps increase, at both L1 and L2 triggers, the rejection rate of fakes of QCD origin.

The preshower detectors consist of a central preshower detector (CPS) [28] covering $|\eta| < 1.3$ and a forward preshower detector (FPS) [29] covering $1.5 < |\eta| < 2.5$. Figure 3.11 shows an overview of the CPS detector. It consists of a lead layer and three layers of scintillating strips. The three layers of triangular shaped strips (see Fig. 3.12) have one axial and two stereo layers. The stereo layers have a 20° stereo angle. The CPS detector is placed immediately outside the solenoid and inside the calorimeter at a radius of about 72 cm.

The solenoid and the lead layer serve as the pre-radiator. As a particle passes

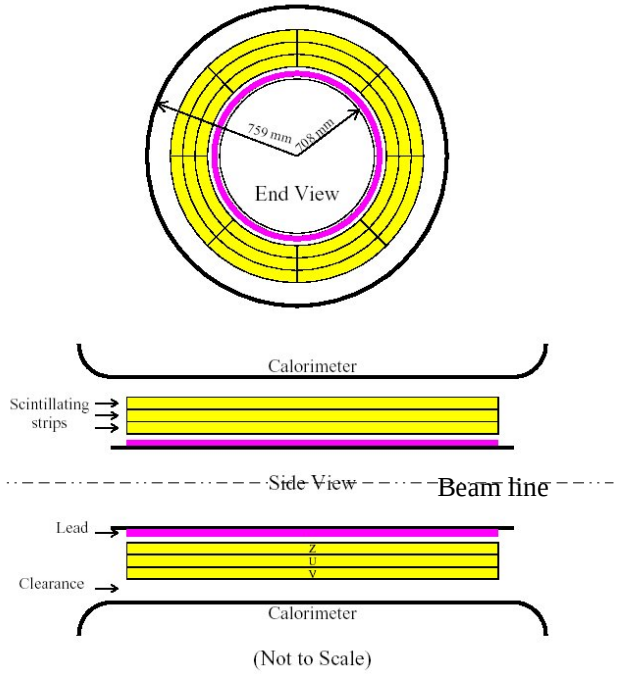

Figure 3.11: The CPS detector.

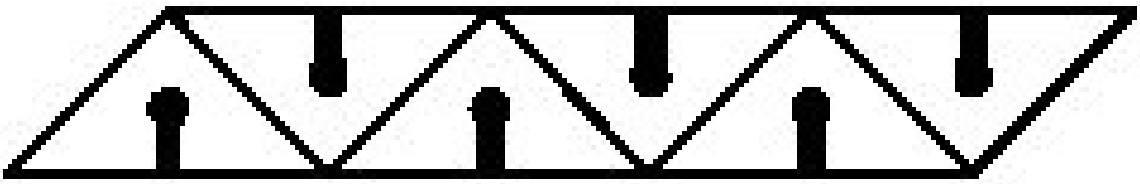

Figure 3.12: The triangularly shaped CPS strips

through the pre-radiator, it produces electromagnetic and/or hadronic showers. It should be noted that the solenoid is not an ideal pre-radiator due to its aluminum component, which contributes a nuclear interaction length from .2 to .35 for η from 0 to 1.4. Therefore the lead layer is shaped to become thinner with increasing η, keeping a constant 2 radiation lengths in the all covered pseudo-rapidity region. All charged particles that traverse the CPS detector register a hit. Electrons/photons shower readily in the pre-radiator and produce maximum-ionizing tracks in the rear layers. Charged pions and muons tend not to shower in the pre-radiator, therefore produce minimum-ionizing tracks in the rear layers.

The FPS detector consists of two pieces, mounted on the End-cap Calorimeters. Each piece has four scintillator layers, inner U and V layers and outer U and V layers, see Fig. 3.13. There is a lead absorber plate of two radiation lengths between the inner and outer layers. The inner layers usually detect minimum-ionizing particles, or MIPs, while the outer layers detect the EM showers produced by electrons/photons after traversing the absorber plate. Because of this, the layers are often referred to as the MIP and shower layers. Electrons produce hits at both of the MIP and shower layers. Charged pions also produce two hits, but the signal at the shower layer is much smaller. Photons, whether directly produced or resulting from π^0 decays, will be identified by the presence of a hit in the shower layer, and the absence of a spatially-matched hit in the MIP layer.

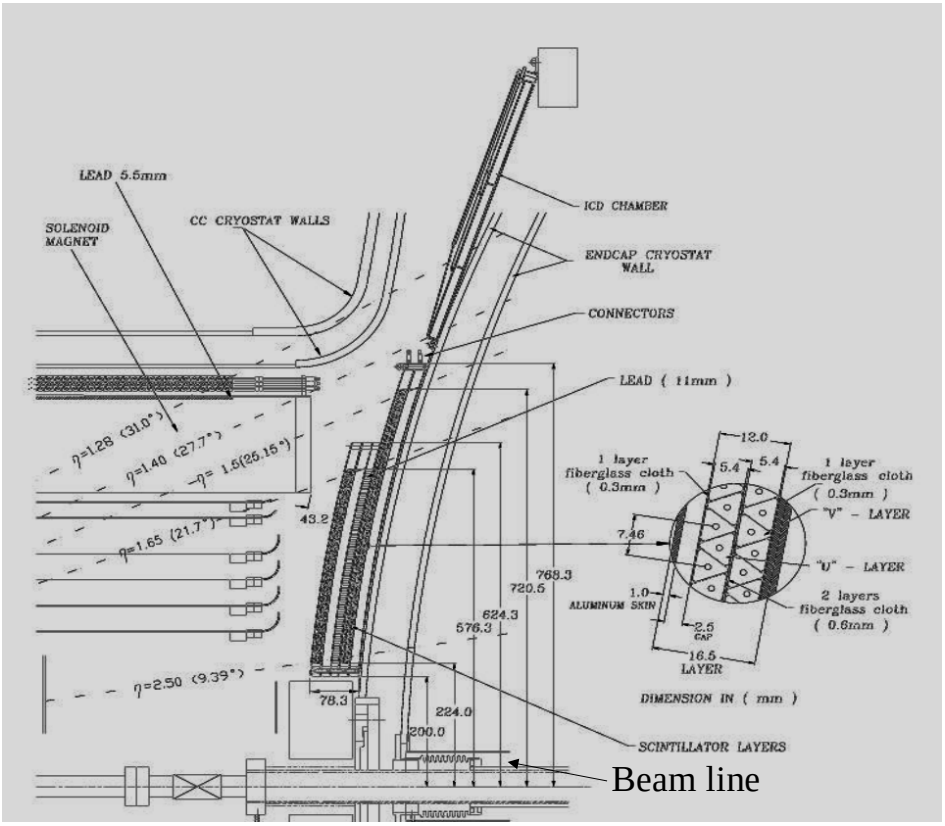

Figure 3.13: One quarter r-z view of the FPS detector.

As the calorimeter, the preshower detector is not used in this analysis neither.

3.6 The Muon System

Most of the particles from $p\bar{p}$ collisions are absorbed by the thick absorbers (formed mainly by the solenoid and calorimeter). In order to penetrate the absorbers, a particle must satisfy the following three requirements: 1) have lifetime sufficient to travel several meters before decaying, 2) not interact strongly with materials, 3) not readily produce bremsstrahlung radiation. The only charged particle known to meet the requirements is the muon. Therefore, The muon system is located at the outer-most layer of the DØ detector. Any charged particle that penetrates the absorbers and reach the muon system is assumed to be a muon.

The muon system is critical in obtaining the data sample used in this analysis. All B physics studies rely on the muon triggers (di-muon/single muon trigger). The data samples used in this analysis are mostly from the following two di-muon triggers: *2MU_A_L2ETAPHI* and *2MU_C_2L2_2TRK*. The triggers will be discussed in detail in next section.

The muon system has three subsystems: the central muon detector (made of Proportional Drift Tubes - PDTs [37]) , the forward muon detector (made of Mini-Drift Tubes - MDTs) and trigger scintillation counters, see Fig. 3.14.

The muon system covers a pseudorapidity region of $|\eta| \leq 2.0$. The central muon detector were used in Run I, providing pseudorapidity coverage of $|\eta| \leq 1.0$. The forward muon detector extends muon detection to $|\eta| = 2.0$ in DØ Run II. Scintillation counters are used for triggering and rejection of cosmic muons and accelerator background. Shielding around the beam pipe from the edge of the End-cap calorimeter to the accelerator tunnel are added to further reduce the background.

Each muon detector has three layers (A, B and C layers). The A layer is between the calorimeter and the 2 Tesla muon toroid magnet. The toroid magnet provides the magnetic field for the local muon momentum measurement. The B and C layers are outside the toroid. The central muon detector and forward muon detector are discussed in detail next.

3.6.1 The Central Muon Detector

The A layer chambers on the top and sides have 4 decks of PDT tubes to help reject backgrounds. On the bottom it only has three decks due to space constraints. The B and C layers have three decks each. The central muon detector consists of 94 PDTs of the Wide-Angle-MUon-System (WAMUS) [38][39]. Each PDT chamber is a rectangular aluminum tube with 5.7 cm $\times$ 10 cm cells.

The drift chambers produce the measurements for muon hits. The hit resolution from the sense wire is approximately 10 to 50 cm, depending on the hit location. The local momentum resolution has been studied in [40]. For muons with $pt > 4$ GeV/c, the resolution is given by $\frac{\sigma_p}{p} = \sqrt{(\frac{0.16(p-2)}{p})^2 + (0.02p)^2}$. This is significantly larger than the resolution of the global tracks. For example, for $p_T = 4$ GeV/c, the local muon resolution is 11%, the global track resolution is 1.6%. Therefore, each local muon track is to be matched with the global tracks. The kinematic variables of a muon track are drawn from a matched global track.

At trigger level, each muon object is assigned a quality from the following categories:

1. Tight: ≥ 2 wire hits in the A layer, ≥ 4 wire hits in the B and C layer, ≥ 1 scintillator hit in A and ≥ 1 scintillator hit in B or C layer, $\chi^2 \geq 0$.

2. Medium: ≥ 3 wire hits in the A layer, ≥ 2 wire hits in the B or C layer. ≥ 1 scintillator hit in B or C layer. $\chi^2 \geq 0$

3. Loose: ≥ 3 wire hits in the A layer, or ≥ 2 wire hits and ≥ 1 scintillator hit in A layer.

Muons traveling at 90 ° with $p_T > 1.5$ GeV/c can fire the A layer wires, but can not reach the B layer due to the absorption in the toroid. To pass through the toroid, it needs $p_T > 3$ GeV/c.

3.6.2 The Forward Muon Detector

As in the central region, the A layer of the forward muon detector has four decks of MDT drift tubes and the B and C layers have three decks each. The coordinate resolution is 0.7 mm/deck. The local momentum resolution of the forward detector is $\frac{\sigma_p}{p} = \sqrt{(\frac{0.2(p-2)}{p})^2 + (0.0085p)^2}$ [40]. For p_T is 4 GeV/c, the local muon resolution is about 11%. In the forward region of the muon system, the solenoid and calorimeter might not be in the path of a muon. The muon can reach the A layer with p_T lower than 1.5 GeV/c.

The scintillation counters are substantially less sensitive to backgrounds than gas detectors. This advantage cuts the gate width from 100 ns to 20 ns, reducing the number of background hits per plane by ten times, while keeping the muon detection efficiency at 100%.

3.7 The Trigger and Data Acquisition System

The proton-antiproton beams make about 1.7 million collisions per second at the center of the DØ detector. The information collected for each collision is called an event. Not every event can be saved due to the limited band width of writing events to tape. Moreover, not every event needs to be saved to tape. For some of the crossings, the proton and antiproton beams just pass through each other without generating interesting events. In the other crossings, the following

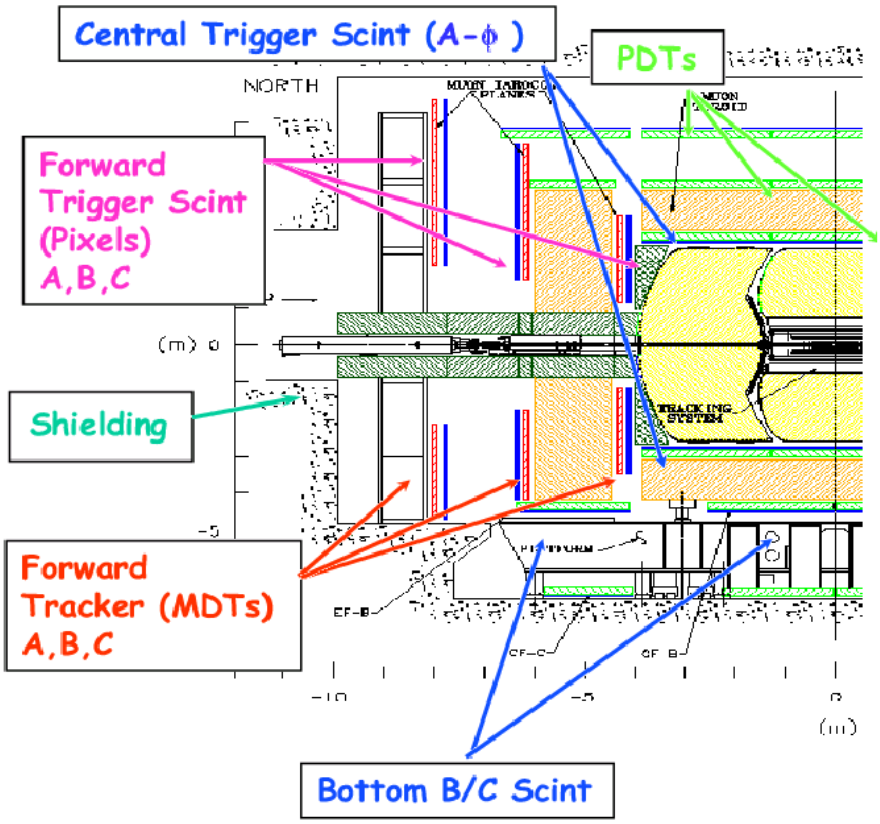

Figure 3.14: The r-z view of the half muon system.

interactions may happen: elastic scattering, single diffraction, double diffraction, and hard scattering. The events with hard scattering are of the most interest.

For DØ RunII, the rate of writing events to tape is 50 Hz, much smaller than the event rate from collisions. The job of selecting 50 events out of 1.7 millions events per second is done by the DØ trigger system [42]. DØ trigger system provides a number of triggers which select different types of events that are of the most interest to different physics analyses.

The DØ trigger system include three levels of triggering. The level 1 trigger (L1) is designed to have an output rate of 10 kHz, the level 2 trigger (L2) has an output rate of 2 kHz, and the level 3 trigger (L3) has an output rate of 50 Hz. We discuss each trigger in detail below.

3.7.1 The Level 1 Trigger

The current L1 trigger system is a hardware trigger system filtering the 1.7 MHz beam crossing rate with minimal dead time (less than 5% in normal desired running conditions). The L1 trigger system consists of the L1 Trigger Framework (L1FW, see Fig. 3.15) and the L1 trigger subsystems.

Each L1 trigger subsystem, for every beam crossing, processes detector-specific information from the detector front-end electronics (DFE) and passes the results to L1FW by the *And-Or Input Terms*. Each *And-Or* term is a binary

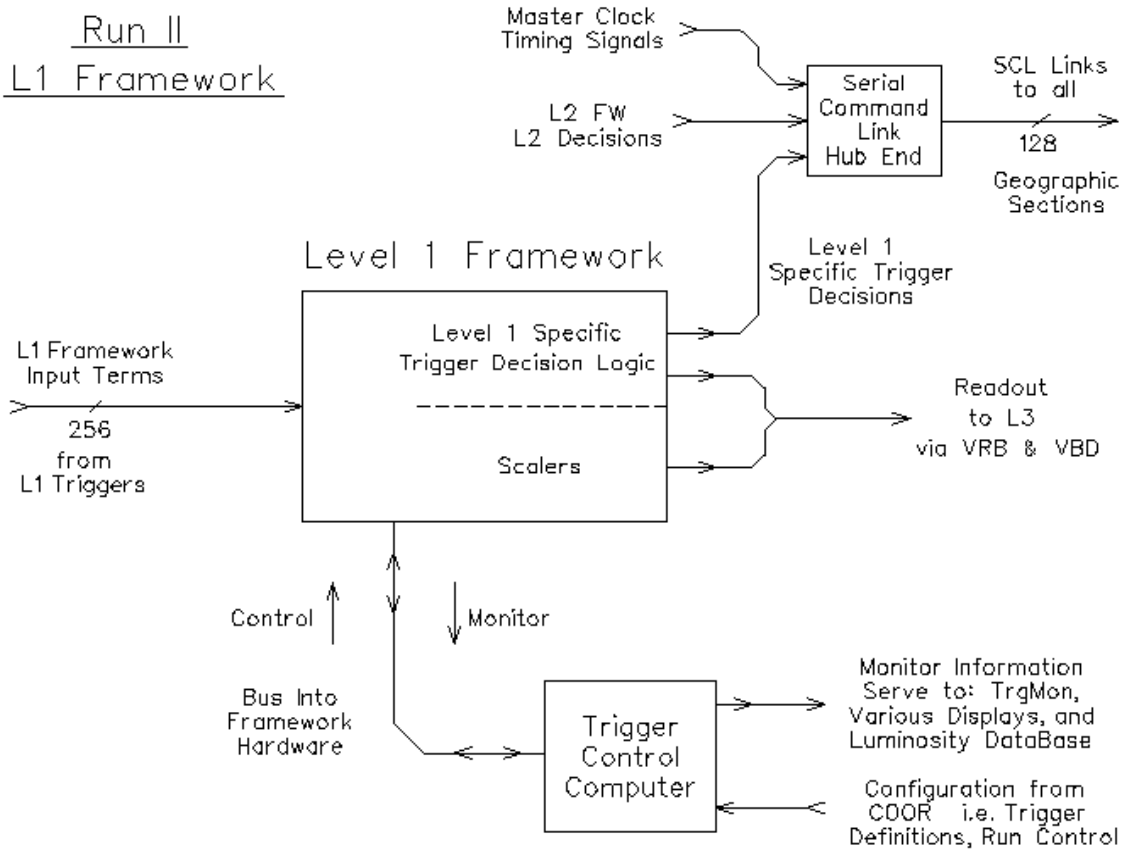

Figure 3.15: DØ Run II Level 1 Trigger Framework.

signal. There are a total of 256 *And-Or* terms available. The *And-Or* terms can also be used to bring information from other sources into L1FW, such as the general beam condition indicators and the cosmic background veto signals. One hundred twenty eight *Specific Triggers* are formed by evaluating 128 sets of the *And-Or* term combinations. The global L1 trigger decision is the logical .OR. of the 128 *Specific Trigger* decisions. For example, the trigger *2MU_A_L2ETAPHI* used for collecting events in this analysis uses four *And-Or Input Terms* to form the L1 trigger. This L1 trigger requires a di-muon trigger based on muon scintillator only and calorimeter suppressed readout.

Each component of the Acquisition system that is connected to the Trigger Framework is called a *Geographic Section*. It captures and processes data in response to L1 Accepts and then conveys the data to the L2 and/or L3 trigger system. For example, L2 central muon crate (L2MUC) captures the data from L1 muon system and processes them to generate L2 central muon decision. L1FW is one of the *Geographic Sections* too. Each *Geographic Section* is connected to the Trigger Framework via a Serial Command Link (SCL). The L1FW supports a total of 128 *Geographic Sections*.

The L1FW is built out of 9U 400mm cards in customized VME crates and make extensive use of FPGA technology. All cards use the same general circuit board and the same front and rear panel layout and connectors. The FPGA programming on this common plate-form produces the different functions needed

throughout the system.The L1FW is programmed and controlled by the Trigger Control Computer (TCC). TCC receives high level programming requests from the global coordinating program (COOR) for the online operation, and performs the low level register programming operations required to implement COOR's requests.

3.7.2 The Level 2 Trigger

The L2 Trigger framework [45] (L2FW) consists of a hardware framework and six preprocessors (also referred as L2 crates. see Fig. 3.16): L2MUC (L2 muon central), L2MUF (L2 muon forward), L2CAL (L2 calorimeter), L2CTT (L2 Central Tracking Trigger), L2PS (L2 Preshower), L2STT (L2 Silicon Tracking Trigger) and L2G (L2 Global). Each preprocessor except L2G captures the data from the corresponding L1 output, and runs more sophisticated algorithms. The di-muon trigger *2MU_A_L2ETAPHI* at L2 requires an event with at least 2 local muon tracks (at least one meeting the medium requirements) with (η,ϕ) separations of at least (3,6) respectively. This triggering is done in L2MUC and L2MUF crates. The preprocessors transmit their results to L2G crate that processes the combined results and make a decision whether the information warrants an accept at L2.

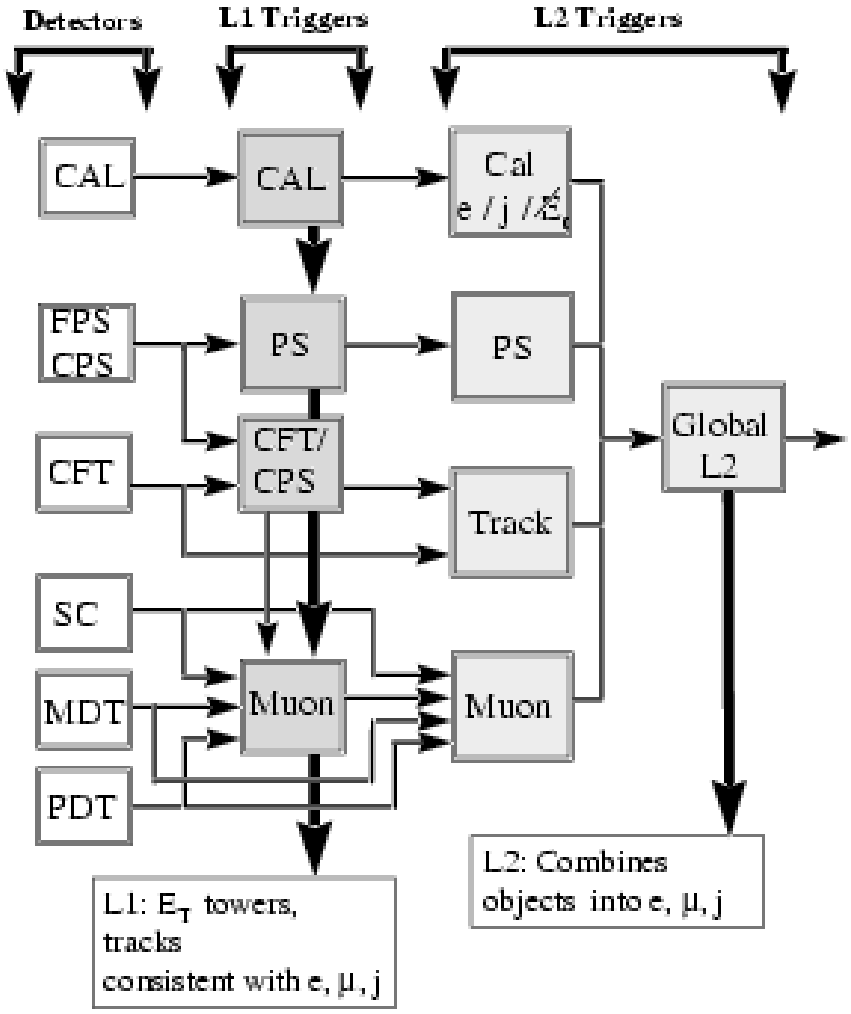

Figure 3.16: L1 and L2 trigger elements. The horizontal arrows denote information flow.

L2 system operates on computers called "β boards", which accept dual Pentium CPUs (up to 1 GHz) with a memory bandwidth limit of about 1 GB/s (64b $\times$ 133 MHz). The time required for each preprocessor to form the associated objects is about 50 μs. For L2G, the time limit is 75 μs. The bandwidth, memory, and CPU have been shown to be sufficient for L2 operations.

Among other L2 monitoring tools, a L2 Bit-Bit comparator framework has been developed. It makes sure that L2 hardware is running properly and L2 online software is consistent with the offline reconstruction software. The comparator is designed to run online so that L2 problems can be found and fixed quickly, saving precious beam time.

3.7.3 The Level 3 Trigger

The L3 trigger system [46] is based on a computer "farm" including over 100 dual 1 GHz Pentium III PCs with 100 mbps Ethernet ports. Such a system presents the advantage of being very flexible in the light of possible future upgrade. Fig. 3.17 shows the architecture of the L3 trigger framework.

A L2 accept triggers full readout of the event to a node of the L3 computer farm. The L3 node performs the following two functions on each event.

1. Event Building: all data received from the detector front-end readout crates and L1, L2 crates are packed into a raw data chunk.

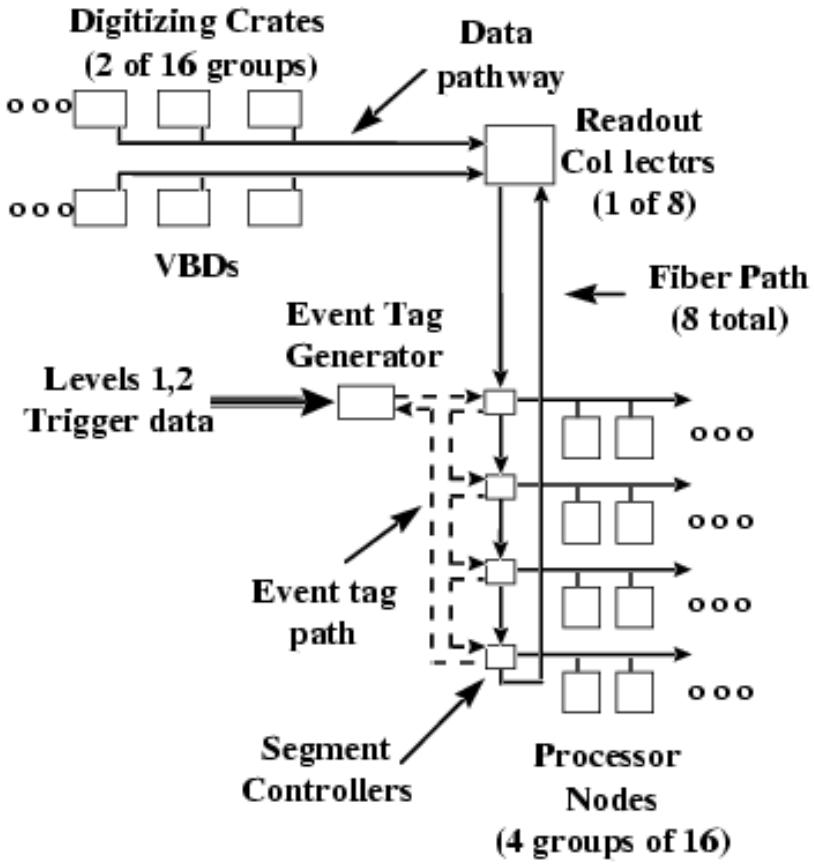

Figure 3.17: L3 architecture.

2. Event Filtering: Guided by L1/L2 trigger information, partially reconstruct the event to determine whether it meets the criteria for acceptance. The event is partially reconstructed to save processing time.

The event building is a very simple process of concatenation of data blocks, and is not expected to consume more than 5 to 10% CPU time on these nodes. Events with over 1000 tracks have been found at high luminosity due to high min-bias events (multiple collision in one beam crossing). Such events can cause a node to use hours of CPU time to process. When more processing power is needed, additional L3 nodes can be added. The natural number of nodes to add is 16, corresponding to one rack.

Each L2 bit that fires causes one or more L3 filter script to be run. If any filter script returns .TRUE. an L3 accept is made. Each filter script consists of the logical .AND. of several filters. Each filter requires the presence of one or more physics objects satisfying given criteria, e.g. two electrons with $E_T > 20$ GeV/c.

Most triggers have a specific Mark and Pass (M&P) rate at L3, where marked events are analyzed as usual, but recorded whether or not they trigger an L3 accept. The events of M&P are used to examine the L3 performance. If the rate is 100 for a given trigger, then one out of each 100 events accepted by that trigger at L2 will be Marked and recorded.

Chapter 4

Offline reconstruction

Once an event passes one or more triggers, it is written to tape for various physics analyses at offline stage. DØ has a farm of 250 Linux computers that run the offline reconstruction framework package (d0reco). The reconstruction includes vertex reconstruction, global track reconstruction, muon reconstruction, electron reconstruction, jet and missing E_T reconstruction, etc. The vertex reconstruction, global track reconstruction, and muon reconstruction are relevant to this analysis and thus discussed in detail next.

4.1 Vertex Reconstruction

It is crucial to reconstruct the primary vertex in every physics analysis. In this analysis, the correctly reconstructed primary vertex means that we can properly exclude the min-bias tracks and use only the tracks from the primary vertex

in the jet charge calculation. In most analysis, having the secondary vertex reconstructed is of significant importance too. In this analysis, the fully reconstructed secondary vertex of the signal side B is required for the time dependent $\sin(2\beta)$ measurement.

The Impact Parameter Algorithm is used to reconstruct the primary vertex. The algorithm starts with an estimated primary vertex position from the fitting of all charged tracks into a single vertex. The candidate tracks must have impact parameter significance (impact parameter divided by its error) less than 3 . With the primary vertex seed, the following steps are run:

1. Fit the vertex and compute $\chi^2(N_{trk})$.

2. Compute the contribution to $\chi^2(N_{trk})$ from each candidate track.

3. Find the track with maximum contribution ($\Delta\chi^2_a$) to $\chi^2(N_{trk})$.

4. Exclude the track from the candidate track list if $\Delta\chi^2_a > \Delta\chi^2_{threshold}$.

5. Repeat step 1 to 4 until no more tracks are excluded. Save the fitted vertex if $N_{trk}) \geq 2$ and $\chi^2(N_{trk}) < \chi^2(N_{max})$.

6. Once a primary vertex has been found, the algorithm is applied again to the remaining tracks and the previous steps are repeated until no more vertices can be reconstructed.

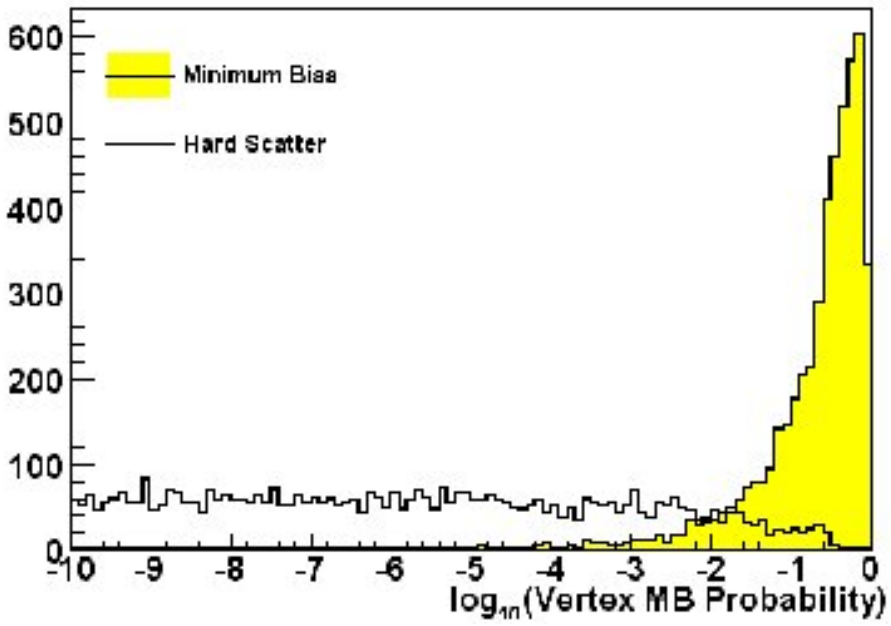

Figure 4.1: Minimum Bias probabilities of the hard scattering event and the minimum bias event

Normally, more than one primary vertex is found, with one being from the hard scattering collision which is of interest to physics analysis. To select the primary vertex associated with the hard scattering collision from the reconstructed primary vertices, the Minimum Bias Probability is computed. The Minimum Bias Probability is obtained from the p_T of the tracks associated to each vertex. The vertex with the lowest probability is selected as the primary vertex, see Fig. 4.1.

It is a little bit more complicated to find the secondary vertices. The following steps show how to reconstruct a secondary vertex:

1. Find track clusters using a simple cone of size 0.5. (*Track clustering*)

(a) removing tracks associated to min-bias vertices.

(b) find highest p_T track as a seed track, requiring $p_T > 2$ GeV/c.

(c) add closest track if $\Delta R < 0.5$. Re-compute the momentum $\mathbf{p}$ of the cluster.

(d) repeat step (c) until no more tracks can be added.

(e) Keep the cluster if total $p_T = \sum p_T > 5$ GeV/c.

(f) repeat step (b) to (e) until no more seed track is available.

2. Select tracks NOT associated to primary vertices (*Track Selection*).

3. Find vertices (*Vertex Finding*).

(a) Force a fit of all tracks in the cluster into a vertex.

(b) Iteratively, reject the track with the highest χ^2 contribution to the vertex until the total χ^2 per degree of freedom becomes smaller than $\chi^2_{threshold}$.

4. Select vertices based on kinematic variables (*Preliminary vertex selection*).

(a) opening angle smaller than 0.1.

(b) require at least 1 track with $p_T > 2$ GeV/c if track multiplicity is greater than 3.

(c) require at least 1 track with $p_T > 1.5$ GeV/c if track multiplicity is greater than 2.

(d) transverse decay length smaller than 2.5 cm (remove lambda's, etc).

(e) longitudinal decay length smaller than 3 cm.

5. Resolve multiple track-vertex associations (*Final vertex selection*).

(a) select and keep the best vertex, i.e. vertex with the smallest χ^2 per degree of freedom.

(b) remove all vertices with at least 1 shared track with the vertex selected

(c) repeat step (a) and (b) until no more vertex remains.

4.2 Global Track Reconstruction

The DØ track-finding algorithm uses the Kalman fitter [47]. The crucial part of the track fitting task is the interacting propagation, which propagates tracks in the DØ tracker including the error, and takes into account magnetic curvature and interaction with detector material. Interactions with detector material cause multiple scattering and energy loss. The DØ interacting propagator includes the most refined knowledge and description of the motion of charged particles in the DØ tracking detectors that is available in a form that is fast enough to use in the reconstruction program.

The Kalman fitter is one way to solve the mathematical problem of determining, from a set of measurements (i.e. the hits in SMT and CFT detectors), the optimal track parameters (see the previous chapter) with errors on any surface. The Kalman fitter can be thought of as an improved procedure of multidimensional χ^2 minimization. The basic Kalman fit algorithm is outlined below

1. make an initial guess of a partially reconstructed track

2. extend the track by the inclusion of additional measurement (i.e. additional hit at additional detector layer)

3. the track parameters and error matrix are propagated (using the interacting propagator) to the surface of the next measurement, creating a prediction on that surface.

4. the prediction and the new measurement are used to produce an improved estimate of the track parameters and errors on the measurement surface.

5. repeat step 1 to 4 until all measurements have been added to the track.

In the central region ($|\eta| < 1.7$), the global track uses the measurements from both SMT and CFT detectors. It has better p_T and impact parameter resolution than using either SMT or CFT hits. In the forward region ($|\eta| \geq 1.7$), the only available measurements are the SMT hits.

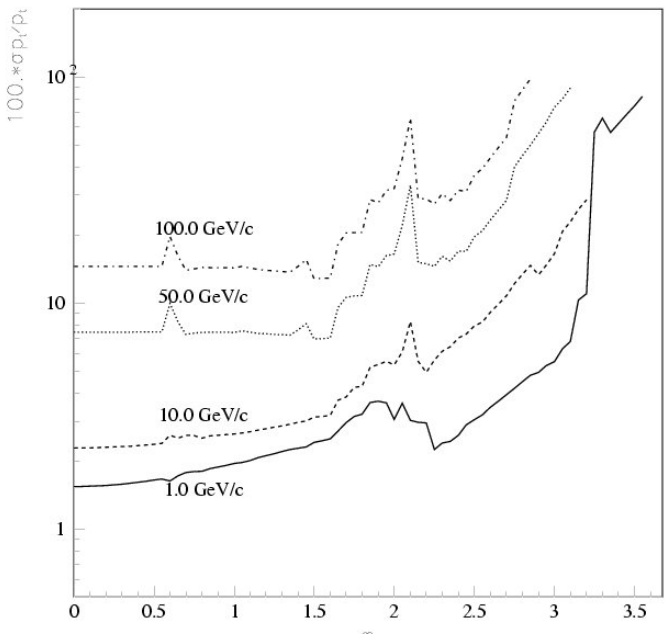

Figure 4.2: The p_T resolutions of the global tracks as a function of pseudorapidity assuming 35 μm vertex resolution.

The p_T resolution of a global track is approximately $\delta p_T/p_T = \sqrt{0.015^2 + (0.0014 * Pt)^2}$ and decreases as the track's pseudorapidity increases. The p_T resolution is summarized in Fig. 4.2. The resolution of the 2-dimensional DCA of a global track is shown in Fig. 4.3. The reconstruction efficiency of the global tracks is shown in Fig. 4.4. More information of global tracks can be found in website of the reconstruction group at DØ [22].

4.3 Muon Reconstruction

Muon objects are first reconstructed in the muon system. The track segments in each muon detector layer are formed by fitting associated muon hits

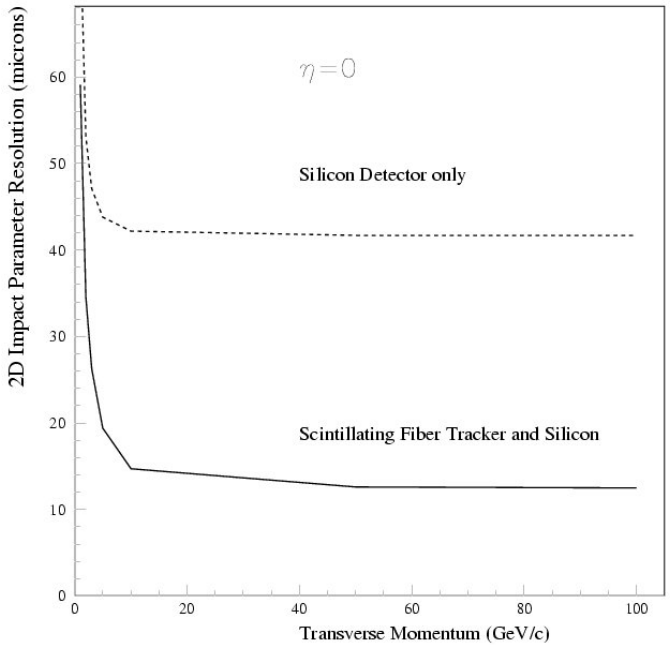

Figure 4.3: Resolution of 2-dimensional DCA for the global tracks at η=0 as a function of transverse momentum.

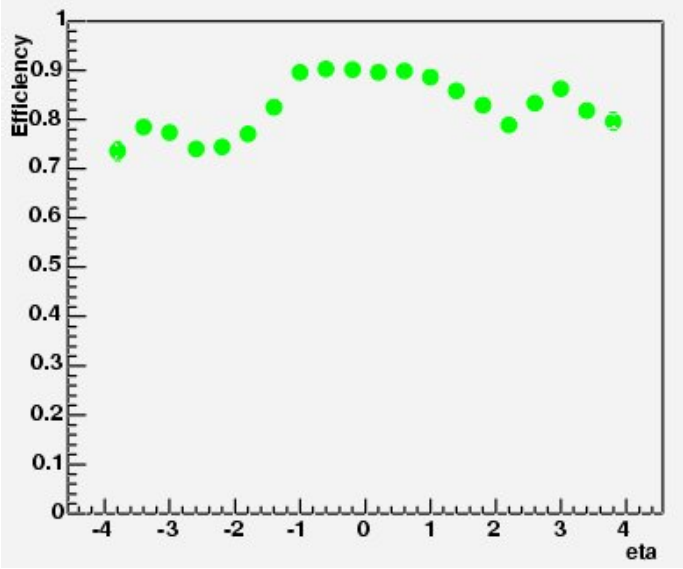

Figure 4.4: The reconstruction efficiency of the tracks on $Z \rightarrow \mu\mu$ events.

into a straight line. The track segments are then matched and the local muon momentum is computed from the measurement of the bend of a track passing through the muon toroid magnet. As we have discussed in the last chapter, local muon momentum resolution is much poorer than that of global tracks. Therefore the kinematic variables of a muon track are drawn from a matched global track.

Chapter 5

Opposite Side Jet Charge Tagging

5.1 Introduction

The identification of the production flavor of reconstructed neutral B-hadrons is required for both B mixing and CP asymmetry studies. The B-hadrons are either fully or partially reconstructed in specific decay channels, e.g. $B \to J/\psi K_s$, and are referred to as the signal B-hadrons in the context of the jet charge tagging analysis.

Flavor tagging refers to determining if the signal B is a B (containing a $\bar{b}$ quark), or a $\bar{B}$ (containing a b quark). There are three tagging algorithms at DØ : Opposite Side Soft Lepton Tagging (SLT) [49], Opposite Side Jet Charge Tagging (JETQ), and Same Side Tagging (SST) [50]. The SST algorithm utilizes the correlations between the signal side b-quark flavor and the charges of the associated particles from its hadronization process. For example, as shown in

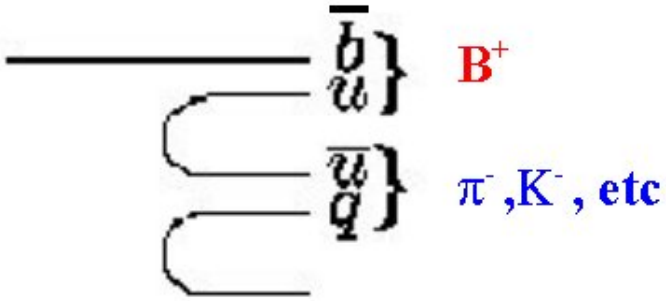

Figure 5.1: The charge correlation used in the SST tagging algorithm.

Fig. 5.1, the signal B is a B^+, the "first" associated particles produced in the hadronization process is π^-, or K^-, etc, and this particle generally has a higher p_T than other particles of the fragmentation remnants.

Opposite side tagging refers to tagging the flavor of the signal B by determining the flavor of the "opposite" side B. Since the strong interaction production of b quarks occurs in $b\bar{b}$ pairs, the signal side b-flavor is revealed once the opposite side b-flavor is tagged. The SLT algorithm uses those events where the opposite side B decays semileptonically, utilizing the correlations between the charge of the lepton (e or μ) in the transition decay of $b \rightarrow c$ and the b-flavor. For a b-quark, the lepton has a negative charge; for a $\bar{b}$-quark, the lepton has a positive charge.

The JETQ algorithm utilizes the correlations between the charge of the opposite side b-quark and the average charge of its daughter particles (jet charge). For a b-quark, the associated jet charge is more likely to be negative; for a $\bar{b}$-quark, the associated jet charge is more likely to be positive.

To test the performance of the tagging algorithm in real data, we use data samples consisting of $B^{\pm} \rightarrow J/\psi K^{\pm}$ decays. In such samples the flavor of the signal B is already revealed by the sign of the kaon's charge. The B_d mixing measurement using the JETQ algorithm provides another way to test the tagging performance.

5.2 The Tagging Efficiency, Dilution, and Tagging Power

The tagging efficiency (ϵ) and dilution (D) are used to evaluate the performance of the tagging algorithm. They are defined as follows

$$\epsilon = \frac{N_T}{N} \tag{5.1}$$

$$D = \frac{N_R - N_W}{N_T} \tag{5.2}$$

The variables in the above equations are

- N: The total number of input events to be tagged.
- N_T: The total number of tagged events
- N_U: The total number of un-tagged events
- N_R: The total number of correctly tagged events

- N_W: The total number of incorrectly tagged events

where $N = N_T + N_U$, $N_T = N_R + N_W$.

The tagging efficiency is simply the probability that the tagging algorithm gives a tag. The tagging dilution is related to the probability that the tagging algorithm tags an event correctly/incorrectly as shown below

$$P_{rtag} = \frac{1}{2}(1 + D) \tag{5.3}$$

$$P_{wtag} = \frac{1}{2}(1 - D) \tag{5.4}$$

where $P_{rtag}(P_{wtag})$ is the probability that the tag is correct (incorrect). The reason that one uses the dilution instead of P_{rtag} becomes clear when one examines the statistical power.

Consider an asymmetry measurement of a sample with N events, if the number of the reconstructed B ($\bar{B}$) events is N_B ($N_{\bar{B}}$), the asymmetry, referred to as the raw asymmetry, of this sample between B and $\bar{B}$ is defined as

$$A = \frac{N_{\bar{B}} - N_B}{N_{\bar{B}} + N_B} \tag{5.5}$$

Assuming the same tagging efficiency and dilution for both types of events, the number of events tagged as B ($\bar{B}$) is the sum of the number of B ($\bar{B}$) events tagged correctly and the number of $\bar{B}$ (B) events tagged incorrectly as given below

$$N_B^{tag} = N_B \epsilon \frac{1 + D}{2} + N_{\bar{B}} \epsilon \frac{1 - D}{2} \tag{5.6}$$

$$N_{\bar{B}}^{tag} = N_{\bar{B}}\epsilon\frac{1+D}{2} + N_B\epsilon\frac{1-D}{2} \tag{5.7}$$

The asymmetry in the tagged sample will be

$$A_{tag} = \frac{N_{\bar{B}}^{tag} - N_B^{tag}}{N_{\bar{B}}^{tag} + N_B^{tag}} = D * A \tag{5.8}$$

Compare with the raw asymmetry, the tagged asymmetry is diluted by the quantity of dilution. The statistical uncertainty of A is

$$\sigma_A = \sqrt{\frac{1 - D^2A}{\epsilon D^2 N}} \tag{5.9}$$

The uncertainty scales like $1/\sqrt{\epsilon D^2 N}$, rather than the more familiar $1/\sqrt{N}$. This means that the statistical power of the tagging algorithm is quantified by ϵD^2, referred as the tagging power. To minimize the statistical error, one should maximized the quantity ϵD^2.

5.3 The Jet Charge

The jet charge flavor tagging algorithm was first developed in e^+e^- collider experiments [51][52]. In the e^+e^- collider environment, the jet charge is defined as the momentum weighted average charge of tracks associated to a jet

$$Q_{jet}^{e^+e^-} = \frac{\sum_i^n q_i(P_i \cdot \hat{a})}{\sum_i^n (P_i \cdot \hat{a})} \tag{5.10}$$

where q is the charge, P is the total momentum vector, and $\hat{a}$ is the unit vector along the jet direction. However, this formula does not work for the JETQ

tagging at hadron-hadron colliders. This is because the hadron collider environment is much more complex than the e^+e^- collider environment. First, in the B samples from hadron-hadron colliders, the opposite side B may have only part of its daughter particles reconstructed due to the detector acceptance limitation (such events can be easily identified by monitoring the jet structure in e^+e^- experiments). This makes the direction of a reconstructed B jet not necessarily the direction of the associated B. Secondly, the composite nature of the two incoming beam particles implies the additional possibility that several parton pairs undergo separate hard or semi-hard scatterings, referred to as the "underlying events". The underlying event is everything from the primary vertex except the two outgoing b "jets". These underlying events produce a number of gluon and light quark emissions, introducing a number of parton jets in addition to the two B jets. If the B has a small energy, it is very difficult to separate the B jet from a parton jet. Selecting the wrong jet in the jet charge tagging causes Eq. 5.10 to fail. On the contrary, the $b\bar{b}$ events produced at e^+e^- colliders have a clean two- or three-jet (caused by the gluon emission from one b quark) structure, making it much easier to determine the direction of the B.

We define the jet charge in this analysis by Eq. 5.11. It is based on the fact that the daughter particles from B-hadrons have, on average, the highest transverse momentum (p_T) among all particles in the event. We found the tagging power varies slightly when n is varied around 1. For bigger or smaller n, the

tagging power decreases. Therefore we have chosen $n = 1$.

$$Q_{jet} = \frac{\sum P_T^n(i) * q(i)}{\sum P_T^n(i)} \tag{5.11}$$

We have investigated other possible correlations that may be utilized, but finding none of them improve the tagging power. For example, we tried utilizing the Distance Closest Approach (DCA) to the primary vertex as a weight (giving a larger weight to tracks having DCA above a threshold), the results showed that it did not help the tagging due to the poor DCA resolutions and the fact that many B daughters just have very small DCA (B decays exponentially when moving away from the primary vertex). We have also tried using the cosine of the angle between a track and the jet direction as a weight (giving bigger weight to small angle, since the B daughter particles are assumed closer to the B direction). But it did not help either because the problem in obtaining the correct B direction. Moreover, this weight may give bigger weight to particles that are not from the opposite side B, but happen to be closely aligned to the B direction.

Figure 5.2 shows a plot of the calculated jet charges for a MC B^- sample using Eq. 5.11. We have used all candidate particles in an event to calculate the jet charge, instead of using the jet cone algorithm [56] [57] or K_T jet algorithms [54] [55]. The detail of the candidate particles and jet algorithms will be discussed later in this chapter. A requirement of $|Q| > 0.2$ is imposed on the tagging results. If $|Q| < 0.2$, the event is labeled as un-tagged. This requirement is chosen by

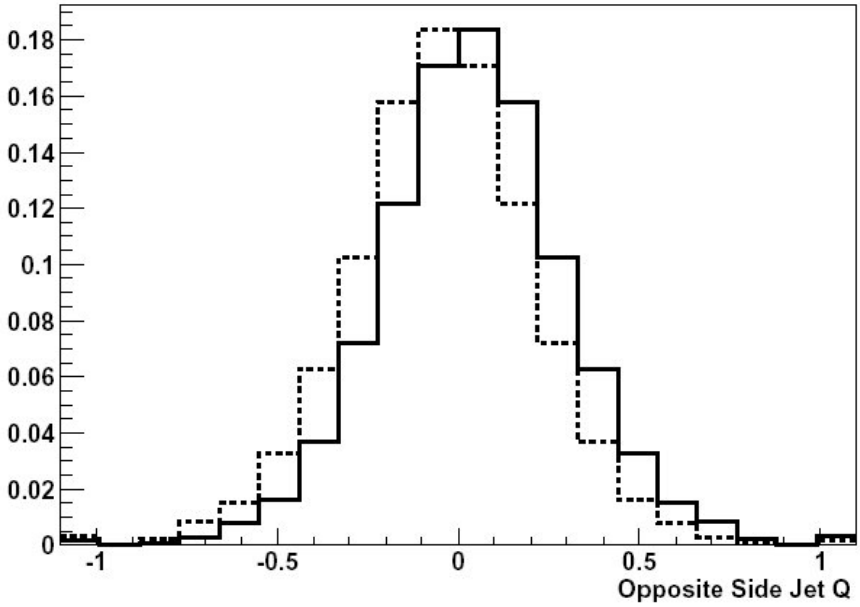

Figure 5.2: Plot of the jet charges tagged by the JETQ algorithm for a B^- sample. The solid line is for the calculated jet charges. The dotted line is a "flip" of the the solid line, helping to see the separation power of the tagging algorithm.

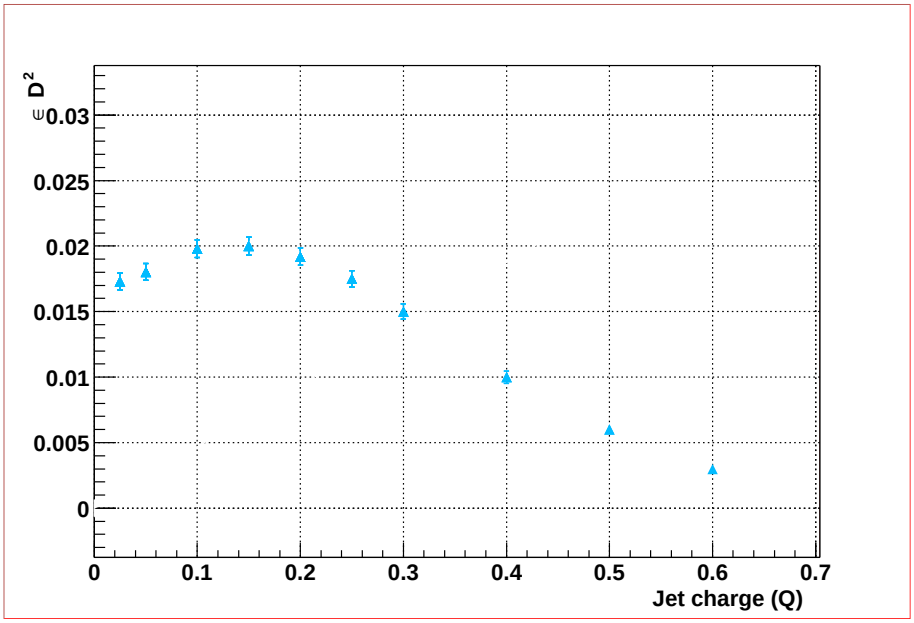

Figure 5.3: The tagging power with different Q cuts.

optimizing both the tagging power and tagging dilution. Figure 5.3 and 5.4 show the tagging power and dilution change as a function of the cut on Q for a typical B^- sample. The $\bar{B}^0$ MC samples yield similar plots.

5.4 The Classification of Particles

To better understand how the different classes of particles affect the jet charge calculation, we categorize the particles into the following classes (See Fig. 5.5)

1. "FB daughters": particles from the signal side B-hadron.

2. "OB daughters": particles from the opposite side B-hadron.

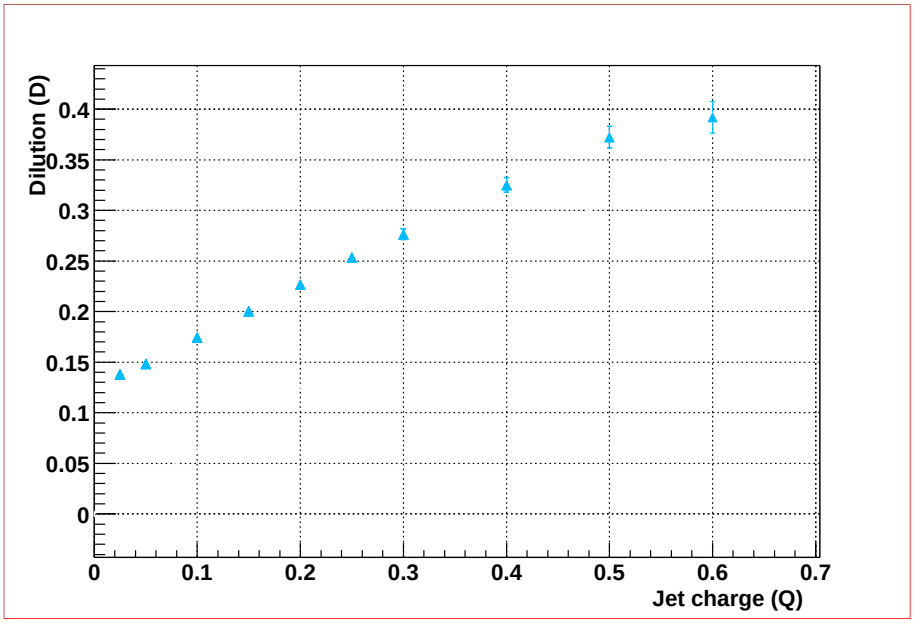

Figure 5.4: The tagging dilution with different Q cuts.

3. "Fb daughters": particles from the signal side b-quark, excluding daughters from the signal B-hadron.

4. "Ob daughters": particles from the opposite side b-quark, excluding daughters from the opposite side B-hadron.

5. "Undl. Particles": particles from the underlying events.

6. "Minbias particles": particles from the minbias events. In high-luminosity collisions, it is possible to have several collisions in a given beam crossing. In a $b\bar{b}$ event, as one collision gives the $b\bar{b}$ pair, the other are generally QCD events. These minbias events build up the total production of particles that is observed by detectors.

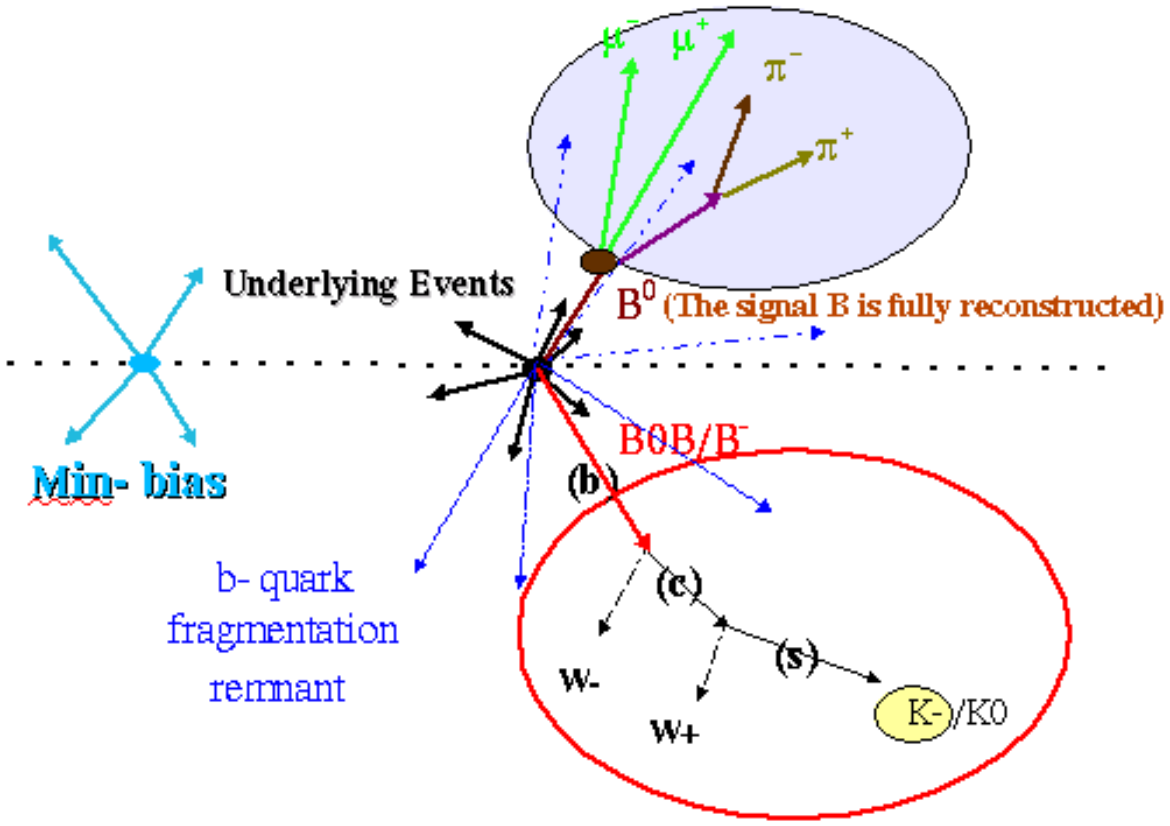

Figure 5.5: A $b\bar{b}$ event at Tevatron Collider

The "FB daughters" are explicitly excluded in the jet charge tagging. The "Fb daughters" play a very special role: causing an apparent asymmetry in the tagging power between charged and neutral B samples. We postpone the discussion on this until the next section.

The "OB daughters" play the most important role in the jet charge tagging. If we only use the "OB daughters" to calculate the jet charge, the tagging power, ϵD^2 is 7.7% for both charged and neutral B samples (there is no asymmetry in the tagging power between the two type samples, since "Fb daughters" are not included). More specifically, it is the charged kaon (also the lepton) from the opposite side B that plays the most important role in the JETQ tagging. The kaon is mainly from the decay chain: $b \to c \to s$. The charged kaon has a strong charge correlation to the flavor of the opposite side B.

The important role played by the kaon becomes clear when one divides the B^- sample into three sub-samples (separating the opposite side B to be B^+, B_d^0 and B_s^0 for each sub-sample) and examines the fraction of events having a charged kaon in each sub-sample and the corresponding tagging power. Table 5.1 shows the fraction of events that on average have one $K^+/K^-/\pi^+/\pi^-$ for each sub-sample. There is an excess of K^+ in the first two sub-samples, with the B^+ sub-sample having the largest excess. The excess of K^+ makes it more likely to tag the B flavor correctly, noting that a positive jet charge corresponds to a correct tag in this example. If we only use the "OB daughters" to calculate the

Opp. side B type	K^+ fraction	K^- fraction	π^+ fraction	π^- fraction
B^+	$44.0\% \pm 0.19\%$	$9.2\% \pm 0.11\%$	$85.1\% \pm 0.14\%$	$67.4\% \pm 0.18\%$
$B_d^0(mixing\ off)$	$33.8\% \pm 0.18\%$	$13.9\% \pm 0.13\%$	$69.5\% \pm 0.18\%$	$79.8\% \pm 0.15\%$
$B_s^0(mixing\ on)$	$27.2\% \pm 0.31\%$	$27.1\% \pm 0.31\%$	$66.6\% \pm 0.33\%$	$66.6\% \pm 0.33\%$

Table 5.1: The fraction of all events that have one of the specified particles on average. Each row corresponds to different types of sub-samples

jet charge, the tagging power is as high as $22.0\% \pm 0.3\%$ for the B^+ sub-sample! For the B^0 sub-sample (B_d^0 mixing is turned off in the MC), the tagging power is only $3.68\% \pm 0.1\%$, due to the smaller excess of K^+ and the 10% excess of π^-. For the B_s sub-sample (B_s^0 mixing is on), there is no excess observed for either kaons or pions because of the fast mixing rate of B_s^0, making the tagging power vanish.

Although charged kaons are very important in tagging, DØ does not have the ability to identify kaons. In the JETQ tagging algorithm, we use all candidate tracks passing a number of selection requirements (discussed next) to calculate the jet charge.

The "Ob daughters" make different contributions based on the different sub-samples mentioned above. For the B^+ sub-sample, the inclusion of the "Ob daughters" makes the tagging power drop to $5.8\% \pm 0.2\%$ because they carry net charges ($-\frac{2}{3}$), opposite to the correct jet charge; for the B^0 and B_s^0 sub-samples, the tagging power increases to $5.3\% \pm 0.2\%$ and $1.2\% \pm 0.1\%$ respectively, since

the "Ob daughters" carry net charges ($+\frac{1}{3}$) in favor of making correct tags. The overall effect of the "Ob daughters" on the complete sample makes the tagging power drop from $7.7\% \pm 0.1\%$ to $4.9\% \pm 0.1\%$.

The "Undl. Particles" and "Minbias particles" are softer in p_T than the "OB daughters", however their multiplicities are much larger. The underlying event is an unavoidable background to many collider observables. The "Minbias particles" can be suppressed by requiring that a particle come from the primary vertex. However this can not remove all the "Minbias particles", since some "Minbias particles" may be from a vertex that is very close to the primary vertex. The inclusion of the "Undl. Particles" and "Minbias particles" causes the tagging power to drop significantly. In the above example, the tagging power drops from $4.9\% \pm 0.1\%$ to $1.3\% \pm 0.1\%$.

5.5 The Requirement of the $\Delta\phi/\Delta R$ Separation

We have found that the "Fb daughters" produce a significantly larger tagging power in the charged B samples than in the neutral B samples. This is explained by the fact that the "Fb daughters" carry opposite net charges between the two samples. Taking B^- and $\bar{B}^0$ samples as an example (both Bs fragment from a b-quark), the "Fb daughters" carry net **positive** charge ($+\frac{2}{3}$) in the B^- sample, but net **negative** charge ($-\frac{1}{3}$) in the $\bar{B}^0$ sample. Since the positive jet charge

corresponds to a correct tag in this example, the inclusion of the "Fb daughters" causes an event being more likely to be tagged correctly for the B^- sample, and reduces the possibility of making a correct tag for the $\bar{B}^0$ sample.

In order to suppress the effects from the "Fb daughters", we impose one of the two following requirements

1. $\Delta\phi$ separation: particles are required to have a minimum separation $\Delta\phi$ in ϕ space relative to the direction of the signal B.

2. ΔR separation: particles are required to have a minimum separation ΔR $(= \sqrt{\Delta\eta^2 + \Delta\phi^2})$ in $\eta - \phi$ space relative to the direction of the signal B.

The tagging algorithm used in CDF during Run I [53], required a ΔR separation greater than 0.7 to suppress the effect from the "Fb daughters". However, we found this to be too small, causing the tagging power of charged B sample to be much larger than that of neutral B sample (three times bigger in our MC samples). Figure 5.6 shows the $\Delta\phi$ and ΔR distributions of a typical $b\bar{b}$ sample. Most of "Fb daughters" survive the $\Delta R > 0.7$ cut.

Table 5.2 shows a comparison of the tagging power between the two requirements for neutral B samples. The $\Delta\phi$ requirement yields a larger tagging power than the ΔR requirement. Since the tagging power of neutral B samples are what we need to maximize, we have chosen the $\Delta\phi$ requirement in our final analysis.

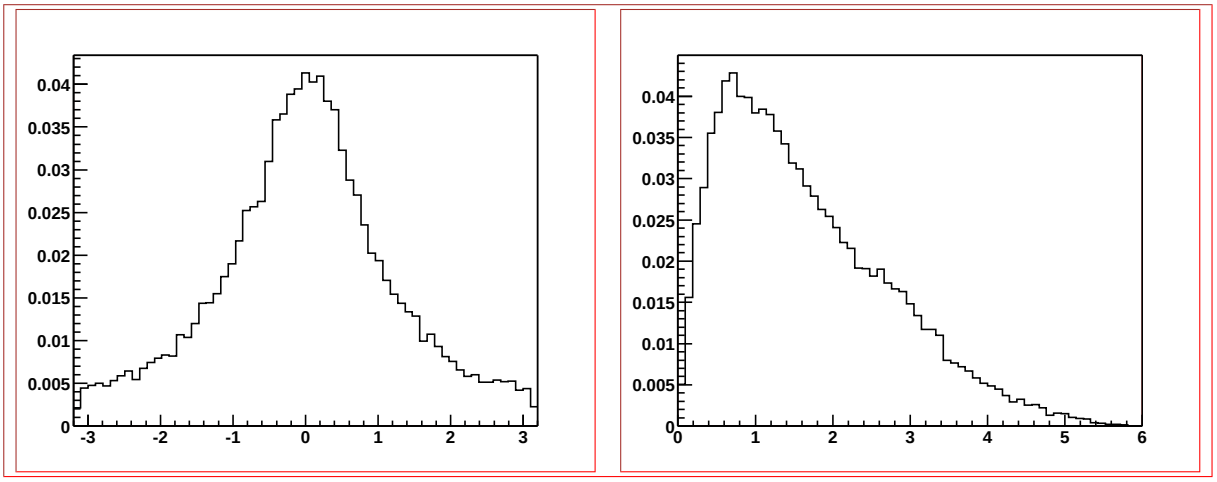

Figure 5.6: The left plot shows the $\Delta\phi$ distribution of the "Fb daughters" relative to the direction of the signal B. The right plot shows the ΔR distribution of the "Fb daughters" relative to the direction of the signal B.

Separation	Dilution with $\Delta\phi$ cut	Dilution with ΔR cut
0.7	0.78% ± 0.04%	0.57% ± 0.04%
1.5	0.97% ± 0.05%	0.91% ± 0.05%
2.0	1.02% ± 0.05%	0.93% ± 0.05%

Table 5.2: Comparison between the tagging power by using the requirement of $\Delta\phi$ and the requirement of ΔR.

5.6 The Jet Algorithms

To make jets, a list of candidate tracks are selected from the particles that pass the following selection criteria

1. The "FB daughters" are explicitly excluded.

2. A track must have the z vertex displacement from the primary vertex less than 2.0 cm. This is to suppress the tracks from the minbias events.

3. A $\Delta\phi$ requirement on the separation of a track from the direction of the signal B. This requirement has two functions: 1) suppress the contribution from the "Fb daughters", 2) suppress the contribution from the "Undl. Particles" as well as the "Minbias particles".

In the next two sections, we describe the jet cone algorithm and the K_T jet algorithm and their applicabilities in this analysis. In the last section, we make the conclusion that the jet charge should be computed by using all the candidate tracks, instead of using a jet from any jet algorithm.

5.6.1 The Jet Cone Algorithm

Jets of narrowly collimated energetic hadrons are observed in $p\bar{p}$ collision (Fermilab, CERN), ep scattering (HERA) and in e^+e^- annihilations[58] (SLAC,

LEP, DESY, KEK). The jet cone algorithm is commonly used to reconstruct jets. The details of the algorithm at DØ can be found in Ref. [59].

Instead of using the calorimeter objects, we use the reconstructed global tracks to make jets, since most B daughters do not make corresponding calorimeter objects. We have found the jet cone algorithm works poorly in our analysis environment. This is because the average E_T of the B jets is much lower than the E_T of the jets commonly used in the jet cone algorithm. The B jet is composed, instead of narrowly collimated energetic hadrons, low p_T hadrons that have a large spread in $\eta - \phi$. For a typical $b\bar{b}$ sample, the average p_T of the "OB daughters" is about 2 GeV. Fig. 5.7 shows the ΔR separation of the "OB daughters" from the associate b's direction when the signal side B has p_T from 3 to 6 GeV and from 15 to 18 GeV. When the B p_T is above 15 GeV, a cone of size $\Delta R = 0.7$ (commonly used in the jet cone algorithm) contains most of the daughter particles. However this cone size becomes too small, when the p_T is smaller. Moreover, the "OB daughters" have a very low multiplicity. With the requirement of $p_T > 0.5$ GeV, the multiplicity of the opposite side B decay products is only about 2, while the total multiplicity of the produced particles is about 20. Overlapping jets cause another problem for the jet cone algorithm. If a track is contained in two jet cones, one has to develop a way to assign the track in a specific jet. Such assignments may not be correct in all cases.

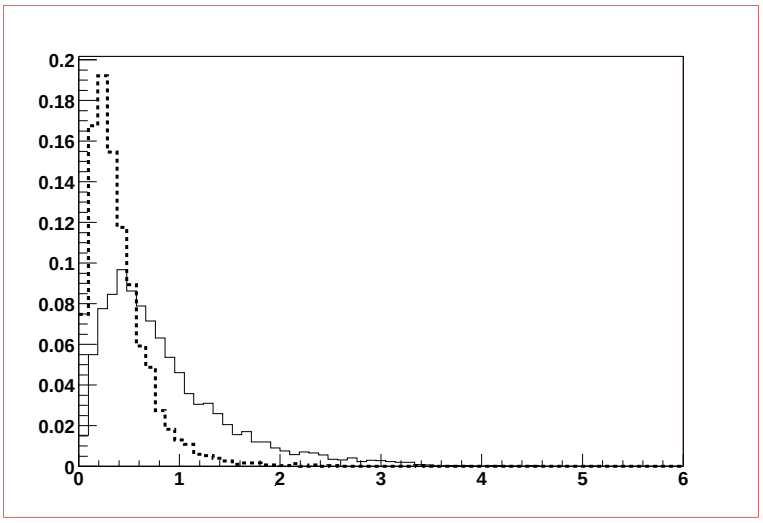

Figure 5.7: The ΔR separation of the "OB daughters" from the associated b quark direction. The solid line is for the case when the p_T of the signal side b-quark is from 3 to 6 GeV. The dotted line is for the case when the p_T of the signal side b-quark is from 15 to 18 GeV.

In summary, the large jet width, low multiplicity and low p_T make the construction and selection of the B jets very difficult using a fixed cone size jet algorithm in the hadron-hadron collider environment.

5.6.2 The K_T jet algorithm

The K_T jet algorithm successively merges pairs of tracks in order of increasing relative transverse momentum. The algorithm contains a single parameter, D, that controls when the merging stops. Every particle in the event is uniquely assigned to a jet and there are no overlapping jets as there is in the cone algorithm.

The K_T algorithm is described as follows

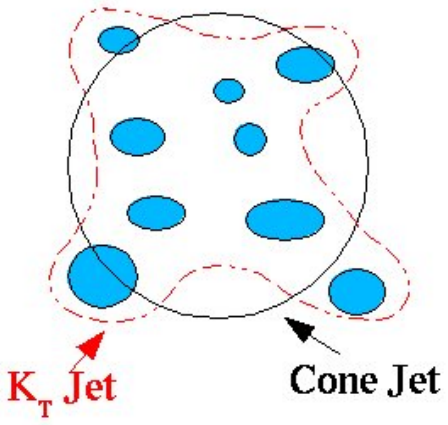

Figure 5.8: The comparison on the shape of jet between the jet cone algorithm and the K_T jet algorithms.

1. For each pair of tracks, i and j, define:

$$d_{ij} = min(p_T^2(i), p_T^2(j))\frac{\Delta R_{ij}^2}{D^2} \tag{5.12}$$

where ΔR_{ij}^2 is the separation of the i^{th} and j^{th} track in $\eta - \phi$ space

$$\Delta R_{ij} = \sqrt{(\eta_i - \eta_j)^2 + (\phi_i - \phi_j)^2} \tag{5.13}$$

Also define

$$d_i = p_T^2(i) \tag{5.14}$$

2. Find the minimum d_{min} of all d_i and d_{ij}.

3. If d_{min} is a d_{ij} then the two tracks are merged, using the 4-vector recombination scheme, into a new "track" k with

$$P_k = P_i + P_j \quad \eta_k = -ln(tan\frac{\theta_k}{2}) \quad \phi_k = tan^{-1}(\frac{P_y^k}{P_x^k}) \tag{5.15}$$

4. If d_{min} is a d_i, then the i^{th} track is not "mergable" and is removed from the track list pool and added to the jet list.

5. Repeat steps 1 - 5 until all the tracks have been merged into jets.

Many studies of the jet cross sections at DØ [60] have shown the difference between K_T and jet cone algorithm is actually very small. However, compared with the cone algorithm (see Fig. 5.8), the K_T algorithm indeed gives a better shape of jet – a more natural shape. We found this advantage helps the K_T algorithm perform better by reducing the loss of the "OB daughters". However, the algorithm still suffers the problem that the B jet is soft and has low multiplicity.

5.6.3 Use all candidate particles

Besides the two jet algorithms discussed above, there is another option to compute the jet charge: using all of the candidate tracks. The advantage of this algorithm is that it eliminates the chance that the "OB daughters" are all discarded when a "wrong" jet is selected. It may also recover some of the "OB daughters" if they are not included in a selected B jet.

We have compared the tagging results of using all candidate tracks with those of the K_T algorithm. For the MC B^- sample, the tagging power of the K_T algorithm is only $0.81\% \pm 0.04\%$, while the tagging power of using all candidate tracks is $1.92\% \pm 0.07\%$. For the MC $\bar{B}^0$ sample, the tagging power of the K_T

algorithm is only $0.66\% \pm 0.04\%$, while the tagging power for using all candidate tracks is $1.02\% \pm 0.05\%$. Therefore, we use all the candidate tracks to compute the jet charge in our final analysis.

Chapter 6

Monte Carlo Samples

6.1 Monte Carlo Event Simulation

Monte Carlo (MC) Event Simulations have become routine in high energy physics as well as looking at real data. Monte Carlo techniques generate complete events with all particles from the parton level to the final state stable particles, giving a complete simulation of the events produced in colliders.

The generated events are processed through a detector simulation software package (called *d0sim* at DØ) to include detector effects (e.g particles interact with detectors, making signals in each detector cell), and the reconstruction software package (called *d0reco* at DØ) to include the performance of the event reconstruction (such as tracking efficiency, p_T resolution, etc). In cross section measurements, generated events are also processed by the trigger simulation package (called *d0trigsim* at DØ) to study trigger efficiencies for various physics

processes.

Monte Carlo techniques have been shown to be very successful in high energy physics. However, one must be aware of all liabilities of the Monte Carlo simulations. In some processes, MC simulations are far from complete, making potentially large differences between MC and experimental results.

6.2 The Production Mechanism of $b\bar{b}$ pairs

There are three major sub-processes that contribute to the generation of $b\bar{b}$ events at the Tevatron, see Fig. 6.1.

1. Flavor Creation (FC): A pair of $b\bar{b}$ quarks is created by annihilation of light quarks or by gluon fusion via the two 2-to-2 parton subprocesses, $q+q \rightarrow b\bar{b}$, and $g + g \rightarrow b\bar{b}$.

2. Flavor Excitation (FE): Although there are no valence b quarks in the proton, at high Q^2 $b\bar{b}$ pairs are produced by gluons and populate the proton sea. In the flavor excitation process, one of these b-quark is knocked out of the initial state into the final state by a parton via the subprocesses $g + b \rightarrow g + b$, $g + \bar{b} \rightarrow g + \bar{b}$, $q + b \rightarrow q + b$, $q + \bar{b} \rightarrow q + \bar{b}$, etc.

3. Gluon Splitting (GS): In the gluon splitting events, only gluons and light quarks and light antiquarks participate in the 2-to-2 hard parton scattering

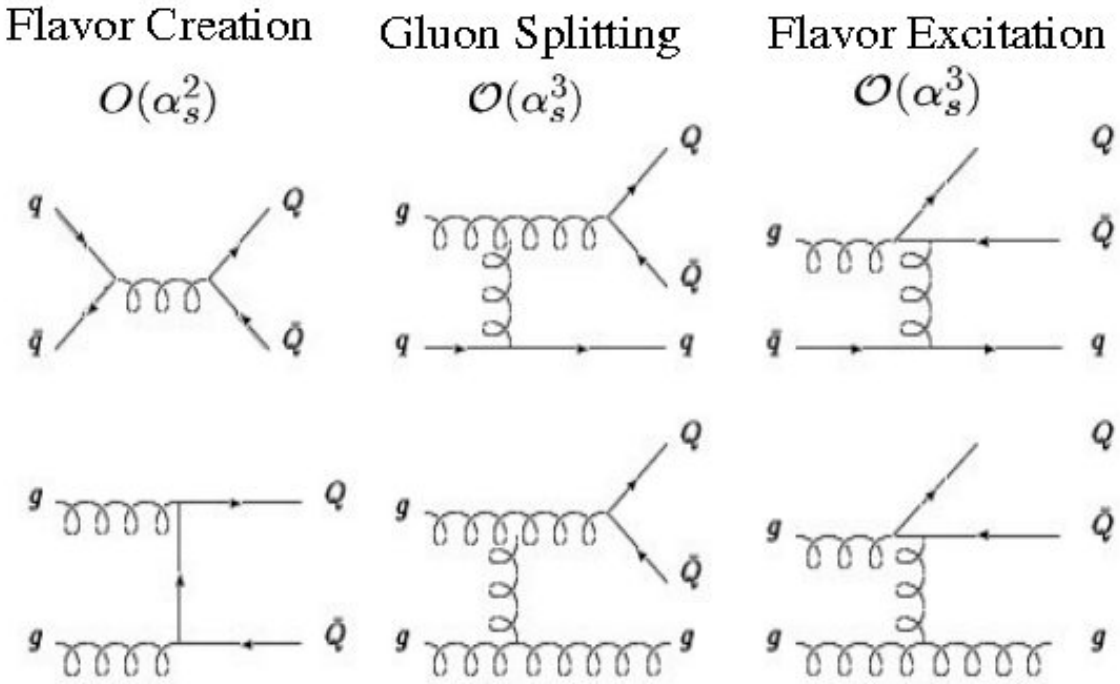

Figure 6.1: Feynman Diagrams for LO and NLO $b\bar{b}$ pair production.

subprocess. The $b\bar{b}$ pairs originate in the shower or fragmentation of the outgoing energetic gluons, light quarks and light antiquarks. Such subprocess include $g + g \rightarrow g + (g \rightarrow b\bar{b})$, $q + q \rightarrow q + (q \rightarrow b\bar{b}q)$, etc.

We have found there are three major differences in the topologies and kinematics among the three subprocesses: 1) they have distinct distributions of the azimuthal separation between the $b\bar{b}$ pairs; 2) they have distinct distributions of the p_T correlations between the $b\bar{b}$ pairs; 3) they have different p_T distributions of b-quark. These differences are discussed in detail below.

The azimuthal separation

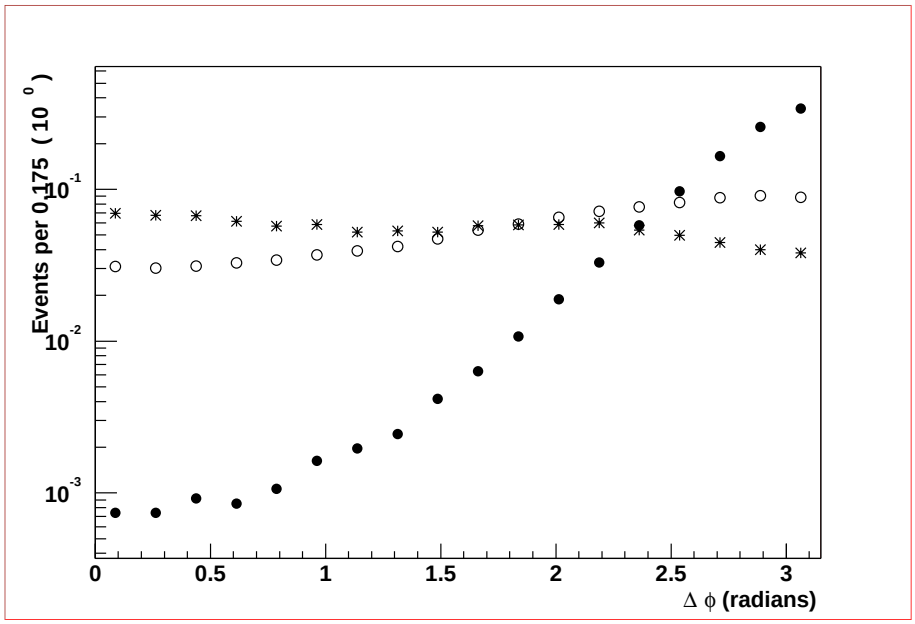

Figure 6.2: The azimuthal separation of the $b\bar{b}$ events from the Flavor Creation (solid dots), Flavor Excitation (circles) and Gluon Splitting ($*$ dots) subprocesses.

Figure 6.2 illustrates the azimuthal separation for each subprocess. The accepted events correspond to the events passing the selection criteria which will be discussed later in this chapter. The difference between the flavor creation and the other two subprocesses is significant, while the difference between the flavor excitation and the gluon splitting subprocesses is much smaller. These distinct topologies make the JETQ algorithm perform much better (i.e. having larger tagging power) for the flavor creation subprocess than the other two subprocesses. The tagging powers of the flavor excitation and the gluon splitting subprocesses are similar.

The p_T correlations

Figure 6.3 illustrates the p_T correlation between the two b-quarks for each subprocess. The accepted events correspond to the events after the event selection. From the figure, one can see that the flavor creation subprocess has strong p_T correlations, while the other two subprocesses do not show correlation.

The p_T distribution of b-quark

Fig. 6.4 illustrates the p_T distribution of b-quark. Again, the accepted events correspond to the events after event selection. In the low p_T region, the flavor creation subprocess has a higher fraction in the total sample; in the high p_T region, the other two subprocesses have higher fraction.

6.2.1 Event generation

We have used PYTHIA version 6.202 in the DØ software framework to generate the MC $b\bar{b}$ event samples. The flavor creation events are the easiest to generate. One can either run the heavy quark option (i.e. $MSEL = 5$ in the PYTHIA generator card) or run all QCD ($MSEL = 1$) and then select the flavor creation events by monitoring the 2-to-2 subprocesses. If one runs all QCD in PYTHIA, the b-quark mass is set to zero. Therefore, one should generate the flavor creation subprocess by running the heavy quark option in PYTHIA.

The flavor excitation and gluon splitting events can only be generated in PYTHIA by running all QCD and select the events by monitoring the 2-to-2

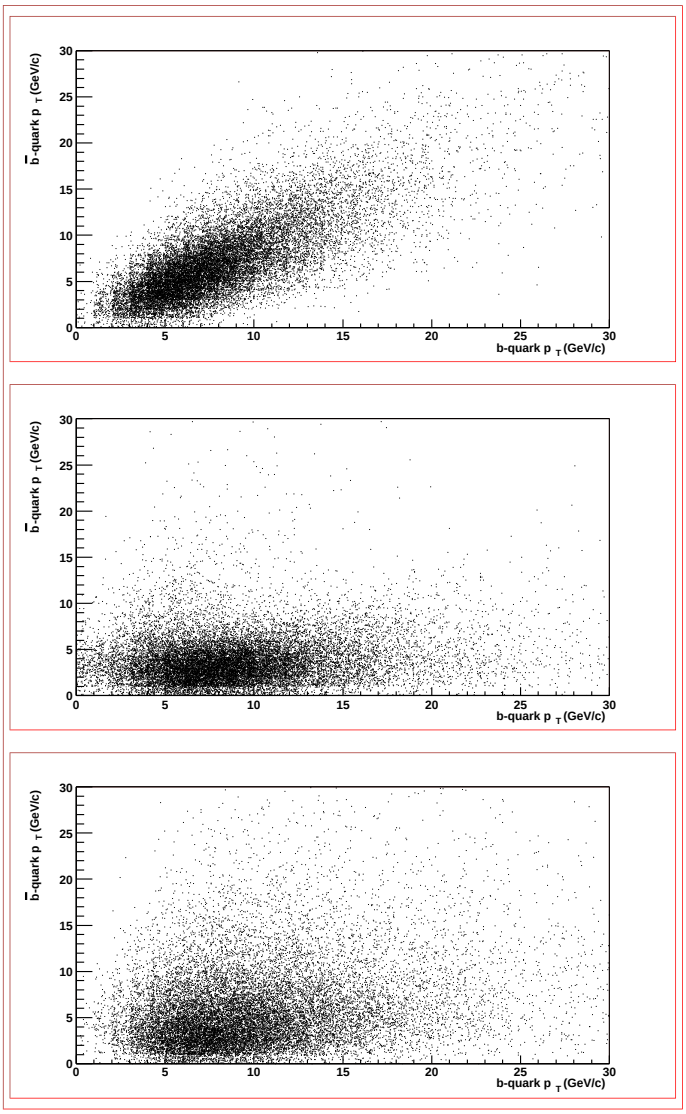

Figure 6.3: The p_T correlation between the two b quarks for the Flavor Creation events (top), Flavor Excitation events (middle) and Gluon Splitting events (bottom). Events correspond to the events after event selection.

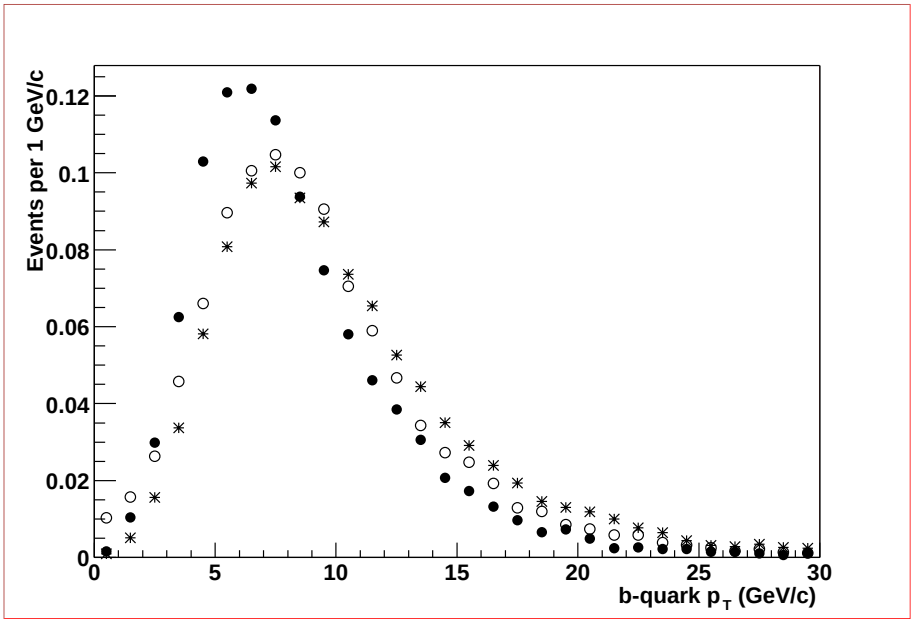

Figure 6.4: The p_T distribution of b-quark after event selection.

subprocess. This process has a very low efficiency in the generation of $b\bar{b}$ events. We found the efficiency is increased largely by increasing the $ckin(3)$ parameter (the parameter in PYTHIA that controls the minimum p_T value allowed in hard 2-to-2 process) in the PYTHIA card file. By varying $ckin(3)$ from 0 to 5, we found the kinematics of the b-quark is almost same. We have chosen $ckin(3) = 5$ to generate the MC samples of the flavor excitation and gluon splitting events. The corresponding efficiency is 1.2%.

For the generation of the Flavor Creation sample, we have generated over 20 Millions events. For the generation of the Flavor Excitation and Gluon Splitting events, we have generated over 1 billion events.

6.3 Event Selection

The raw generated MC samples has a much softer b-quark p_T spectrum than the real data sample, since there are kinematic requirements on the daughter particles from the signal B meson in data. To simulate the data sample, we select MC events using the corresponding kinematic requirements made on the data sample,

1. Require the two muons from the signal B with $p_T > 2.$, and $|\eta| < 2.5$

2. Require the kaon from the signal B with $p_T > 1.$, and $|\eta| < 2.5$

These selection requirements remove mostly the events where the b-quark populates the low p_T region. The flavor creation, flavor excitation and gluon splitting events have efficiencies of passing these event selection criteria of 2.94%, 2.38% and 2.27% respectively.

6.4 The Combined $b\bar{b}$ Sample

The generated MC samples before the event selection show that the fractions of the flavor creation, flavor excitation and gluon splitting subprocesses are 0.45:0.41:0.14. This agrees qualitatively with the results in Ref. [61], see Fig. 6.5. In Ref. [61], R.F.Field has done a systematic study of sources of b-quark production at the Tevatron.

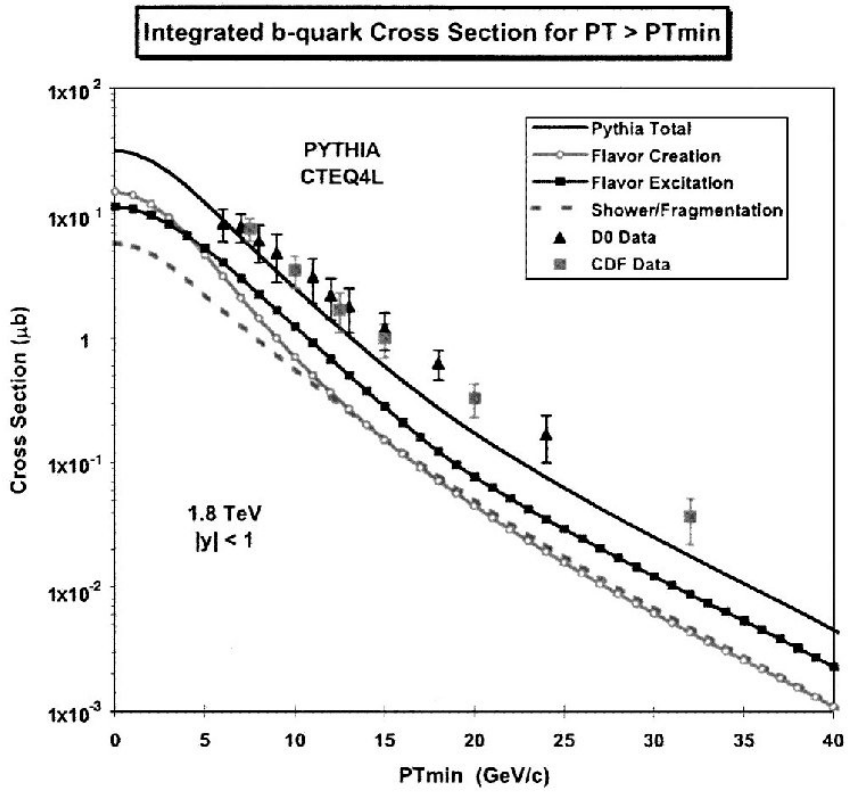

Figure 6.5: The inclusive b-quark differential cross section for $|y| < 1$ for proton-antiproton collisions at 1.8 GeV resulting from PYTHIA 6.158 [CTEQ4L, $p_T(\text{hard}) > 0$].

The ratios given above change to 0.51:0.37:0.12 after the event selection criteria are applied. Based on these ratios, we create the combined MC samples which include all three subprocesses. The signal B p_T distribution of the combined sample agrees well with the one of the data sample, see Fig. 6.6.

To estimate any potential systematic errors from the fractions, we calculate the change in tagging power by changing the fraction of FC, fixing the ratio between FE and GS (the tagging power of these two subprocesses are similar, so changing the ratio between the two does not cause a significant change). We

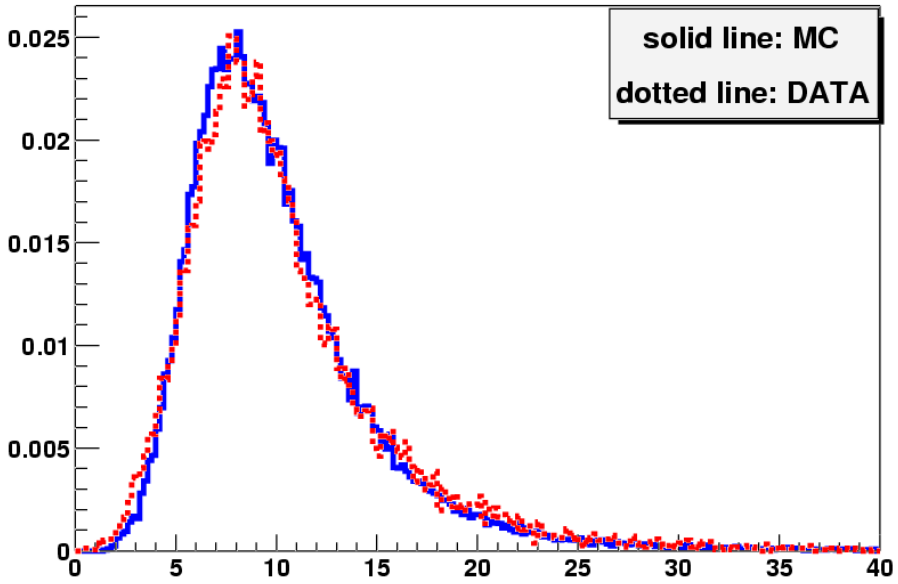

Figure 6.6: The comparison of the p_T distributions for the signal B between the MC combined sample and data sample.

found a 1% change in the fraction of the flavor creation subprocess causes less than 0.15% absolute change in resulting tagging diltution. This uncertainty is negligible compared with the statistical error we have in data sample.

6.4.1 B Mixing Effects on the Tagging Results

For all Monte Carlo samples, the mixing of B_s^0 is turned on with the mixing parameter $x_s = 20.0$. However, we have turned off the mixing of B_d system for two reasons: 1) For the neutral MC sample, the signal $\bar{B}^0/B^0$ is forced to decay to $J/\psi K_s$, turning on the mixing will cause the opposite side B_d to also decay to $J/\psi K_s$ which should rarely happen. 2) Although we can turn on the mixing of the charged B sample without causing the problem in reason (1), this makes it

hard to compare tagging results between charged and neutral samples.

However, the effects of mixing must be understood before a correct comparison between MC and data can be made. We have evaluated the effects of the B_d mixing to the tagging results using our MC B^- and $\bar{B}^0$ samples in the following way

1. divide $B^-/\bar{B}^0$ sample into two sub-samples: 1) the opposite side B is B_d, 2) the opposite side B isn't B_d.

2. For sub-sample 1, we measure the tagging efficiency and dilution, ϵ_{nomix} and D_{nomix}; then we flip the charge of each daughter particle from the B_d, measure the tagging results, getting ϵ_{mix} and D_{mix}; Then the tagging results for sub-sample 1 with the B_d mixing on is obtained by combining the two results based on the method discussed in Appendix A. The fraction of the mixed events is taken to be 18%.

3. For sub-sample 2, we measure the tagging efficiency and dilution, ϵ_2 and D_2 respectively.

4. Finally, we combined the two sub-samples to get the tagging results for the total sample in the case that the B_d mixing is on. The fraction of sub-sample 1 is taken to be 40%.

For the B^- sample, with B_d mixing on, the tagging dilution is estimated to be

92% of the dilution of the events with the B_d mixing off. For $\bar{B}^0$ sample, the tagging dilution is estimated to be 90% of the events with the B_d mixing off. The tagging efficiency is almost unchanged in both samples.

Chapter 7

JETQ Tagging results with Monte Carlo Samples

In this chapter, we will give the tagging results for the generated MC samples, including both charged B and neutral B samples. No asymmetry has been found in the tagging results between the generated B^- and B^+ samples, as well as between the generated B^0 and $\bar{B}^0$ samples. Between the charged and neutral sample, the charged sample has a much larger dilution. The reason has been discussed in the last chapter.

For the reconstructed samples, we have found $B^-(\bar{B}^0)$ sample has slightly higher tagging dilution than $B^+(B^0)$ sample. This asymmetry is caused by a small excess of positive tracks (in favor of the tagging of B^- sample) in the reconstructed events.

In order to show that the difference in topologies between the three subprocesses (flavor creation, flavor excitation, and gluon splitting) cause different tagging results, we will first outline the tagging results for each subprocess for the B^- sample. Then the tagging results for the combined samples will be outlined.

7.1 The Tagging Results of the Flavor Creation Subprocess

The actual value of the tagging power of the JETQ algorithm depends on the $\Delta\phi$ separation. Table 7.1 shows the tagging results of the JETQ tagging algorithm running on the MC Flavor Creation sample with different $\Delta\phi$ cuts. It can be seen that both the dilution and the tagging power drop as the $\Delta\phi$ cut increases. This is caused by the two reasons that we have discussed: 1) the larger the $\Delta\phi$ cut, the more "Fb daughters" are removed, making the tagging power drop (We have shown in chapter 5 that the "Fb daughters" help increase the tagging power in charged B samples); 2) the larger the $\Delta\phi$ cut, the more "OB daughters" are removed, and we have shown these particles are crucial in the JETQ tagging.

On the other hand, the tagging efficiency increases as $\Delta\phi$ is increased. This

$\Delta\phi$ cut	D	ϵ	ϵD^2
0.7	28.3% ± 0.35%	39.7% ± 0.11%	3.17% ± 0.08%
1.0	26.0% ± 0.34%	42.6% ± 0.11%	2.88% ± 0.07%
1.5	23.8% ± 0.32%	47.9% ± 0.11%	2.72% ± 0.07%
2.0	21.9% ± 0.30%	55.1% ± 0.11%	2.64% ± 0.07%
2.4	19.1% ± 0.28%	63.2% ± 0.11%	2.30% ± 0.07%

Table 7.1: The results of the tagging dilution (D), efficiency (ϵ) and tagging power (ϵD^2) for the flavor creation B^- events, based on the $\Delta\phi$ requirements of 0.7, 1.0, 1.5, 2.0 and 2.4

is because the larger $\Delta\phi$ cut leads to less tracks in the candidate track list (sometimes the number of tracks in the list drops to only 1 track), making the jet charge value shift to either +1 or -1, and moving away from 0. Since events with $|Q| < 0.2$ are labeled as untagged, the larger $\Delta\phi$ cut leads to a higher tagging efficiency.

The tagging results also show dependences on the p_T of the signal side B meson (the p_T of the opposite side B is unknown). Figure 7.1 shows the tagging efficiency, dilution and tagging power as functions of the signal side B meson p_T and different $\Delta\phi$ cuts. The tagging efficiency drops as the p_T of the signal B increases. This is because the larger the p_T of the signal B, the larger the multiplicity of tracks in an event, thus more tracks in the candidate track list. The larger multiplicity makes the jet charge more likely to be neutral (i.e. close to 0), causing lower tagging efficiency.

$\Delta\phi$ cut	D	ϵ	ϵD^2
0.7	28.3% ± 0.34%	40.1% ± 0.11%	3.23% ± 0.08%
1.0	26.8% ± 0.33%	42.9% ± 0.11%	3.09% ± 0.08%
1.5	24.8% ± 0.32%	48.2% ± 0.11%	2.96% ± 0.08%
2.0	22.9% ± 0.30%	55.2% ± 0.11%	2.89% ± 0.08%
2.4	19.6% ± 0.28%	63.3% ± 0.11%	2.43% ± 0.07%

Table 7.2: The results of the tagging dilution (D), efficiency (ϵ) and tagging power (ϵD^2) for the flavor creation B^+ events, based on the $\Delta\phi$ requirements of 0.7, 1.0, 1.5, 2.0 and 2.4

On the other hand, the tagging dilution increases as the p_T of the signal B increases. This is due to the strong p_T correlations between the two b-quarks in the flavor creation subprocess, which is shown in Fig. 6.3 (the top plot). The larger the p_T of the opposite side B, the more likely for the tagging algorithm to tag correctly, since the "OBdau particles" are more likely to dominate over all other relevant particles in terms of p_T. But this correlation is not true in the flavor excitation and gluon splitting subprocesses, since there is no p_T correlations between the two b-quarks in those subprocesses.

Finally, we find no tagging asymmetry between the generated MC B^- and B^+ samples in the JETQ algorithm. The tagging results for B^+ sample is shown in table 7.2

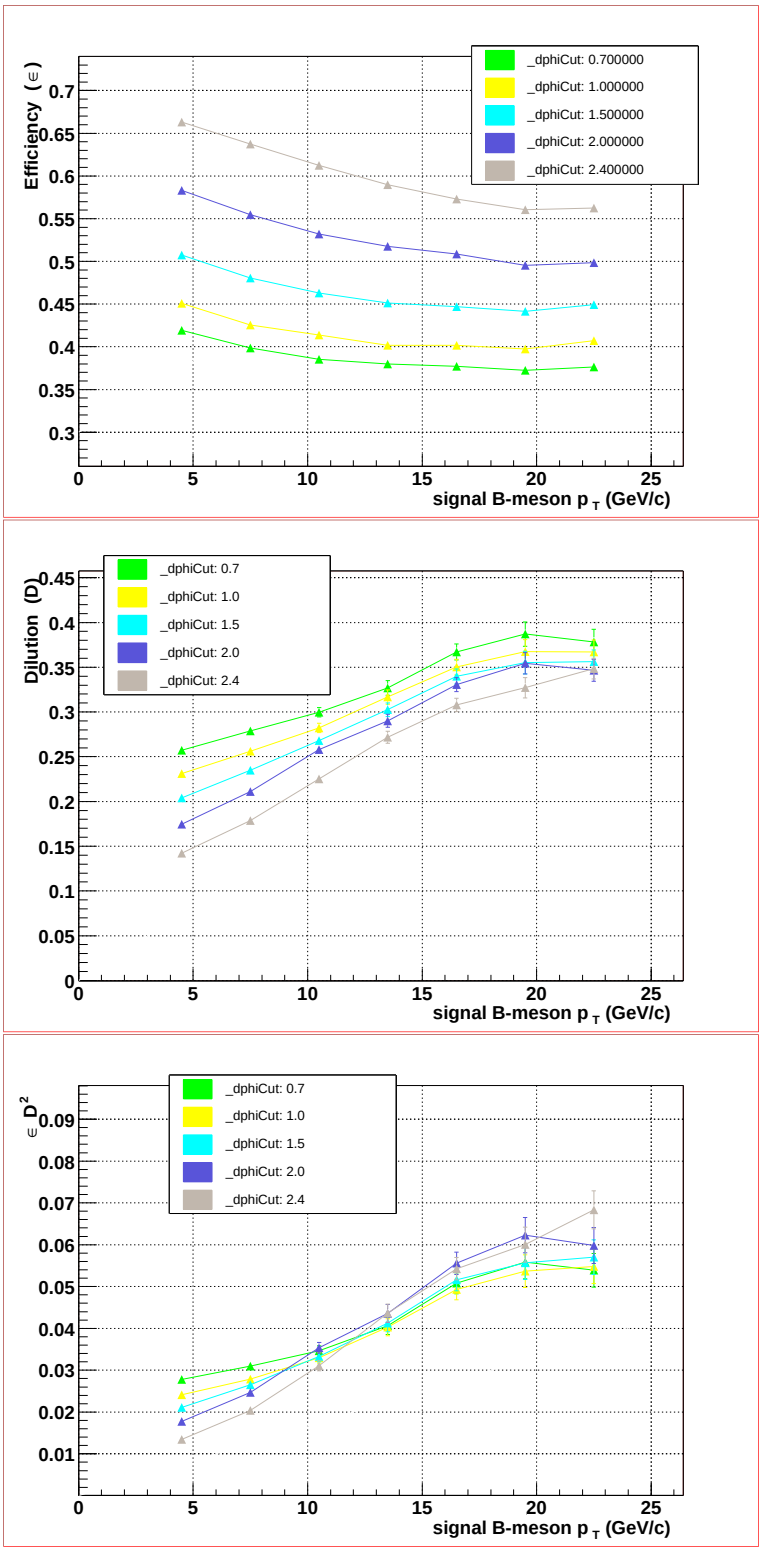

Figure 7.1: The tagging results for the MC Flavor Creation B- sample. The top plot is the tagging power, the medium plot is for the tagging dilution, the bottom plot is for the tagging efficiency. The x-axis is the p_T of the signal side B meson, different lines corresponding different $\Delta\phi$ cuts.

$\Delta\phi$ cut	D	ϵ	ϵD^2
0.7	15.1% ± 0.53%	36.4% ± 0.16%	0.83% ± 0.06%
1.0	12.5% ± 0.52%	39.1% ± 0.16%	0.61% ± 0.05%
1.5	9.9% ± 0.49%	44.6% ± 0.16%	0.44% ± 0.04%
2.0	6.7% ± 0.45%	51.8% ± 0.16%	0.23% ± 0.03%
2.4	4.3% ± 0.42%	60.2% ± 0.16%	0.11% ± 0.02%

Table 7.3: The results of the tagging dilution (D), efficiency (ϵ) and tagging power (ϵD^2) for the flavor excitation subprocess, based on the $\Delta\phi$ requirements of 0.7, 1.0, 1.5, 2.0 and 2.4

7.2 The tagging results of the Flavor Excitation Subprocess

Since the tagging power is a function of the tagging efficiency and the dilution, its results are known once the results of the other two variables are given. We will skip the plots of the tagging power.

Table 7.3 shows the tagging results of the MC Flavor Excitation B^- sample with different $\Delta\phi$ cuts. The tagging dilutions are poorer compared with those of the flavor creation subprocess. This is caused by the following two reasons: 1) the $\Delta\phi$ correlations between the two b-quarks are much weaker in the flavor excitation subprocess. 2) the two b-quarks do not have the p_T correlations as found in the flavor creation subprocess.

The tagging efficiency as a function of the p_T of the signal side B meson is

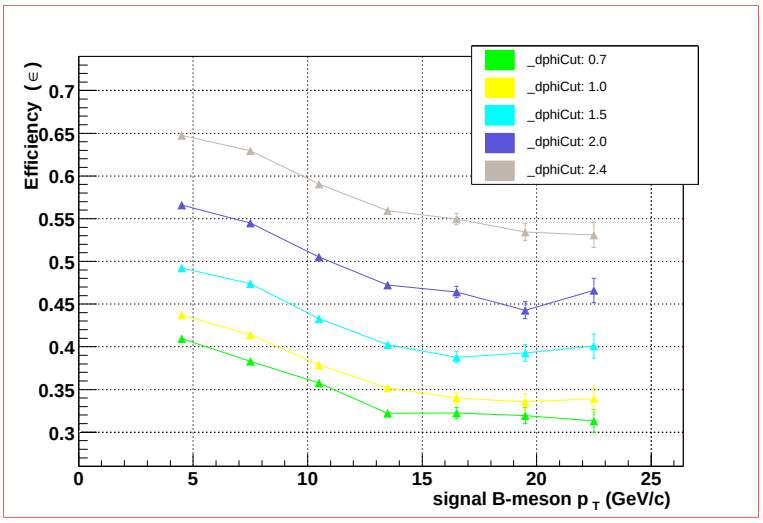

Figure 7.2: The tagging efficiency for the MC Flavor Excitation B- sample. .

similar to that of the flavor creation subprocess. However, the tagging dilution plots are distinctly different. The plots are shown in figures 7.2 and 7.3. Since there is no p_T correlation between the two b-quarks, it is natural to see the tagging power is approximately flat over all p_T region.

7.3 The Tagging Results of the Gluon Splitting Subprocess

The topology and kinematics of b-quarks are similar in the flavor excitation subprocess and gluon splitting subprocess. Their tagging results are also similar.

Table 7.4 shows the tagging results of the MC gluon splitting B^- sample while using different $\Delta\phi$ cuts.

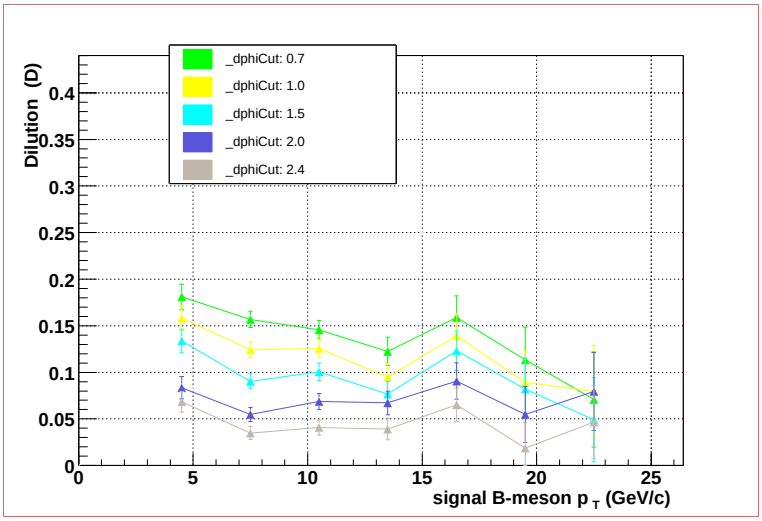

Figure 7.3: The tagging dilution for the MC Flavor Excitation B- sample. .

$\Delta\phi$ cut	D	ϵ	ϵD^2
0.7	16.5% ± 1.04%	33.9% ± 0.29%	0.92% ± 0.12%
1.0	13.3% ± 1.00%	36.9% ± 0.30%	0.65% ± 0.10%
1.5	9.5% ± 0.93%	42.6% ± 0.30%	0.38% ± 0.08%
2.0	6.7% ± 0.86%	50.4% ± 0.31%	0.23% ± 0.06%
2.4	3.5% ± 0.79%	59.4% ± 0.30%	0.07% ± 0.03%

Table 7.4: The results of the tagging dilution (D), efficiency (ϵ) and tagging power (ϵD^2) for the gluon splitting subprocess, based on the $\Delta\phi$ requirements of 0.7, 1.0, 1.5, 2.0 and 2.4

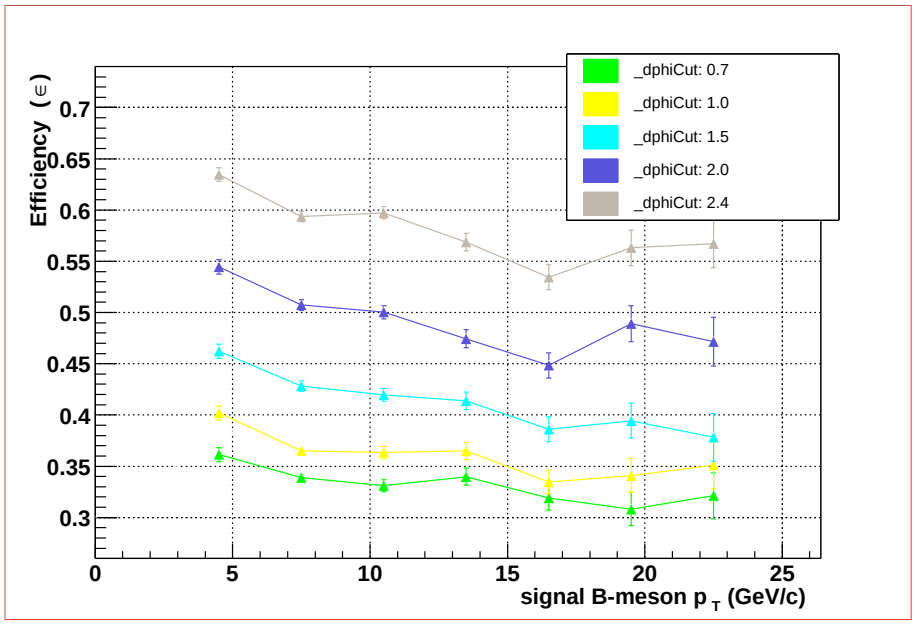

Figure 7.4: The tagging efficiency for the MC Gluon Splitting B- sample. .

The results of the tagging power as functions of the signal side B p_T are shown in the figure 7.4 and 7.5.

7.4 The tagging results of the combined sample

As discussed in chapter 6, we have obtained the combined sample by taking the fractions of the three subprocesses of 0.51:0.37:0.12. Table 7.5 shows the tagging results of the combined B^- sample while using different $\Delta\phi$ cuts. Table 7.6 shows the tagging results of the combined $\bar{B}^0$ sample while using different $\Delta\phi$ cuts.

The tagging results of the combined B^- sample as functions of the signal

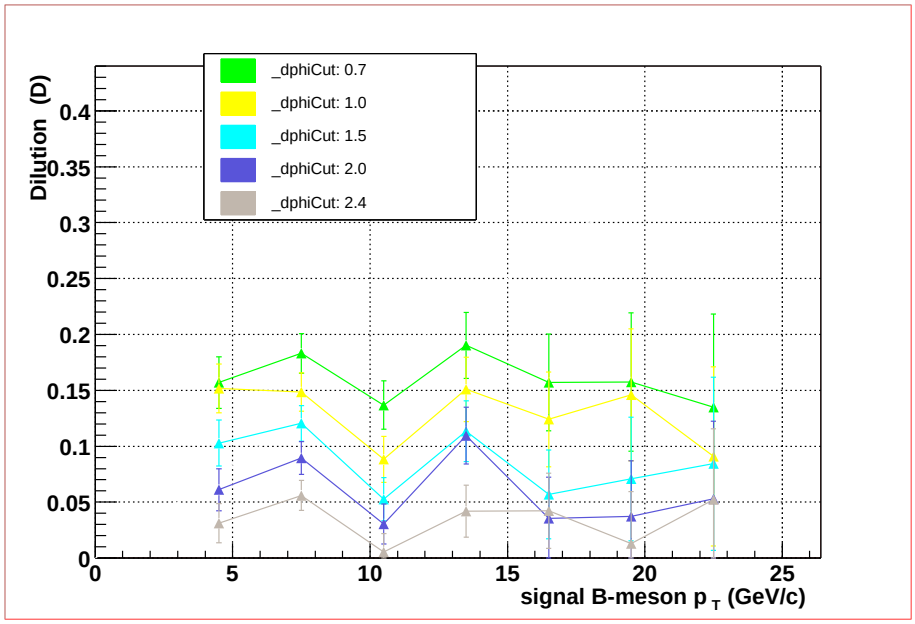

Figure 7.5: The tagging dilution for the MC Gluon Splitting B- sample. .

$\Delta\phi$ cut	D	ϵ	ϵD^2
0.7	22.5% ± 0.42%	37.4% ± 0.13%	1.90% ± 0.07%
1.0	20.0% ± 0.41%	40.3% ± 0.13%	1.61% ± 0.07%
1.5	17.5% ± 0.38%	45.7% ± 0.13%	1.40% ± 0.06%
2.0	14.8% ± 0.36%	52.9% ± 0.13%	1.17% ± 0.06%
2.4	12.3% ± 0.33%	61.4% ± 0.13%	0.93% ± 0.05%

Table 7.5: The results of the tagging dilution (D), efficiency (ϵ) and tagging power (ϵD^2) for the combined B^- sample, based on the $\Delta\phi$ requirements of 0.7, 1.0, 1.5, 2.0 and 2.4

$\Delta\phi cut$	D	ϵ	ϵD^2
0.7	14.5% ± 0.4%	37.4% ± 0.1%	0.78% ± 0.04%
1.0	14.7% ± 0.4%	40.2% ± 0.1%	0.87% ± 0.04%
1.5	14.6% ± 0.4%	45.8% ± 0.1%	0.97% ± 0.05%
2.0	13.9% ± 0.3%	53.1% ± 0.1%	1.02% ± 0.05%
2.4	11.5% ± 0.3%	61.7% ± 0.1%	0.81% ± 0.04%

Table 7.6: The results of the tagging dilution (D), efficiency (ϵ) and tagging power (ϵD^2) for the combined $\bar{B}^0$ sample, based on the $\Delta\phi$ requirements of 0.7, 1.0, 1.5, 2.0 and 2.4

side B p_T are shown in the figure 7.6, 7.7 and 7.8. The tagging results of the combined $\bar{B}^0$ sample as functions of the singal side B p_T are shown in the figure 7.9, 7.10 and 7.11.

7.5 The fully reconstructed sample

Up to now, we have discussed the results based on the generated MC samples. To understand the effects of the DØ simulation and reconstruction to the tagging results, we have run part of the combined sample into the DØ simulation and reconstruction packages. Moreover, we have run the combined sample after full reconstruction through the same package (*d0root_btag*) that is used to obtain the real data samples. The tagging results for the reconstructed sample (including both B^- and B^+ samples) are shown in table 7.7.

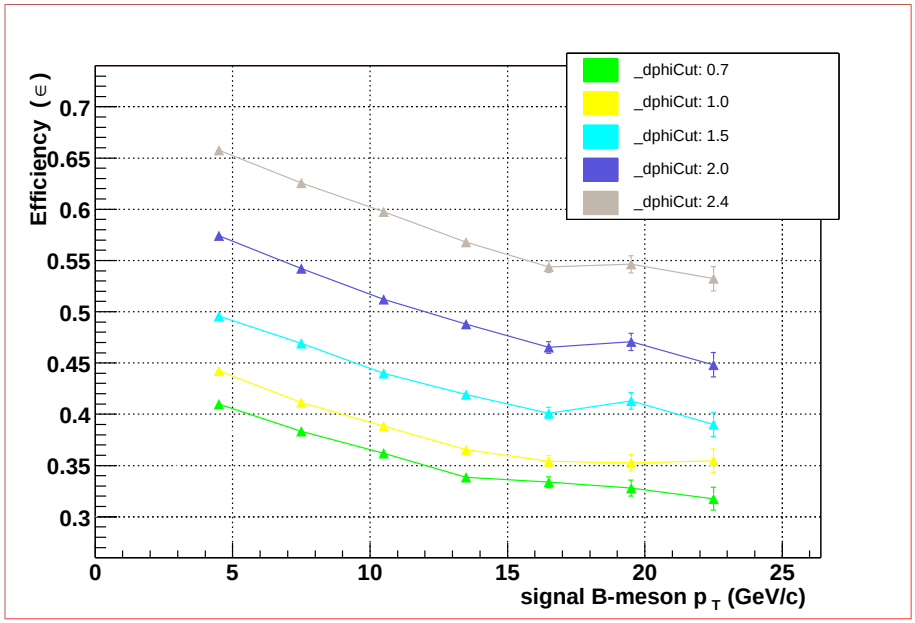

Figure 7.6: The tagging efficiency for the combined MC B- sample.

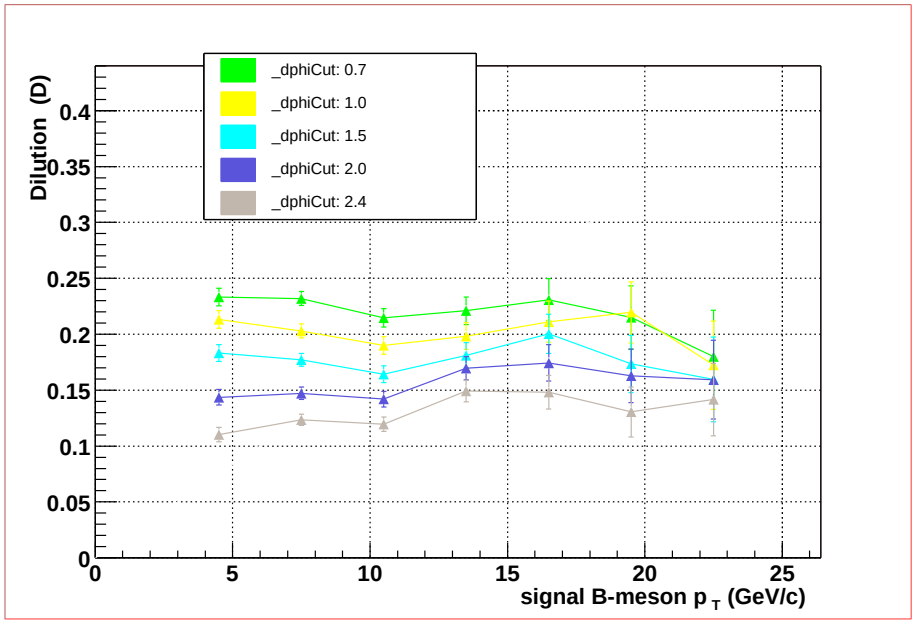

Figure 7.7: The tagging dilution for the combined MC B- sample.

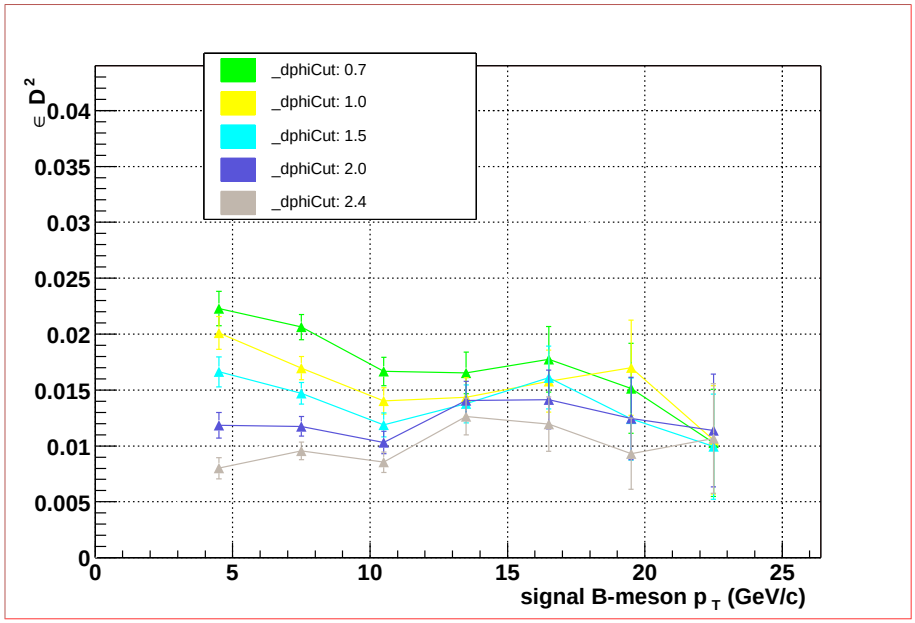

Figure 7.8: The tagging power for the combined MC B- sample.

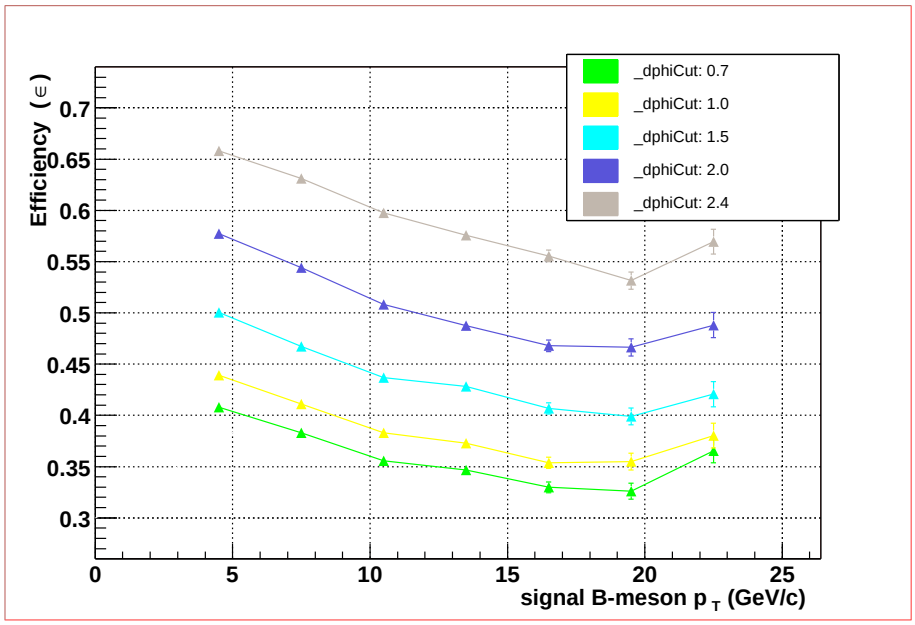

Figure 7.9: The tagging efficiency for the combined MC $\bar{B}^0$ sample.

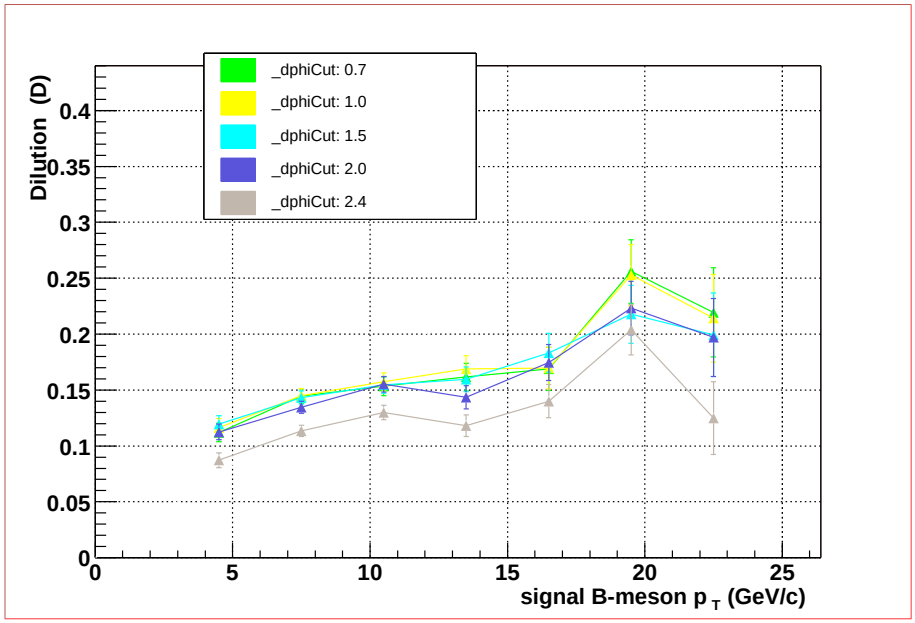

Figure 7.10: The tagging dilution for the combined MC $\bar{B}^0$ sample.

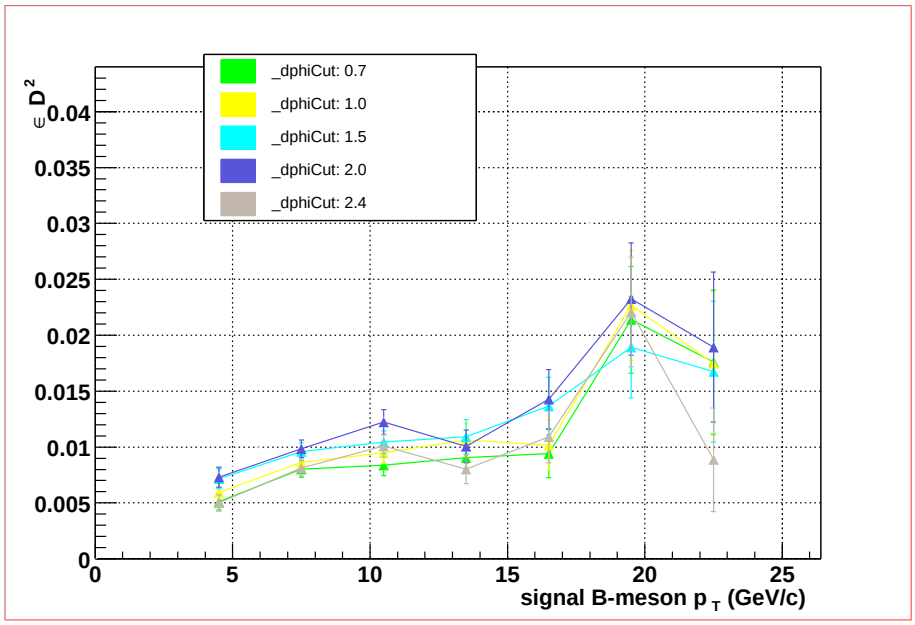

Figure 7.11: The tagging power for the combined MC $\bar{B}^0$ sample.

$\Delta\phi$ cut	D	ϵ	ϵD^2
0.7	19.1% ± 0.68%	40.3% ± 0.22%	1.47% ± 0.10%
1.0	17.0% ± 0.66%	44.6% ± 0.22%	1.29% ± 0.10%
1.5	15.0% ± 0.63%	49.5% ± 0.22%	1.08% ± 0.09%
2.0	13.0% ± 0.59%	56.3% ± 0.22%	0.95% ± 0.09%
2.4	11.3% ± 0.56%	63.8% ± 0.22%	0.82% ± 0.08%

Table 7.7: The results of the tagging dilution (D), efficiency (ϵ) and tagging power (ϵD^2) for the fully reconstructed sample, based on the $\Delta\phi$ requirements of 0.7, 1.0, 1.5, 2.0 and 2.4

Compared with the tagging results of the MC generated samples, the tagging dilution on average drops 13.4%. The major reason that acounts for the decrease of the tagging dilutions is the imperfection of the global track reconstruction efficiency. The tracking efficiency in the central region is about 90%, and in the forward region ($|\eta| > 1.7$) is about 80%.

7.6 The asymmetry between the B^+ and B^- reconstructed samples

In addition to the decrease of the tagging dilutions, a small asymmetry in the tagging dilutions between the B^+ and B^- events have also been observed in the reconstructed samples. The tagging results for the B^+ and B^- reconstructed samples are shown in the table 7.8 and 7.9 respectively.

$\Delta\phi cut$	D	ϵ	ϵD^2
0.7	18.6% ± 0.9%	41.9% ± 0.3%	1.45% ± 0.14%
1.0	15.8% ± 0.9%	44.7% ± 0.3%	1.12% ± 0.12%
1.5	13.9% ± 0.8%	49.6% ± 0.3%	0.96% ± 0.12%
2.0	12.5% ± 0.8%	56.6% ± 0.3%	0.88% ± 0.11%
2.4	10.5% ± 0.8%	63.8% ± 0.3%	0.71% ± 0.10%

Table 7.8: The results of the tagging dilution (D), efficiency (ϵ) and tagging power (ϵD^2) for the fully reconstructed B^+ sample, based on the $\Delta\phi$ requirements of 0.7, 1.0, 1.5, 2.0 and 2.4

$\Delta\phi cut$	D	ϵ	ϵD^2
0.7	19.5% ± 0.9%	41.7% ± 0.3%	1.59% ± %
1.0	18.0% ± 0.9%	44.2% ± 0.3%	1.44% ± %
1.5	15.7% ± 0.8%	49.2% ± 0.3%	1.21% ± %
2.0	13.6% ± 0.8%	55.9% ± 0.3%	1.03% ± %
2.4	12.2% ± 0.8%	63.8% ± 0.3%	0.94% ± %

Table 7.9: The results of the tagging dilution (D), efficiency (ϵ) and tagging power (ϵD^2) for the fully reconstructed B^- sample, based on the $\Delta\phi$ requirements of 0.7, 1.0, 1.5, 2.0 and 2.4

The asymmetry is related to the fact that the reconstructed events have a small excess of positive tracks in the reconstructed events. In the reconstructed samples, including both charge and neutral B samples, we have found 1.6% more positive tracks than negative tracks. This excess of positive tracks cause the $B^-(\bar{B}^0)$ sample have larger tagging dilution.

Chapter 8

JETQ tagging results of the data Sample

In this chapter, we give the JETQ tagging results for the data sample with fully reconstructed $B^{\pm} \rightarrow J/\psi K^{\pm}$ decays. The results are compared with the predictions from the MC, and found to be consistent within the statistical error.

8.1 Data Sample Selection

The data sample used in this analysis was collected using the dimuon trigger during the period from September 2002 through November 2003, corresponding to an integrated luminosity of 225 pb^{-1}. After reconstructing the data, events with at least one reconstructed J/ψ formed from a pair of opposite charged muons are selected. The data is then analyzed using the d0root_btag (version 9.1) package to find events with fully reconstructed $B^{\pm} \rightarrow J/\psi K^{\pm}$ decays. The following selection criteria have been used:

1. J/ψ reconstruction: Each muon from the J/ψ must have $p_T \geq 1.5$ GeV/c with at least one hit in the silicon tracking detector (SMT). The dimuon mass ($M_{\mu\mu}$) is required to be in the range of 2.8 to 3.3 GeV/c. The χ^2 of the the dimuon vertex fit must be $\chi^2 < 10$.

2. $B^{\pm}$ reconstruction: The $B^{\pm}$ is reconstructed through finding a common vertex formed by the reconstructed J/ψ and a track (assumed to be $K^{\pm}$). The candidate $K^{\pm}$ is required to have $p_T \geq 1.0$ GeV/c, with a $\chi^2 < 10$ for its contribution to the fit of the B vertex. In addition, the B vertex, which has three tracks (two muons, one kaon), is required to have a $\chi^2 < 20$. Next, we impose a collinearity requirement. We require the cosine of the angle between the B momentum direction and the vector from the primary vertex to the B decay vertex to be greater than 0.9. Finally, we require the decay length significance (decay length divided by its error) of B to be > 4.5. The resulting $B^{\pm}$ sample is shown in Fig. 8.1.

8.1.1 Track Selection Criteria

The following track selection criteria are applied to select the candidate tracks used in the JETQ tagging process:

1. The tracks used to reconstruct the signal B are explicitly excluded, i.e. a pair of muons and the $K^{\pm}$ in Fig. 5.5.

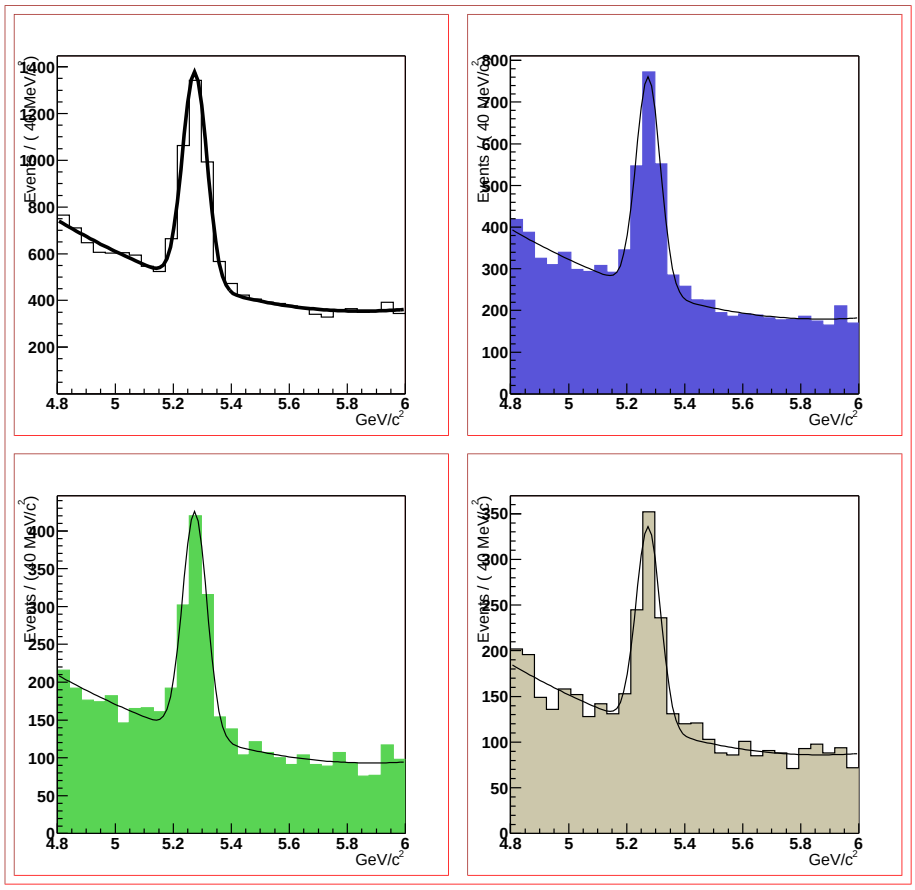

Figure 8.1: Invariant mass for candidate $B^{\pm} \rightarrow J/\psi K^{\pm}$ events. The data sample was obtained by the DØ RunII detector, with an integrated luminosity of 225 pb^{-1}. The first plot is for all candidate B, the second plot is for tagged events, the third is for the correctly tagged events, the last is for the incorrectly tagged events.

2. A track is required to have at least 1 SMT hits (corresponding to SMT hits in at least one layers of the silicon detectors).

3. A track is required to have a χ^2/dof (Degree of Freedom) of less than 9. This is a track quality requirement on the reconstructed tracks from the global track fitting.

4. A track is required to have a 2-dimensional DCA (Distant Closest Approach to the primary vertex) of less than 0.2 cm. The requirement reduces the asymmetry on the tagging power between B^+ and B^- samples. The asymmetry is caused by a small excess of positive tracks. This is believed to be a detector effect.

5. A track must have $p_T > 0.5$ GeV/c.

6. A track must have the z vertex displacement from the primary vertex of less than 2.0 cm. This requirement suppresses the "Minbias particles" from entering the jet.

7. To tag an event, the calculated jet charge Q is required to be $|Q| \geq 0.2$. An event has no tag if $|Q| < 0.2$.

8. A $\Delta\phi$ requirement on the separation of a track with respect to the direction of the signal b-quark is applied.

8.2 JETQ Tagging Results

The JETQ algorithm has been run on the selected data sample. The invariant candidate B mass plots are drawn in Fig. 8.1. The number of tagged events is drawn by fitting each tagging plot with a Gaussian function and a polynomial function of order 2.

The flavor of the signal b-quark is known from the charge of the kaon in the fully reconstructed $B^{\pm} \rightarrow J/\psi K^{\pm}$ decay. If the signal b quark has positive charge, then a negative jet charge gives the correct tag, a positive jet charge gives an incorrect tag. The tagging efficiency (ϵ) and dilution (D) are calculated by Eq. (1) and (2). The errors of ϵ and D are calculated using binomial errors. The error of the tagging power is calculated by the error propagation formula, assuming ϵ and D are independent. The detail of the error estimation is discussed in chapter 9.

Table 8.1 shows the results for $\Delta\phi$ separations of 0.7, 1.2 and 2. In all three cases, the tagging dilutions are consistent with the predictions of the MC sample.

We have checked the robustness of the results by varying all associated requirements involved in the JETQ tagging algorithm by both small and large amount. For the small variation, each requirement has been varied by $\pm$ 1% around the selected value. For the large variation, we have taken the p_T cut at

$\Delta\phi cut$	D	ϵ	ϵD^2
0.7	15.2% ± 4.0%	52.1% ± 1.7%	1.20% ± 0.64%
1.2	13.7% ± 3.9%	56.9% ± 1.7%	1.07% ± 0.60%
2.0	8.14% ± 3.7%	64.8% ± 1.6%	0.43% ± 0.39%

Table 8.1: DATA sample with $B^{\pm} \rightarrow J/\psi K^{\pm}$, 225 pb^{-1}

0.25 and 1.0; the Δz cut at 1., 3.; the $|Q|$ cut at 0.1, 0.3; χ^2/dof at 3, 6. The resulting dilutions agree with the predictions from the MC sample within the statistical error.

Chapter 9

Error Estimation for the Tagging Results

This chapter describes how to estimate the statistical errors for the tagging efficiency and dilution. Two methods are discussed. They are the method of binomial error and error propagation. It is shown that the two methods yield identical results when no background exists, and yield consistent results when there is background. By comparing the two methods, we conclude that using binomial errors can be applied more generally and is used in our final analysis.

We will only discuss the error estimate for ϵ. The same approach applies to the error estimate for D after replacing Eq. 5.2 with $D = 1 - 2 * \frac{N_B}{N_T}$.

9.1 Method A: Binomial Error Approach

Each candidate event has a fractional probability (ϵ) of being tagged, the total number of tagged events (N_T) obeys a binomial distribution. Therefore the

error in ϵ is given by

$$\sigma_\epsilon = \sqrt{\epsilon(1-\epsilon)}\frac{\sqrt{N}}{N} \tag{9.1}$$

The error in ϵ is due to the binomial error in counting N_T for a fixed input number of events N. The error for N_T is given by $\sqrt{\epsilon(1-\epsilon)N}$.

It should be noted that the binomial error in N_T is calculated analytically based on the binomial distribution probability density function [62], thus no approximation is used.

9.2 Method B: Error Propagation Approach

An alternative method of estimating σ_ϵ is through the propagation of errors. To do this, we first transform Eq. 5.1 into

$$\epsilon = \frac{N_T}{N_T + N_U} \tag{9.2}$$

where N_T and N_U are independent of each other. The error in a quantity f that is a function of two independent variables through the propagation of errors is [63]

$${\sigma_f}^2 = \left(\frac{\partial f}{\partial x}\right)^2 {\sigma_x}^2 + \left(\frac{\partial f}{\partial y}\right)^2 {\sigma_y}^2 \tag{9.3}$$

One should keep in mind that this equation is based on the approximation that the first derivative changes only slightly over a few σ around the mean value, thus the higher order differential terms in the Taylor expansions can be ignored.

Applying Eq. 9.3 to Eq. 9.2 gives

$$\sigma_\epsilon = \sqrt{(1-\epsilon)^2 \frac{\sigma_{N_T}^2}{N^2} + \epsilon^2 \frac{\sigma_{N_U}^2}{N^2}} \tag{9.4}$$

σ_{N_T} is interpreted as the statistical error of N_T, which is equal to $\sqrt{N_T}$. Same for σ_{N_U}. Inserting the statistical errors into the equation, one ends up with Eq. 9.1.

$$\begin{aligned}
\sigma_\epsilon &= \sqrt{(1-\epsilon)^2 \frac{N_T}{N^2} + \epsilon^2 \frac{N_U}{N^2}} \\
&= \sqrt{(1-2\epsilon)\frac{N_T}{N^2} + \epsilon^2 \frac{N_T}{N^2} + \epsilon^2 \frac{N_U}{N^2}} \\
&= \sqrt{(1-2\epsilon)\frac{N_T}{N^2} + \epsilon^2 \frac{N}{N^2}} \\
&= \sqrt{(1-2\epsilon)\frac{N_T}{N^2} + \epsilon \frac{N_T}{N^2}} \\
&= \sqrt{(1-\epsilon)}\epsilon \frac{\sqrt{N}}{N}
\end{aligned}$$

Therefore, the two methods give identical result if there is no background.

9.3 Adding Background

In a real experiment, N is extracted by fitting the mass distribution, which has both signal and backgrounds, e.g. the candidate B invariant mass plot shown in Fig. 8.1. The error $\sqrt{N}$ underestimates the error in N by ignoring the existence of background. The background must be considered in calculating the error in N. Therefore Eq. 9.1 and 9.4 must be modified.

For the method of binomial error, one can replace $\sqrt{N}$ in Eq. 9.1 with the error from a fit to N. The fitting code calculates the statistical error in N by including the contribution from the background. The replacement is based on the following observation: although the binomial error in ϵ is not directly caused by the statistical error in N, the magnitude of it is proportional to the statistical error in N. The validity of this replacement has been verified using toy MC studies.

After this substitution, The binomial error becomes

$$\sigma_\epsilon = \sqrt{\epsilon(1-\epsilon)}\frac{\delta N}{N} \tag{9.5}$$

δN stands for the fitted error in N. One can do a similar substitution for method B. The error through propagation becomes:

$$\sigma_\epsilon = \sqrt{(1-\epsilon)^2\frac{(\delta N_T)^2}{N^2} + \epsilon^2\frac{(\delta N_U)^2}{N^2}} \tag{9.6}$$

δN_T and δN_U stand for the fitted error in N_T and N_U respectively.

9.4 Equivalence of Method A and B When Background Exists

In this section, we will show that the two methods yield approximately the same result. First we define the following terms:

- B_N: The total number of background events in the sample under the B mass peak;

- B_T: The total number of background events in the tagged sample under the B mass peak;

- B_U: The total number of background events in the un-tagged sample under the B mass peak,

with the constraint $B_N = B_T + B_U$.

With background, the error in the fitted total number of B events is directly given by the fitting code. However, to show method A and B yield approximately the same result, we need to write this error (δN) in an analytical form as a function of N and B_N. Since the magnitude of δN has contributions from the statistical fluctuations of N and B_N, which are independent of each other, a natural assumption is

$$\delta N = \sqrt{(\sigma_N)^2 + (\sigma_{B_N})^2} \equiv \sqrt{N + B_N} \tag{9.7}$$

Similar assumptions apply to the error estimate for δN_T and δN_U.

Studies using both a Toy MC and data samples have shown that this is a very good approximation. The difference between the fitted results and the analytically calculated result is less than 3%.

To compare the results from the method of binomial error and the method through propagation of errors, we compare the term $N^2\sigma_\epsilon^2$ derived from Eq. 9.5 to that derived from Eq. 9.6. Applying Eq. 9.7 to Eq. 9.5, squaring and multiplying it by N^2 give

$$N^2\sigma_\epsilon^2 = (1-\epsilon)\epsilon N + (1-\epsilon)\epsilon B_N \tag{9.8}$$

We make similar substitutions of δN_T and δN_U in Eq. 9.6, squaring and multiplying it by N^2 give

$$N^2\sigma_\epsilon^2 = (1-\epsilon)^2(T+B_T) + \epsilon^2(U+B_U) \tag{9.9}$$

T and N are related by the tagging efficiency ϵ. In order to relate B_T and B_U to B_N, we define the tagging efficiency for the background events by ϵ'. Now we change each tag and un-tag variable in Eq. 9.9 to the corresponding quantities of the largest sample (i.e. N and B_N for the total B sample) by using $T = \epsilon N$, $B_T = \epsilon' B_N$, etc. Eq. 9.9 becomes

$$\begin{aligned}
N^2\sigma_\epsilon^2 &= (1-\epsilon)^2(\epsilon N + \epsilon' B_N) + \epsilon^2((1-\epsilon)N + (1-\epsilon')B_N) \\
&= [(1-\epsilon)^2\epsilon + \epsilon^2(1-\epsilon)]N + [(1-\epsilon)^2\epsilon' + \epsilon^2(1-\epsilon')]B_N \\
&= (1-\epsilon)\epsilon N + (\epsilon' - 2\epsilon'\epsilon + \epsilon^2)B_N \quad (define\ \ \delta_{\epsilon\epsilon'} = \epsilon - \epsilon') \\
&= (1-\epsilon)\epsilon N + (1-\epsilon)\epsilon B_N - (1-2\epsilon)\delta_{\epsilon\epsilon'} B_N
\end{aligned}$$

Comparing the resulting terms with those in Eq. 9.8, the only difference is the additional term $(1-2\epsilon)\delta_{\epsilon\epsilon'} B_N$. The difference that this additional term adds

on the error estimate of ϵ between method A and B is

$$\sqrt{\frac{(1-2\epsilon)\delta_{\epsilon\epsilon'}B_N}{(1-\epsilon)\epsilon N + (1-\epsilon)\epsilon B_N}}$$

It is much easier to estimate the upper limit of this difference defined as

$$a = \sqrt{\frac{(1-2\epsilon)\delta_{\epsilon\epsilon'}}{(1-\epsilon)\epsilon}} \tag{9.11}$$

We tested two algorithms (SLT and JETQ) in the B flavor tagging studies, both yield $|a| < 2\%$. More generally this additonal term should have negligible contributon as long as the two efficiencies are similar to each other, i.e. $\delta_{\epsilon\epsilon'} \ll \epsilon$. This condition holds in general because a big difference between ϵ and ϵ' implies additional cuts exist to clean up one's sample. In addition, if $\epsilon = 50\%$, the difference between the two methods becomes 0. In the cases of the efficiency being close to 0% or 100%, method B will have the problem that one of the samples has a very small size, causing the fit to be less reliable.

9.5 Conclusions

Since both methods yield equivalent results, each of them can be used in estimating the error in ϵ and D. However, method A is strongly recommended over method B. This is because method A uses the measured quantity of two larger samples (N and N_T) rather than method B which uses smaller samples (N_T and N_U). This makes method A more reliable because of higher statistics in

the samples used. This is especially important when the efficiency is close to 0% or 100%.

Chapter 10

The CP Asymmetry Parameter $\sin(2\beta)$ Measurement

In this chapter, the JETQ algorithm is used to measure the CP asymmetry parameter $\sin(2\beta)$ using both the time integrated and time dependent methods. Similar studies have been conducted in CDF Run I project, yielding $\sin(2\beta) = -0.31 + 0.81 - 0.85$ [64]. We first discuss the data sample selection in section 10.1. In section 10.2, we discuss the time integrated $\sin(2\beta)$ measurement. In section 10.3, we discuss the time dependent $\sin(2\beta)$ measurement. In section 10.4, we compare toy MC simulations of the $\sin(2\beta)$ measurement with the results of the data sample.

10.1 Data Sample Selection

To measure the CP asymmetry parameter $\sin(2\beta)$, we use the data sample of fully reconstructed $B \to J/\psi K_s$ decays. The data sample we used is in AADST format, different from the charged data sample used in the last section. The following selection criteria have been used in the reconstruction of candidate B events:

1. J/ψ reconstruction: Each muon from the J/ψ must have $p_T \geq 1.5$ GeV/c with at least two hits in the silicon tracking detector. The dimuon mass ($M_{\mu\mu}$) is require to be in the range 2.8 to 3.35 GeV/c^2.

2. K_s reconstruction: Each pion from the K_s must have $p_T \geq 0.4$ GeV/c. The invariant mass ($M_{\pi\pi}$) of two pions is required to be in the range 0.465 to 0.52 GeV/c^2.

3. $B^0/\bar{B}^0$ reconstruction: The B is reconstructed through finding a common vertex formed by the reconstructed J/ψ and K_s. In addition, the B vertex is required to have a $\chi^2 < 25$. Next, we impose a collinearity requirement. We require the cosine of the angle between the B momentum direction and the vector from the primary vertex to the B decay vertex to be greater than 0.9.

The resulting $B \rightarrow J/\psi K_s$ candidate events and associated tagged events are shown in Fig. 10.1, the tagging plots correspond to a $\Delta\phi$ cut of 2.0. To count the number of tagged $\bar{B}^0$ and B^0 events, we have fit the invariant mass plots of $\bar{B}^0$-tagged and B^0-tagged events with a Gaussian function (signal) plus a linear function (background).

In running the JETQ tagging algorithm, the same track selection criteria applied in the last section has been used, except that the minimum p_T requirement is changed to 0.25 GeV/c. We find from the MC studies that a smaller p_T cut yields a larger tagging power. A larger tagging power generally leads to a smaller statistical error on the measured value of $\sin(2\beta)$ value. Therefore, we select the minimum p_T requirement at 0.25 GeV/c (0.25 GeV/c is the p_T cutoff in the DØ reconstruction software).

10.2 The Time Integrated $\sin(2\beta)$ Measurement

CP violation in B-mesons leads to a difference in the decay rates of $\bar{B}_d$ and B_d into CP eigenstates f_{CP}. For $B \rightarrow J/\psi K_s$, the decay rates are given by [65]

$$\Gamma_f(t) = e^{-\Gamma t} \times (1 - \sin 2\beta \times \sin \Delta m t) \quad (10.1)$$

$$\bar{\Gamma}_f(t) = e^{-\Gamma t} \times (1 + \sin 2\beta \times \sin \Delta m t) \quad (10.2)$$

where $\Gamma_f(t)$ stands for $B_d \rightarrow f_{CP}$, $\bar{\Gamma}_f(t)$ stands for $\bar{B}_d \rightarrow f_{CP}$, Δm is the mass difference between between the heavy and light CP eigenstates, β is one of the

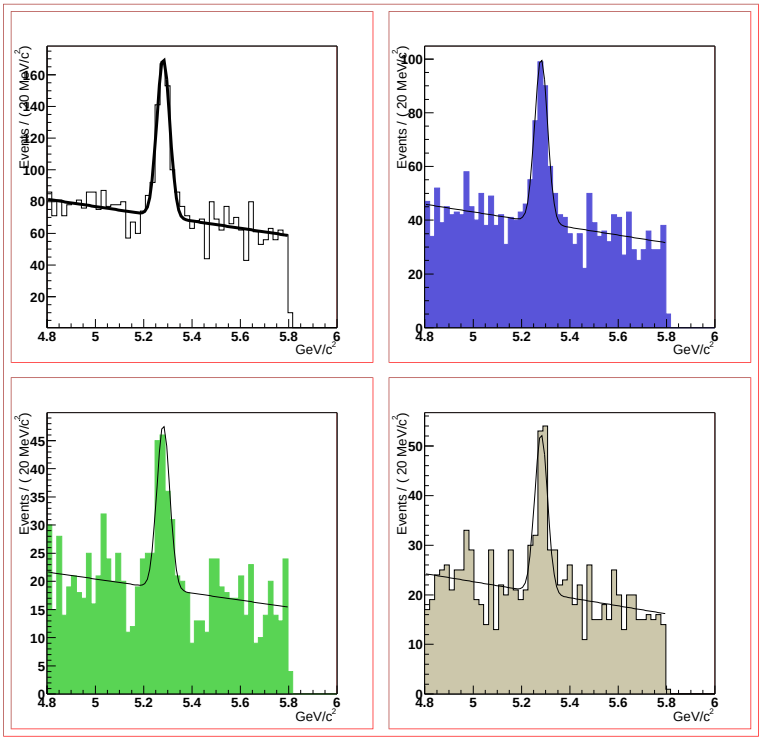

Figure 10.1: Invariant mass for candidate $B \to J/\psi K_s$ events. The data sample was obtained by DØ Run II detector, corresponding to 225 pb^{-1} luminosity. The first plot is for all candidate B, the second plot is for tagged events, the third is for the events tagged as B^0, the last is for the events tagged as $\bar{B}^0$.

angles of the unitarity triangle.

For a time integrated measurement, the value of $\sin(2\beta)$ is given by

$$\sin(2\beta) = \frac{1+x_d^2}{x_d}\frac{\bar{N}-N}{\bar{N}+N} \tag{10.3}$$

where x_d is the mixing parameter, $x_d = \Delta m/\Gamma$. $\frac{\bar{N}-N}{\bar{N}+N}$ is defined as the raw asymmetry A_{raw}, where N is the number of B^0 events, $\bar{N}$ is the number of $\bar{B}^0$ events. A_{raw} is derived from the tagged asymmetry A_{tag}

$$A_{raw} = \frac{A_{tag}}{D} \tag{10.4}$$

$$A_{tag} = \frac{\bar{T}-T}{\bar{T}+T} \tag{10.5}$$

where D is the tagging dilution, $\bar{T}$ is the number of events tagged as $\bar{B}$, T is the number of events tagged as B. The error in the measurement of $\sin(2\beta)$ is given by

$$\delta[2\beta)] = \frac{1+x_d^2}{x_d}\frac{1}{\sqrt{N\epsilon D^2}} = \frac{1+x_d^2}{x_d}\frac{\sqrt{N\epsilon}}{N\epsilon D} \tag{10.6}$$

where $\sqrt{N\epsilon}$ is the statistical error due to the number of tagged events ($T_{tot} = N\epsilon$). If there were no background in the data sample, the above equation would be correct. With background in the data sample, the contribution from the background must be included. As discussed in the previous chapter, the contribution from the background can be included by replacing $\sqrt{N\epsilon}$ with the error from the fit of T_{tot}.

Processing the neutral B sample through the JETQ algorithm determines the production flavor of the reconstructed B in each event. If the jet charge is

$\Delta\phi cut$	$\bar{B}$ tags	B tags	$\bar{B} - purity$	$B - purity$	$\sin(2\beta)$
1.2	74.1	65.3	39%	38%	1.04± 1.88
1.5	76.1	70.4	38%	37%	0.63± 1.86
1.7	88.5	65.8	39%	34%	2.47± 1.75
2.0	99.1	90.5	40%	40%	0.82± 1.80
2.3	82.8	116.4	34%	43%	−3.52± 2.34
2.6	104.8	104.4	37%	37%	0.06± 2.71

Table 10.1: The resulting tags and the corresponding $\sin(2\beta)$ values for the time integrated measurement.

negative, the flavor of the reconstructed B-meson is tagged as a B, if the charge is positive, the flavor of the reconstructed B-meson is tagged as $\bar{B}$.

Table 10.1 gives the tagging results for different values of $\Delta\phi$ (1.2, 1.5, 1.7, 2.0, 2.3 and 2.6). As a check of the reliability of our result, we have included the purity of each fit invariant mass plot. The purity is defined as $S/(S+B)$, where S stands for the number of signal events, B stands for the number of background events. The B-tags and $\bar{B}$-tags show small difference in the purities when the $\Delta\phi$ requirement is 1.2, 1.5, 2.0, 2.6, but large differences when the $\Delta\phi$ requirement is 1.7 and 2.3. Since the purity is expected to be similar for both B-tags and $\bar{B}$-tags, a large difference implies that the fitting results are affected by statistical fluctuations of the signal and/or background, causing a much larger fluctuation in the measured value of $\sin(2\beta)$. As a crosscheck, we have make the same plots with different $\Delta\phi$ requirements using the charge B data sample. We find that

the difference in the purities is small (around 1% to 2%).

The measured values of $\sin(2\beta)$ with different $\Delta\phi$ cuts are listed in Table 10.1. With the $\Delta\phi$ cut at 2.0, the measurement gives $\sin(2\beta) = 0.82 \pm 1.80$. Given the world average value of $\sin(2\beta) = 0.74 \pm 0.04$ [66], to confirm that $\sin(2\beta)$ is non-zero, we need approximately 30k tagged B events. This corresponds to an integrated luminosity of 3.3 fb^{-1}, assuming the current triggering and reconstruction efficiencies.

We have checked the robustness of this measurement using the same method as in the robustness check of the tagging results in chapter 8. All of the resulting values of $\sin(2\beta)$ are consistent within the statistical error of the values in Table 10.1 .

The systematic error associated with this measurement is mainly from the uncertainty in the fractions of the three subprocesses FC:FE:GS. At the present time there are no measurements of these fractions. Our MC studies show that the fractions are 0.51:0.37:0.12. If we assume a 5% relative change in the fraction of the Flavor Creation events, the corresponding systematic error in the measured $\sin(2\beta)$ value (for $\Delta\phi = 2.0$) will be 0.05. If we assume a 10% relative change in the fraction, the correponding systematic error will be 0.11. Compared with the current statistical error, this is negligible.

	$\Delta\phi = 1.2$		$\Delta\phi = 2.0$		$\Delta\phi = 2.3$	
Proper Decay Length(μm)	$\bar{B}$ tags	B tags	$\bar{B}$ tags	B tags	$\bar{B}$ tags	B tags
0 - 200	12.1	11.7	18.5	31.2	11.8	41.0
200 - 400	26.1	23.9	30.5	20.1	24.6	21.5
400 - 800	21.8	15.4	29.1	19.4	32.2	33.1
800 - 1400	12.4	9.8	15.2	11.2	13.5	11.7
1400 - 2000	1.00	4.94	4.70	7.12	1.25	7.14

Table 10.2: The number of tags for the time dependent measurement.

10.3 The Time Dependent $\sin(2\beta)$ Measurement

The CP parameter $\sin(2\beta)$ can be written in terms of a time dependent asymmetry as

$$A(t) = \frac{\bar{\Gamma}(t) - \Gamma(t)}{\bar{\Gamma}(t) + \Gamma(t)} = \sin 2\beta \times \sin \Delta m t \tag{10.7}$$

The time dependent measurement is made using this equation, where we bin the proper decay length into 5 bins: 0-200 μm, 200-400 μm, 400-800 μm, 800-1400 μm, and 1400-2000 μm. The resulting tags are listed in table 10.2, corresponding to 3 different $\Delta\phi$ requirements; 1.2, 2.0, 2.3.

Based on the tags in table 10.2, $A_{tag}(t)$ for each proper decay length bin is calculated. To calculate the raw asymmetry $A_{raw}(t)$, the tagging dilution is needed for each specific $\Delta\phi$ requirement. For a given $\Delta\phi$ requirement, the tagging dilution is assumed to be same in each proper decay length bin.

In the tagging studies of the charged B data sample discussed in the last section, we have shown that the tagging dilution is expected to drop by 13.6% due to the imperfect track reconstruction efficiency and 8% due to the mixing of the opposite side B_d. We find for the neutral B sample, the tagging dilution is expected to drop by the same amount due to reconstruction and 10% due to the B_d mixing. Therefore, the tagging dilution used for the neutral B data sample is $D_{MC} * 0.866 * 0.9$, where D_{MC} is the tagging dilution of the MC sample.

We plot the raw asymmetry in Fig. 10.2 and fit it using the function $A_{CP} \sin[(x/0.03) * \Delta m]$, where Δm is fixed at 0.489 ps^{-1}, A_{CP} is the fitted value of $\sin 2\beta$. From Fig. 10.2, the fit values of $\sin 2\beta$ are 1.03 ± 1.16, 1.80 ± 1.15, -0.35 ± 1.23 for $\Delta\phi$ cut at 1.2, 2.0 and 2.3 respectively. Again, we have checked robustness of the measurements, all changes in the results can be explained by statistical fluctuations.

10.4 Toy Monte Carlo Studies

As a test of the statistical error measured in the data sample, a large number of toy Monte Carlo "experiments" have been run. For the time dependent $\sin(2\beta)$ measurement, the toy Monte Carlo "experiments" provide good estimates of the shape of the raw asymmetry plots for the data sample of specific size.

In the toy MC "experiments", the size of the tagged B events N has been

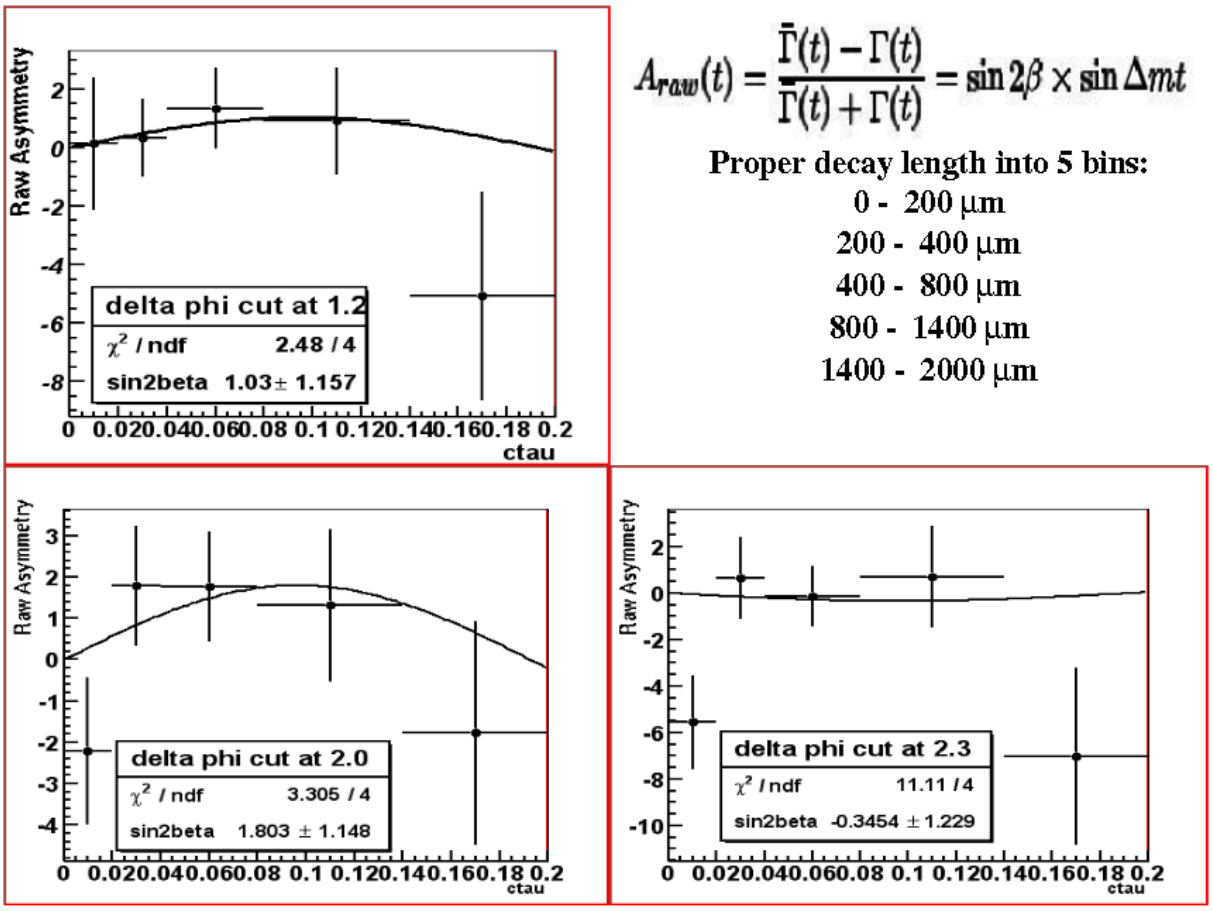

Figure 10.2: The time dependent measurement of CP asymmetry parameter $\sin(2\beta)$ with different $\Delta\phi$ cuts.

chosen to be 200, 2000, and 1,000,000 respectively. The tagging efficiency is estimated to be 60% from the result of the data sample. In the simulation, the number of events of B and $\bar{B}$ are generated according to a binomial distribution following A_{raw} defined in Eq. 10.3. The number of tagged events are generated using a binomial generator following Eq. 5.2, while allowing the tagging dilutions of B and $\bar{B}$ to fluctuate. The magnitude of the fluctuation is determined by the size of the associated sample, while the background contribution is also included. Finally, the value of $\sin(2\beta)$ is assumed to be 0.8.

In testing the statistical error of the integrated measurement, two sets of 100 toy MC "experiments" have been generated. Table 10.3 shows the results of several toy MC "experiments" from the first set. The mean and standard deviation of each set are listed in table 10.4. The MC simulation with 200 tagged events yields a statistical error that agrees very well to the one found in the real data sample.

For the time dependent measurement, the probabilities of B and $\bar{B}$ decaying to $J/\psi K_s$ at time t are simulated by the probability distribution function given in Eq. 10.2. The resulting raw asymmetry plots are shown in Fig. 10.3, 10.4 and 10.5. For each MC "experiment", two plots are shown. The left plot corresponds to the raw asymmetry derived from the generated B and $\bar{B}$ events in each proper decay length bin. The right plot corresponds to the raw asymmetry

Toy MC samples	200 events	2000 events	1000,000 events
1	2.65	1.54	0.73
2	2.00	0.51	0.74
3	-0.33	0.61	0.81
4	1.14	0.54	0.80
5	4.98	1.08	0.77
6	1.38	0.19	0.84
7	3.32	1.08	0.83
8	1.45	1.80	0.78
more	...	...	...

Table 10.3: Examples of the toy MC results for the time integrated $\sin(2\beta)$ measurement.

Toy MC experiments	200 events	2000 events	1000,000 events
set 1	0.65 ± 1.98	0.77 ± 0.68	0.80 ± 0.034
set 2	1.06 ± 1.72	0.89 ± 0.52	0.80 ± 0.025

Table 10.4: The toy MC results of the time integrated $\sin(2\beta)$ measurement. Each set includes 100 MC "experiments"

derived from the "tagged events" (which have included the fluctuation of dilutions). Comparing the data sample's statistical error with that of the toy MC "experiments" with the same sample size (200 tagged events), the data sample have proper errors. The results of the study also show that the raw asymmetry plots of data sample have reasonable shapes.

10.5 Conclusions

We have developed the opposite side jet charge tagging algorithm in the DØ Run II project. The tagging performance has been measured using $B^{\pm} \rightarrow J/\psi K^{\pm}$ data sample of integrated luminosity 225 pb^{-1}. The measured dilution has been compared with the predictions from the fully reconstructed Monte Carlo samples, and good agreement has been found.

With the JETQ tagging algorithm, we have performed measurements of the CP asymmetry parameter $\sin(2\beta)$ using $B \rightarrow J/\psi K_s$ data sample, corresponding to the same luminosity. Using a $\Delta\phi$ cut of 2.0, for the time integrated measurement, we measure $\sin(2\beta)$ to be 0.82 ± 1.80; for the time dependent measurement, we measure $\sin(2\beta)$ to be 1.80 ± 1.15.

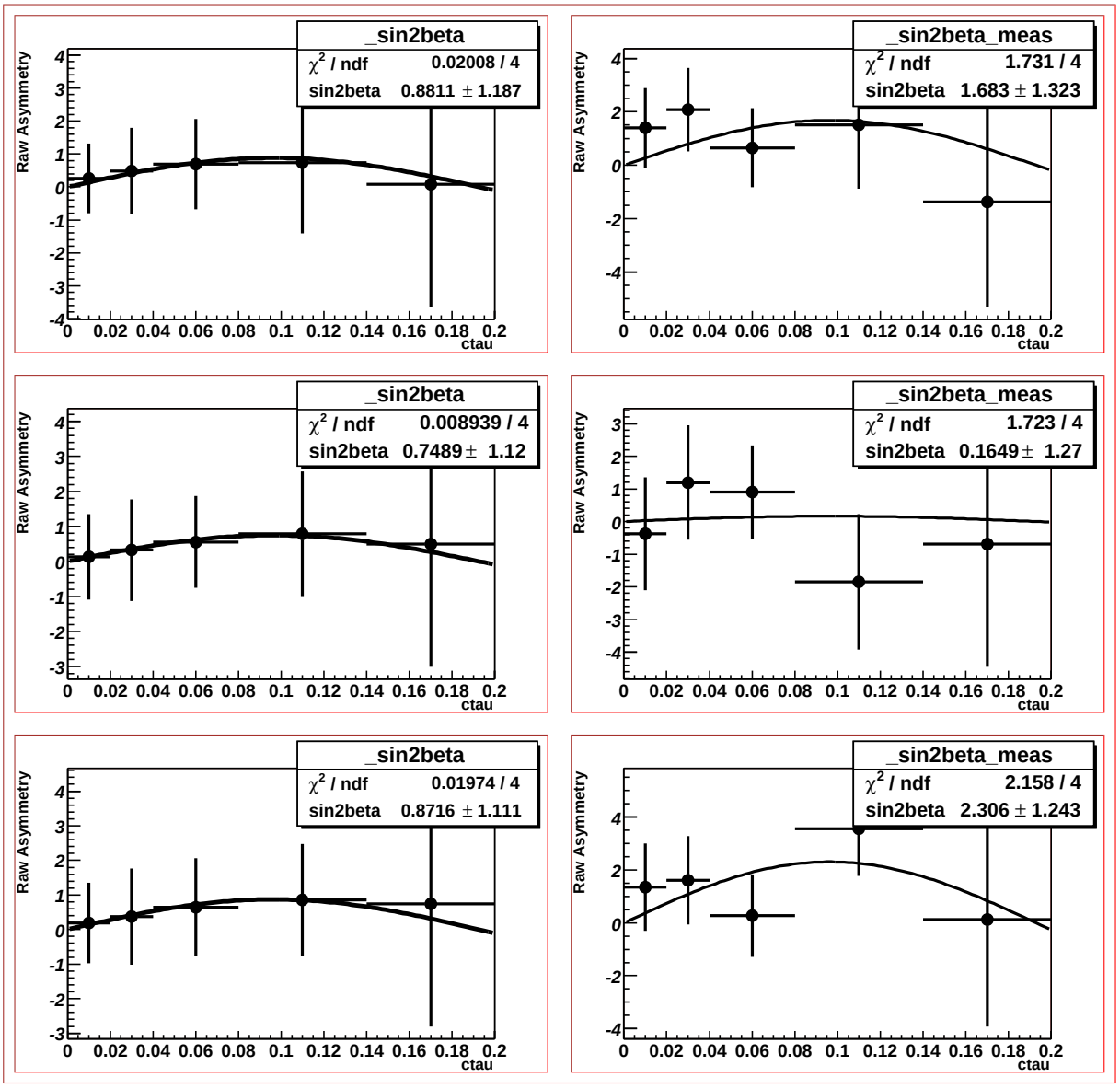

Figure 10.3: Toy MC simulation of the time dependent measurement with 200 tagged events. Three MC "experiments" have been run. Each run corresponds to a pair of plots in a given row. The left plot corresponds to the raw asymmetry derived from the generated B and $\bar{B}$ events in each proper decay length bin. The right plot corresponds to the raw asymmetry derived from the "tagged events" (which have included the fluctuation of dilutions).

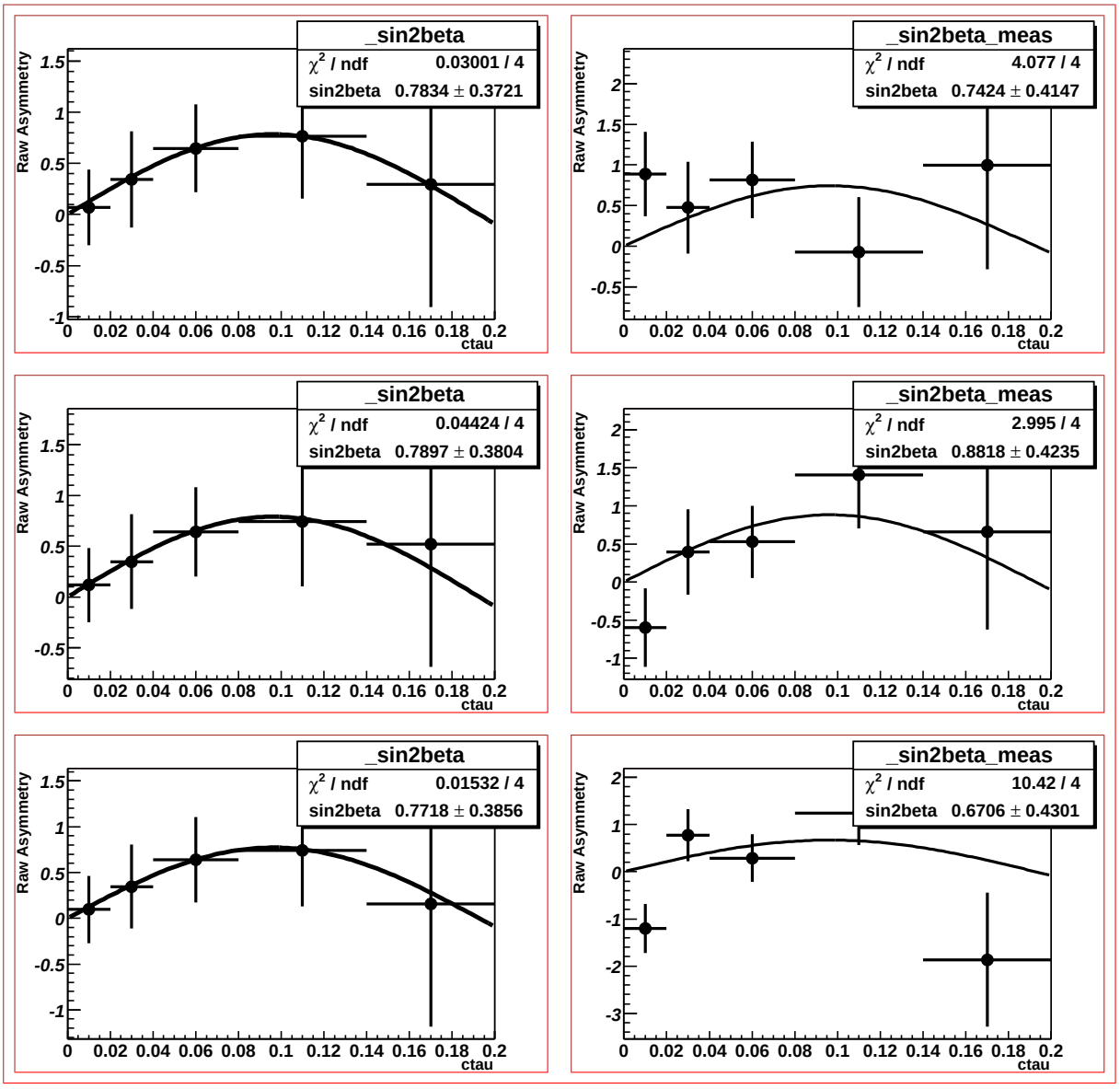

Figure 10.4: Toy MC simulation of the time dependent measurement with 2000 tagged events.

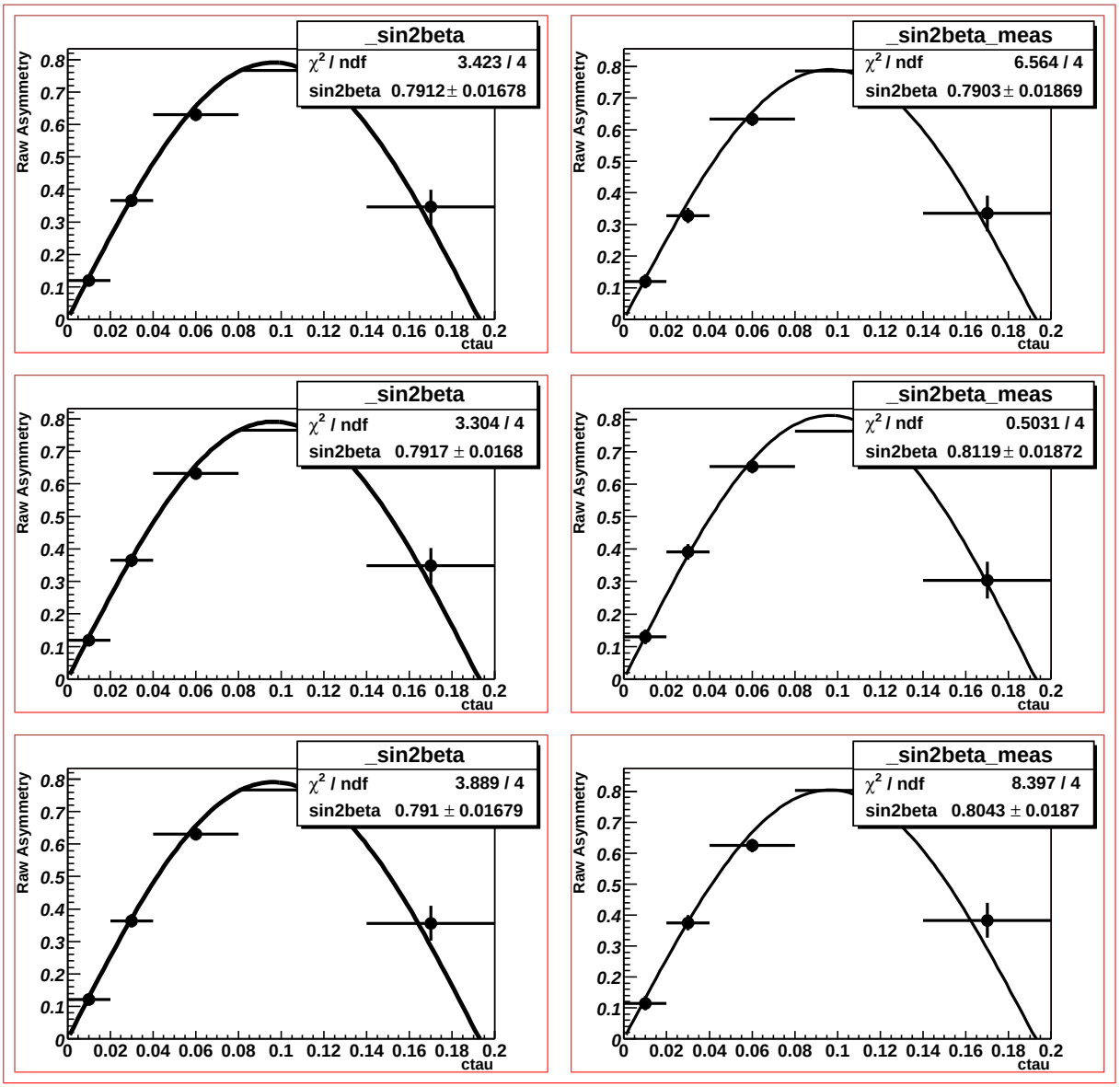

Figure 10.5: Toy MC simulation of the time dependent measurement with 1M tagged events.

Appendix A

The combination of tagging powers from two sub-samples

In this chapter, we discuss how to combine the tagging powers of two sub-samples if the tagging powers of the two sub-samples have been measured.

Suppose there is a sample with N events, a fraction f_1 of the sample belongs to sub-sample type I, a fraction f_2 of the sample belongs to sub-sample type II, $f_1 + f_2 = 1$. Suppose sub-sample I has tagging efficiency ϵ_1 (relative to the sub-sample I) and dilution D_1, sub-sample II has tagging efficiency ϵ_2 (relative to the sub-sample II) and dilution D_2, the tagging efficiency and dilution of the total sample are given by

$$\epsilon = f_1\epsilon_1 + f_2\epsilon_2 \tag{A.1}$$

$$D = \frac{f_1\epsilon_1 D_1 + f_2\epsilon_2 D_2}{f_1\epsilon_1 + f_2\epsilon_2} \tag{A.2}$$

The combined tagging power is

$$\begin{aligned} \epsilon D^2 &= \frac{(f_1\epsilon_1 D_1 + f_2\epsilon_2 D_2)^2}{f_1\epsilon_1 + f_2\epsilon_2} \\ &= \frac{f_1^2\epsilon_1^2 D_1^2 + 2f_1 f_2 \epsilon_1\epsilon_2 D_1 D_2 + f_2^2\epsilon_2^2 D_2^2}{f_1\epsilon_1 + f_2\epsilon_2} \\ &= f_1\epsilon_1 D_1^2 + f_2\epsilon_2 D_2^2 - \frac{f_1 f_2 \epsilon_1\epsilon_2 (D_1 - D_2)^2}{f_1\epsilon_1 + f_2\epsilon_2} \end{aligned} \tag{A.3}$$

From Eq. $A.3$, the tagging power from two sub-samples is not simply the addition of each fraction weighted individual tagging power. There is a cross term, making the combined tagging power generally smaller than the sum of the two individual tagging powers.

Bibliography

[1] David Griffiths, **Introduction to Elementary Particles**, Wiley & Sons, Inc.

[2] Francis Halzen, Alan D. MArtin, **Quarks & Leptons**, John Wiley & Sons Inc.

[3] C.N. Yang and T.D. Lee, Phys. Rev., **96** (1954) 191.

[4] E. Abers and B.W. Lee, Phys. Rep. C, **9** (1973) 1.

[5] P.W. Higgs, Phys. lett., **12** (1964) 132; P.W. Higgs, Phys. Rev. lett., **13** (1964) 508

[6] P. Nason, S. Dawson and R.K. Ellis, *Nucl. Phys. B* **327** (1989) 49, erratum ibid. **B335**(1990)260.

[7] P. Nason, "Heavy quark production", in Heavy Flavors, eds A.J. Buras and M. Lindner, Advanced Series on Directions in High Energy Physics, (World Scientific, Singapore, 1992)

[8] J.C. Collins and Wu-Ki Tung, *Nucl. Phys. B* **360** (1991) 3.

[9] P. Nason, S. Dawson and R.K. Ellis, *Nucl. Phys. B* **303** (1988) 607.

[10] W.T. Giele et al. hep-ph/0104052 v1 4 Apr. 2001.

[11] M. Neubert. Submitted to Journal of Mod. Phys. A, April 1996, hep-ph/9604412.

[12] Particle Data Group Collaboration, Phys. Rev. D, part 1, Jul. 2002.

[13] Bphysics at the Tevatron RunII and Beyond. FERMILAB-Pub-01/197

[14] J.H Christenson et al. Phys. Rev. Lett. **13**, 128 (1964)

[15] A.B. Carter and A.I. Sanda, Phys. Rev. **D23**, 1567 (1981)

[16] N. Cabibbo. Phys. Rev. Lett. **10**, 531 (1963)

[17] S. Abachi *et al.* Nucl. Inst. Meth., **A338** , 185-253 (1994).

[18] The DØ Run II Upgrade, see $http://www-d0.fnal.gov/hardware/upgrade/upgrade.html$

[19] Helen T.Edwards, *Ann. Rev. Nucl. Part. Sci.*, **35:** 605-660, 1985.

[20] DØ Collaboration, S. Abachi et al., Nucl. Instrum. and Meth. A **338** (1994) 185.

[21] M.T.P. Roco, "Analysis of SMT Beam Tests Data", DØ Note #3405.

[22] DØ Tracking/Vertexing Web site, $http://www-d0.fnal.gov/global\_tracking/$.

[23] D.D. Pitzl et al., Nucl. Phys. B (Proc. Suppl.) **23**A (1991) 340; H.J. Ziock et al., IEEE Trans. Nucl. Sci. NS-**38** (1991) 269.

[24] A Silicon Track Trigger for the DØ Experiment in Run II, DØ Note, #3516.

[25] DØ Central Tracking Group Web site, $http://d0server1.fnal.gov/projects/SciFi/cft\_home.html$.

[26] The DØ SciFi Tracking Trigger Technical Design Report(v5), DØ Note, #3551.

[27] B. Hoeneisen and D. Lincoln, "Visible Light Photon Counter (VLPC) Absolute Quantum Efficiency and Saturation", DØ Note, #3889, 2001.

[28] Design Report of the Central Preshower Detector for the DØ Upgrade, DØ Note, #3014.

[29] Technical Design Report of the Forward Preshower Detector for the DØ Upgrade, DØ Note, #3445.

[30] R.C. Fernow, introduction to Experimental Particle Physics, Cambridge University Press(1986) 259

[31] C. Fabjan, Calorimetry in High Energy Physics in T. Ferbel, editor, Experimental Techniques in High Energy Physics

[32] R. D. Schamberger, The DØ Calorimeter Performance and Calibration, in: Proc. fifth Calorimetry in High Energy Physics(ed.. H.Gordon and D. Rueger, Upton, NY, September (1994), 39-50, (World Scientific, 1995).

[33] Design, performance and Upgrade of the DØ Calorimeter, DØ Note 2417.

[34] Ebbe M . Nyman, Phys. Rep. V**9**, Issue 3, p179-198.

[35] P. Amaral et al., Nucl. Inst. Meth. A **443** (2000) 51-70.

[36] DØ Collaboration, Muon System Upgrade Home Page, see $http://www-d0.fnal.gov/hardware/upgrade/muon\_upgrade/muon\_upgrade.html$

[37] DØ Collaboration, S. Abachi et al, Nucl. Inst. Meth. A **338**(1994) 185.

[38] C. Brown et al., Nucl. Inst. Meth. A **279** (1989)331.

[39] J.M. Butler et al., Nucl. Inst. Meth. A **290** (1990)122.

[40] DØ Collaboration, John M. Butler, "Local Muon Momentum Resolution", DØ Note **4002**, 2002.

[41] V. Abramov et al, "Forward muon system for the DØ Upgrade", Nucl. Inst. Meth. A **419**, 660(1998).

[42] G.C. Blazey, "The DØ Run II Trigger", $http://niuhep.physics.niu.edu/\ blazey/rt.ps$

[43] DØ Collaboration web page for L1, $http://www.pa.msu.edu/hep/d0/l1/$

[44] DØ Collaboration, DØ Note #328. DØ Note #705.

[45] DØ Collaboration web page for L2, $http://www.pa.msu.edu/hep/d0/l2/$

[46] DØ Collaboration web page for L3, $http://www-d0.fnal.gov/computing/algorithms/level3/home.html$

[47] DØ Collaboration, DØ Note #4303.

[48] DØ Silicon Tracker Technical Disign Report. Also DØ Note #2075, #2169.

[49] $http://www.nevis.columbia.edu/\ christos/Research\_dir/D0\_BPhysics\_files/slt\_v50.txt$

[50] $http://www.nevis.columbia.edu/\ christos/Research\_dir/D0\_BPhysics\_files/sst\_v50.txt$

[51] R. Akers et al. Phys. Lett. B **327**, 411(1994)

[52] P. Abreu et al. Zeit. Phys. C **72**, 17(1996)

[53] CDF Collaboration, Phys. Rev. **D61**, 072005

[54] S. Ellis and D. Soper, Phys. Rev. D **48**, 3160(1993)

[55] Yu.L. DoKshitzer, Better Jet Clustering Algorithms, hep-ph/9707323 v2 23 Aug 1997

[56] See, for example, DØ Collaboration, S. Abachi, et al, . Phys. Letters B357 500 (1995); CDF Collaboration, F. Abe, et al, Phys. Rev. Lett. **68**, 1109 (1992).

[57] See, for example, ZEUS Collaboration, Phys. Lett. B **306**, 158 (1993); Z. Phys. C **59**, 231 (1993).

[58] See, for example, "QCD Studies at LEP", T. Hebbeker, Proceedings of the Joint International Lepton-Photon Symposium and Europhysics Conference On High Energy Physics, Vol. 2, 73, edited by S. Hegarty et al., Geneva, 1991.

[59] B. Abbott et al. Report No. Fermilab-Pub-97/242-E, 1997.

[60] DØ Collaboration, DØ Note #3777. DØ Note #3468. DØ Note **3585**

[61] R.D. Field, Phys. Rev. **D65**, 094006

[62] Physical Review D, Particles and Fields, July 2002, Part1. 010001-227.

[63] Statistics - A Guide to the use of statistical methods in the physical science. Roger Barlow. John Wiley & Sons, Inc.

[64] "Measurement of $\sin(2\beta)$ from $B \to J/\psi K^0_s$ with the CDF detector", Physical Review D, volume 61, 072005.

[65] "Sensitivity of Time-Dependent CP-Asymmetry Measurement Versus Time-Integrated One in B System", SCAN-9907037, CERN Libraries, Geneva.

[66] Heavy Flavor Averaging Group, *http* : *//www.slac.stanford.edu/xorg/hfag/triangle/winter*2004/*index.shtml*